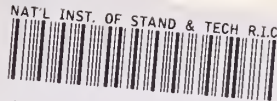


A11100 986400

NBS
PUBLICATIONS



A11104 939625

NBSIR 79-1767

NBS: Properties of Electronic Materials

J. R. Manning

National Bureau of Standards
Washington, D.C. 20234
Phone: (301) 921-3354

June 1979

Annual Report
For the Period 2 April 1978 - 1 April 1979
NASA Government Order H-27954B



S. DEPARTMENT OF COMMERCE

NATIONAL BUREAU OF STANDARDS

QC
100
U56
79-1767
C.2

NOV 13 1979

NBSIR 79-1767

**NBS: PROPERTIES OF ELECTRONIC
MATERIALS**

J. R. Manning

National Bureau of Standards
Washington, D.C. 20234
Phone: (301) 921-3354

June 1979

Annual Report
For the Period 2 April 1978 - 1 April 1979
NASA Government Order H-27954B

U.S. DEPARTMENT OF COMMERCE, Juanita M. Kreps, *Secretary*
Jordan J. Baruch, *Assistant Secretary for Science and Technology*
NATIONAL BUREAU OF STANDARDS, Ernest Ambler, *Director*

TABLE OF CONTENTS

	<u>Page</u>
Summary	1-2
Task 1 - SURFACE TENSIONS AND THEIR VARIATIONS WITH TEMPERATURE AND IMPURITIES by S. C. Hardy and S. R. Coriell.	3-24
Task 2 - SOLUTAL CONVECTION DURING DIRECTIONAL SOLIDIFICATION by W. J. Boettinger, S. R. Coriell, F. S. Biancaniello, and M. R. Cordes	25-81
Task 3 - A THERMOCHEMICAL STUDY OF CORROSIVE REACTIONS IN OXIDE MATERIALS by H. S. Parker, R. S. Roth, C. D. Olson, and E. R. Plante	82-102
Task 4 - THERMODYNAMIC PROPERTIES OF REFRACTORY INORGANIC MATERIALS AT HIGH TEMPERATURES by J. H. Colwell.	103-131
Distribution List	132-133

National Bureau of Standards
Properties of Electronic Materials

Summary

This report describes NBS work for NASA in support of NASA's Materials Processing in Space Program covering the period April 2, 1978 to April 1, 1979. The NBS program has two main thrusts:

1) Carrying out precision measurements in space and investigating the feasibility of improved measurements when the space environment offers a unique opportunity for performing such measurements. These measurements would be useful for either space processing or processes on the ground.

2) Obtaining precision measurements on material properties when these properties are important to the design and interpretation of space processing experiments. These measurements would be carried out either in space or on the ground.

The NBS work is carried out in four tasks. These tasks have, as two of their focal points, the role of convection effects and the role of container effects, both of which would differ in space-based experiments from those found in ground-based experiments. The results obtained for each task are given in detailed summaries in the body of the report. Briefly, in Task I - Surface Tensions and their Variations with Temperature and Impurities - measurements of the surface tension, γ , of liquid gallium were made in vacuum by the sessile drop technique as a function of temperature T . In the range 150 °C to 750 °C, it

was determined that $d\gamma/dT = -0.068 \text{ mJ/m}^2 \text{ }^\circ\text{C}$. In Task 2 - Solutal Convection during Directional Solidification - samples of off-eutectic Pb-rich Pb-Sn were directionally solidified and macrosegregation along the length of the sample attributed to solutal convection was measured. The segregation is often sufficient to prevent plane front solidification, thus causing dendritic instead of composite microstructures. In Task 3 - A Thermochemical Study of Corrosion Reactions in Oxide Materials - phase relationships in the $\text{K}_2\text{O-Fe}_2\text{O}_3$ system were investigated for the 80 to 100 percent Fe_2O_3 portion of the system up to 1600 $^\circ\text{C}$ with major corrosion of the platinum containers being avoided, perhaps because of the small amount of Fe^{+2} in the specimens. In Task 4 - Thermodynamic Properties of Refractory Materials at High Temperatures - methods of determining heat capacities in reactive liquid samples levitated at high temperatures, especially by use of freely-cooling spherical samples, were analyzed.

Task 1

Surface Tensions and Their Variations with Temperature and Impurities

S. C. Hardy and S. R. Coriell

Metal Science and Standards Division
Center for Materials Science

Summary

Instrumentation and techniques have been developed to measure the surface tension of liquid metals using the sessile drop method under high vacuum conditions. The drop profiles are analyzed with the classic Bashforth and Adams method and by fitting the entire profile to solutions of the Young-Laplace equation using a computer routine. The results of the two analyses are in agreement. The surface tension of gallium was measured from 30 °C to 750 °C in a vacuum of at least 10^{-8} torr. The surface tension values show some adsorption related curvature below 150 °C; above this temperature, the surface tension decreases linearly with a slope of $-0.068 \text{ mJ/m}^2 \text{ } ^\circ\text{C}$. These results are not in quantitative agreement with any previous measurements.

Introduction

It has been recognized for many years that surface tension gradients produced by temperature or chemical concentration variations on free liquid surfaces can generate significant fluid flows. In the low gravity levels of space vehicles, flows of this kind will be the dominant ones. A quantitative understanding of the resulting complex phenomena often requires that the dependence of the surface tension on chemical concentration and temperature be known with some accuracy. These thermodynamic properties, however, are not known well enough for many metals and semiconductors of scientific and commercial interest to permit meaningful analysis of observed effects or adequate design of future experiments. Thus accurate measurements of the temperature and chemical concentration dependence of the surface tension of materials are necessary before a basic understanding of the fluid flow behavior is possible. It is the objective of this program to make such surface tension measurements.

Gallium was selected for initial study because it is a convenient model fluid for thermocapillary flow experiments and because there is considerable uncertainty about its surface tension and, more critically, the temperature variation of its surface tension. Previous measurements are not in agreement, probably due to the sensitivity of the liquid gallium surface to contamination by impurities.

The evidence for the role of impurities in surface tension measurements is of two types. The first effect is the observation of

a nonlinear temperature dependence of the surface tension. Typically what is found is that the tension decreases with increasing temperature as expected, but the values at low temperatures lie below the linear extrapolation of the high temperature data. This is interpreted as evidence of enhanced adsorption and consequent surface tension depression at lower temperatures. Several previous measurements have found such a nonlinear temperature dependence for the gallium surface tension^[1,2]. It must be noted, however, that there does not seem to be any compelling theoretical reason to expect the surface tension to decrease linearly with increasing temperature. Recent careful measurements with zinc have found a different dependence^[3].

The second type of effect which suggests the presence of impurities is the observation of a time dependent surface tension. A freshly formed surface will be reasonably clean. As the concentration of impurities on the surface builds up to equilibrium, the surface tension drops to a constant value. Early measurements of the gallium surface tension depended on forming a new pendant drop and recording its shape quickly before significant adsorption could occur^[4]. The value found for the surface tension at the melting point was $735 \pm 20 \text{ mJ/m}^2$; most subsequent measurements have been slightly lower than this range.

Some recent measurements of the gallium surface tension obtained using the pendant drop technique and displaying a typical decrease with time is important because the observed initial values over 800 mJ/m^2

are much higher than any previously reported^[5]. This suggests that all existing surface tension values for gallium were affected by impurities. We performed similar experiments last year^[6] with somewhat different results: although we did not observe high initial values, occasionally the surface tension would gradually rise from about 700 mJ/m^2 to around 800 mJ/m^2 . The effect was not reproducible, which suggested an uncontrolled impurity, probably in the inert atmosphere in which the measurements were made. We therefore thought it desirable to make future measurements in a vacuum system. This is feasible because gallium has a very low vapor pressure. By using the sessile drop technique we could also conveniently study the surface tension over a wide temperature range, a primary goal of this program.

Experimental Procedures

The sessile drop technique is considered to be the most accurate method for measuring surface tensions^[7]. It is based on a comparison of the observed profile of a drop sitting on a horizontal plane with the profile calculated by solving the Young-Laplace equation. No approximations are necessary in this comparison, although several treatments which simplify the surface tension calculation have been developed. We are using an experimental modification of the sessile drop technique in which the drop sits in a cup rather than on a plane^[8]. The cup stabilizes the drop and imposes a circular cross section on the drop base, thus eliminating errors arising from the anisotropic wetting which sometimes is encountered when the drop rests on a flat surface.

Figure 1 is a schematic diagram of the experimental apparatus as seen from the top. The drop cup is contained in a vycor tube which connects to a vacuum system consisting of a 30 liter/sec. ion pump, two crosses, a nude ionization gauge, a bakeable isolation valve, and a mechanical pump and cold trap which are not shown. The cup rests loosely in a flat bottomed depression machined in a steel block. The depression keeps the cup near the center of the tube and also catches any gallium which might spill during the loading procedure or the experiments. The block rests in a semi-circular section cut from a stainless steel tube which fits loosely inside the vycor tube. The steel tube and the block and cup which it contains can be rotated within the outer vycor tube by using a magnet. This permits changes and adjustments in the cup orientation. A chromel-alumel thermocouple is spot welded to the steel block and to the nickel leads of a pressed seal located near the flange in which the vycor tube is mounted. The vycor tube has an optical grade quartz window on the end through which the drop is photographed. A tube furnace or a heating tape is used to establish the drop temperature.

Before the gallium is placed in the cup, the system is evacuated and the block and cup assembly baked with a heating tape at about 500 °C for an hour. After cooling, the ion pump is turned off and the system filled with helium gas. The gallium is inserted in the cup using a long glass pipette connected to a micrometer syringe. This device is filled with absolute alcohol and about 10 cm³ of gallium are drawn into it. The flange containing the window is removed from

the vacuum system and quickly replaced with a tightly fitting stopper through which pass two vacuum couplings. Helium gas is flowed through a tube which extends into the vacuum system to the area of the cup through one of these couplings. The pipette containing the gallium is inserted through the second coupling and pushed down the vycor tube until it is located directly over the cup. After flushing the system with helium for about ten minutes, gallium is forced from the pipette into the cup by moving the plunger of the micrometer syringe. When the drop has been formed in the cup, the pipette is first withdrawn; the helium feed tube and stopper are then removed and the window flange replaced using a new copper gasket. The system is now slowly evacuated by gradually opening the valve to the cold trap and mechanical pump. This is a delicate part of the procedure because if the pressure is reduced too quickly, gas generated in the cup can expel some of the gallium and reduce the drop volume to an unusable size.

After evacuation with the mechanical pump, the valve is closed and the ion pump started. When it is clear that this is pumping properly, the valve is tightened with a torque wrench to establish a vacuum tight seal and the mechanical pump is turned off. When the system pressure is about 10^{-6} torr, the gallium drop and the cup assembly are baked at about 400 °C for about an hour. This cleans the gallium surface and raises the surface tension producing a drop with a high profile. The ion pump is able to reduce the pressure to the low 10^{-8} torr range overnight after this treatment. A subsequent

bake of the vacuum system at about 250 °C is necessary to get to the 10^{-9} torr level.

The sessile drop technique can be used to make highly accurate surface tension measurements. In order to do so, however, the dimensions of the sessile drop must be measured to an accuracy of a few parts in 10^4 . This is a nontrivial measurement requirement; all elements of the optical system must be carefully aligned and focussed. The primary consideration is the lens used to image the drop. The numerical aperture of this lens must be large in order to obtain sufficient resolution, which rules out the use of the standard type of small laboratory telescope. In our system we use a Wollensak f/5.6 enlarging lens with a 190 mm focal length. The image of the drop is focussed on the ground glass plate of a 4"x5" camera whose lens has been removed. The diaphragm of this camera is located at the second focal point of the enlarging lens and a small aperture is used to eliminate nonparaxial rays. The lens is mounted in a movable stage taken from a zone refiner. This stage can be precisely translated along the axis of the optical system by turning the screw drive manually. The image of the drop on the ground glass plate is observed with a low power telescope as the lens is moved forward and backward. In this way the drop can be precisely focussed in the film plane. The drop is illuminated by a high intensity projector located about 20 feet away, i.e., near infinity for this lens. The entire optical system is aligned using techniques which will not be described here.

The drop is photographed on a high contrast, fine grained film designed for graphic arts work. After development the negative is placed between glass plates and analyzed on a measuring microscope. The micrometers of this instrument have a least count of 10^{-4} inch with a traverse of one inch, which is greater than the largest dimension to be measured from the photograph. The image of the drop is kept to this size because the use of a gauge block with the microscope introduces errors which are intolerably large.

The negative must be oriented on the microscope stage so that the two orthogonal directions of stage translation are parallel to the horizontal and vertical axes of the drop. This orientation is a critical preliminary step in order to obtain consistent surface tension values at different points of the profile. This is accomplished by rotating the microscope stage until the sum of the coordinates of the drop diameter are the same at different distances from the drop apex^[9]. Thus at Z_1 , the left hand and right hand coordinates are X_1 and X_r . If the stage is now translated to a different Z_2 , the coordinates will be $X_1 - \Delta X$ and $X_r + \Delta X$ if the drop is symmetrical about the Z axis, i.e., if the microscope Z translation is along the direction of gravity in the drop photograph. Thus the sum is $X_1 + X_r$ for each set of coordinates. In practice these sums can be made to agree within a few parts in 10^4 with no difficulty.

The gallium used in these measurements was nominally of six nines purity and in ingot form. It was prepared for use by melting the entire 100 gram ingot under pure alcohol containing a few drops of

HCl to dissolve the surface oxide. After rinsing with pure alcohol several times, some gallium was drawn into the pipette. The remaining gallium was then resolidified by cooling and stored under alcohol.

Experimental Results

A preliminary test of the resolution and aberrations of the optics was made by photographing a precision ball bearing at the position of the drop. The negative was analyzed on the microscope at 100X by measuring the distance across the image of the bearing, $2X$, as a function of Z , the distance from the apex. The X dimension can also be calculated as a function of Z using r , the known radius of the bearing, i.e., $X_{\text{calc.}} = \sqrt{Z(2r-Z)}$. The quantity $X - X_{\text{calc.}}$ had a average value of .00005 inch for eight measurements over the profile of the bearing with no systematic variations detectable. We therefore concluded that the optical resolution was adequate and the lens was free of distortions at this level of measurement.

Figure 2 shows a typical drop profile. The cup diameter is known and is used to provide an absolute dimensional calibration. In Figure 3 the edge of the drop profile on the negative is shown at 100X magnification; this is what is seen during measurement. The profile is not absolutely sharp at this magnification. The intensity changes over a significant distance, i.e., there is a penumbra. This picture also shows a dark band and an adjacent light band which is much fainter and narrower. These are similar to Fresnel fringes and arise from the diffraction of light by the drop. Their observation means that a basic physical limitation on the measurements has been reached.

The images of the sessile drops were measured as described previously and the surface tension calculated at a number of locations on the surface using the Bashforth and Adams technique and tables^[10]. We also developed a computer program to calculate a best value of the surface tension from measurements of the coordinates of many points on the drop profile. This program repeatedly solves the Young-Laplace equation for the drop shape while adjusting the surface tension^[11] and several other parameters using a simplex method of function minimization^[12] to provide a best fit to the measured coordinates. In Table 1 we list the dimensions measured, the surface tensions calculated by the Bashforth and Adams technique, the dimensions computed by the program which give a best fit to the entire profile, and the value of the surface tension the minimization procedure selected to give this best fit. The average of the surface tension values calculated by the Bashforth and Adams technique differs from this by only 0.6 mJ/m^2 , i.e., $\sim 0.1\%$. In the data we present subsequently surface tensions given are all calculated using the Bashforth and Adams tables. The computer program will be used only to process data which we consider to be in final form.

The surface tension of gallium was measured from the melting point to about 750°C at several vacuum levels. Figure 4 shows some early data taken using a pyrex cup whose circularity and stability were inferior to the quartz cups used later. The vacuum levels were not measured for these experiments because the ionization gauge had not yet been received. From subsequent work we estimate the pressure

to have been in the 10^{-5} torr range. The data clearly shows curvature below about 250 °C. This is probably due to adsorption from the residual atmosphere with surface tension depression as discussed in the introduction.

Measurements of the gallium surface tension obtained using a quartz cup are shown in Figure 5. The vacuum in these experiments ranged from about 5×10^{-8} torr at the high temperature end to about 1×10^{-9} torr from 300 °C to room temperature. This data also shows curvature, but only below about 150 °C. The measurements were made by raising the temperature to at least 400 °C to clean the surface and then cooling to the desired temperature. Because the sample is in vacuum and does not make good thermal contact with the vycor tube, it is not possible to change the temperature of the drop quickly; with the heating source removed, three hours are required to cool the drop to 30 °C from 150 °C. Thus the gallium drop has time to approach adsorption-desorption equilibrium with the residual atmosphere in the vacuum system. The depression of the surface tension at low temperature is almost certainly due to adsorption. A regression analysis of the linear data gives $d\gamma/dT = - 0.068 \text{ mJ/m}^2 \text{ } ^\circ\text{C}$.

A few measurements have been made of the time dependence of the surface tension. In the linear region it appears to be constant; at lower temperatures there is some evidence for a slight decrease of the surface tension over several hours at 100 °C even at a pressure of 10^{-9} torr. Additional work in this area is needed.

Conclusions and Discussion

The data presented in Figure 5 are replotted in Figure 6 with the results of three previous measurements of the gallium surface tension. Our results clearly do not agree with these earlier measurements. The two nonlinear curves shown in the figure are in approximate agreement. The temperature dependences suggested by these authors^[1,2] are

$$\gamma_I = 708 - .0031(T-29.87) - .00067(T-29.87)^2$$

$$\gamma_{II} = 706.7 - .000647(T-29.87) - .0000965(T-29.87)^2.$$

with T in $^{\circ}\text{C}$ and γ in mJ/m^2 .

The linear curve^[13] is described by

$$\gamma_{III} = 718 - .101(T-29.87).$$

The temperature dependence of γ we find resembles the relationship of curve 3 if we ignore the points below 120°C which are clearly showing an adsorption effect. However, our value of $d\gamma/dT$ is significantly smaller in absolute value than the slope of curve 3. In contrast, the present data at high temperature ($> 400^{\circ}\text{C}$) is in fair agreement with the values of γ and $d\gamma/dT$ of curves 1 and 2.

The disparate experimental results shown in Figure 6 pose a dilemma. This results because γ and $d\gamma/dT$ give contradictory evidence about the role impurities are playing in the measurements. Surface active impurities will lower the surface tension as described by the Gibbs adsorption equation. Although it is not as clearly defined, adsorption should also make $d\gamma/dT$ less negative. This is the effect

shown in the data of Figure 4 and in the low temperature data of Figure 5. Thus, as the surface gets cleaner, γ should increase and $d\gamma/dT$ should assume a larger negative value.

By the first of the above criteria, the surfaces in our measurements are cleaner than those in the data of curves 1, 2, and 3 because our γ values are the highest over the entire temperature range. However, the $d\gamma/dT$ criteria would reach the opposite conclusion. The measurements represented by curve 3 would be identified as the cleanest at low temperature, and of curve 1 at high temperature. This is not likely. We conclude that arguments of this kind cannot resolve the contradictions in the various measurements.

The problems of interpretation of surface tension data found here are not unique; similar contradictions are encountered in comparisons of some recent measurements on zinc^[3] referred to earlier with previous results. It seems probable that the different γ and $d\gamma/dT$ values found by different workers is due to the presence of surface active impurities whose nature and concentration vary with temperature in an unknown and uncontrolled manner. The measurements shown in curves 1 and 3 of Figure 6, as an example, were made in evacuated cells which had been sealed off from the pumps at a pressure no better than 10^{-6} torr. Despite rigorous outgassing prior to seal off, such systems must have vastly different vacuum levels at low and high temperatures. The adsorbed chemical species on the liquid surface are probably coupled to some extent to these variations in cell atmosphere. Thus one might interpret a curvature such as that shown

in curves 1 and 2 of Figure 6 as surface tension depression at high temperature due to adsorption on the liquid gallium of species being desorbed from the cell walls.

There is no support in the measurements shown in Figure 6 for the anomalously high values ($\gamma \gtrsim 800 \text{ mJ/m}^2$) found by Abbaschian^[5] and seen occasionally in our work last year^[6]. It is interesting to note, however, that a linear extrapolation of the high temperature data of curve 1 in Figure 6 gives such a value at the melting point. In addition, the old work of Mack et al. contains one anomalously high value. Thus it is possible that all the measurements summarized in Figure 6 have been affected by an impurity. A better characterization of the surface and gaseous impurities is essential before these complex observations can be interpreted.

References

- [1] O. A. Timofeevicheva and P. P. Pugachevich, Dokl. Akad. Nauk SSR, 134, 840 (1960).
- [2] V. I. Nizhenko, L. P. Sklyarenko and B. N. Eremenko, Ukrain. Khim. Zhur. 6, 559 (1965).
- [3] W. L. Falke, A. E. Schwaneke and R. W. Nash, Met. Trans. 8B, 301 (1977).
- [4] G. L. Mack, J. K. Davis and F. E. Bartell, J. Phys. Chem. 45, 846 (1941).
- [5] G. J. Abbaschian, Journal of Less-Common Metals 4C, 329 (1975).
- [6] S. C. Hardy and S. R. Coriell, Properties of Electronic Materials, NBSIR 78-1483, 3 (1978).
- [7] D. W. G. White, Trans. ASM 55, 757 (1962).
- [8] J. V. Najdich and V. N. Eremenko, Fiz. Metal. i Metalloved 11, 883 (1961).
- [9] C. A. Smolders and E. M. Duyvis, Recueil 80, 635 (1961).
- [10] F. Bashforth and J. C. Adams, The Theories of Capillary Action, University Press, Cambridge, p. 1883.
- [11] C. Maze and G. Burnet, Surface Science 24, 335 (1971).
- [12] L. F. Shampine, SC-RR-72 0657, Sandia Laboratories, Albuquerque, New Mexico, Sept. 1972.
- [13] A. A. Karashaev, S. N. Zadumkin and A. I. Kukhno, Russ. J. of Phys. Chem. 41, 329 (1967).

Table 1. Comparison of a Sessile Drop as Analyzed by the Bashforth and Adams Technique and the Computer Profile Fitting Routine

Z (measured) cm	Z (calculated) *	r (measured) cm	r (calculated) cm	γ B. & A. mJ/m ²
.08922	.08909	.35736	.35730	691.9
.13930	.13917	.42944	.42940	690.8
.16076	.16063	.45332	.45339	687.0
.19653	.19641	.48650	.48657	688.1
.23230	.23218	.51264	.51273	687.2
.26807	.26795	.53285	.53292	690.2
.30385	.30372	.54781	.54779	689.2
.33962	.33950	.55781	.55768	682.8
.39263	.39251	.56357	.56340	Max. r
.44694	.44681	.55753	.55755	687.1
.48271	.48258	.54598	.54607	686.7
Average γ				688.1
Best fit γ				688.7

* The difference between Z (measured) and Z (calculated) is constant; this constant is one of the parameters fitted in the computer code.

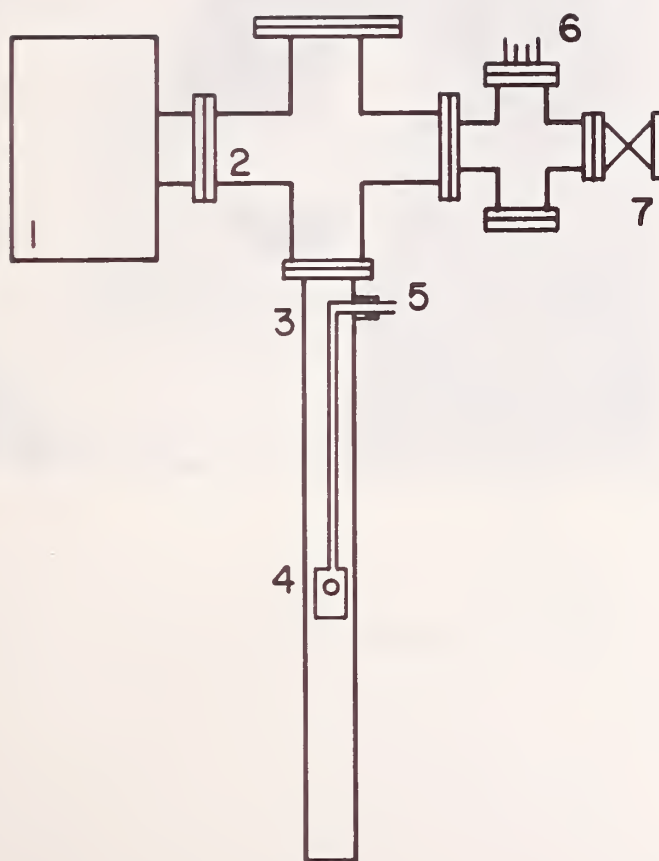


Fig. 1. Schematic diagram of sessile drop apparatus: (1) ion pump (2) cross (3) vycor tube (4) cup containing gallium (5) thermocouple leads (6) ionization gauge (7) isolation valve.



Fig. 2. Picture (negative) of sessile drop.



Fig. 3. Edge of drop as seen through microscope at 100X.

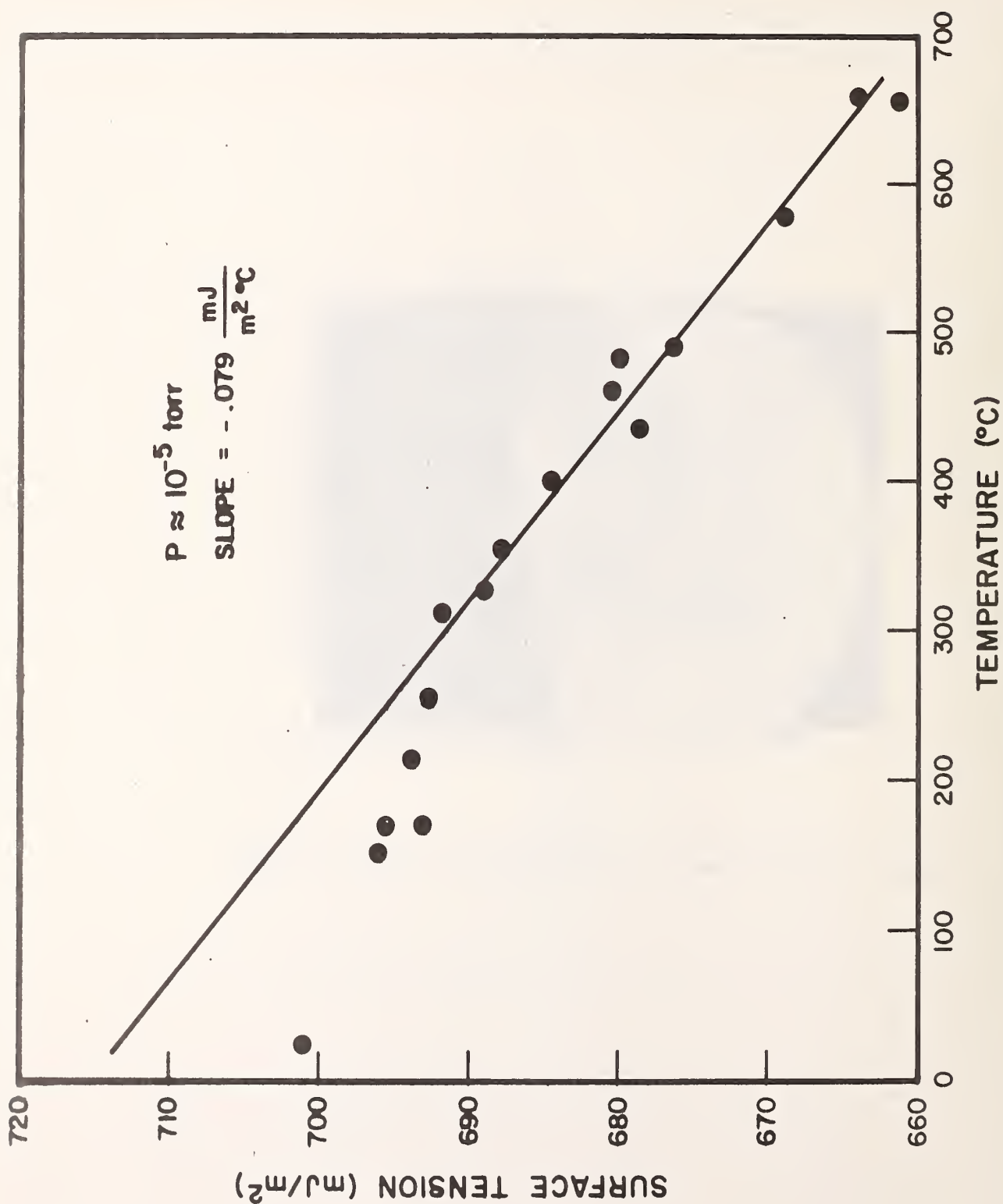


Fig. 4. The surface tension of gallium as a function of temperature (preliminary data at an intermediate vacuum level; glass cup).

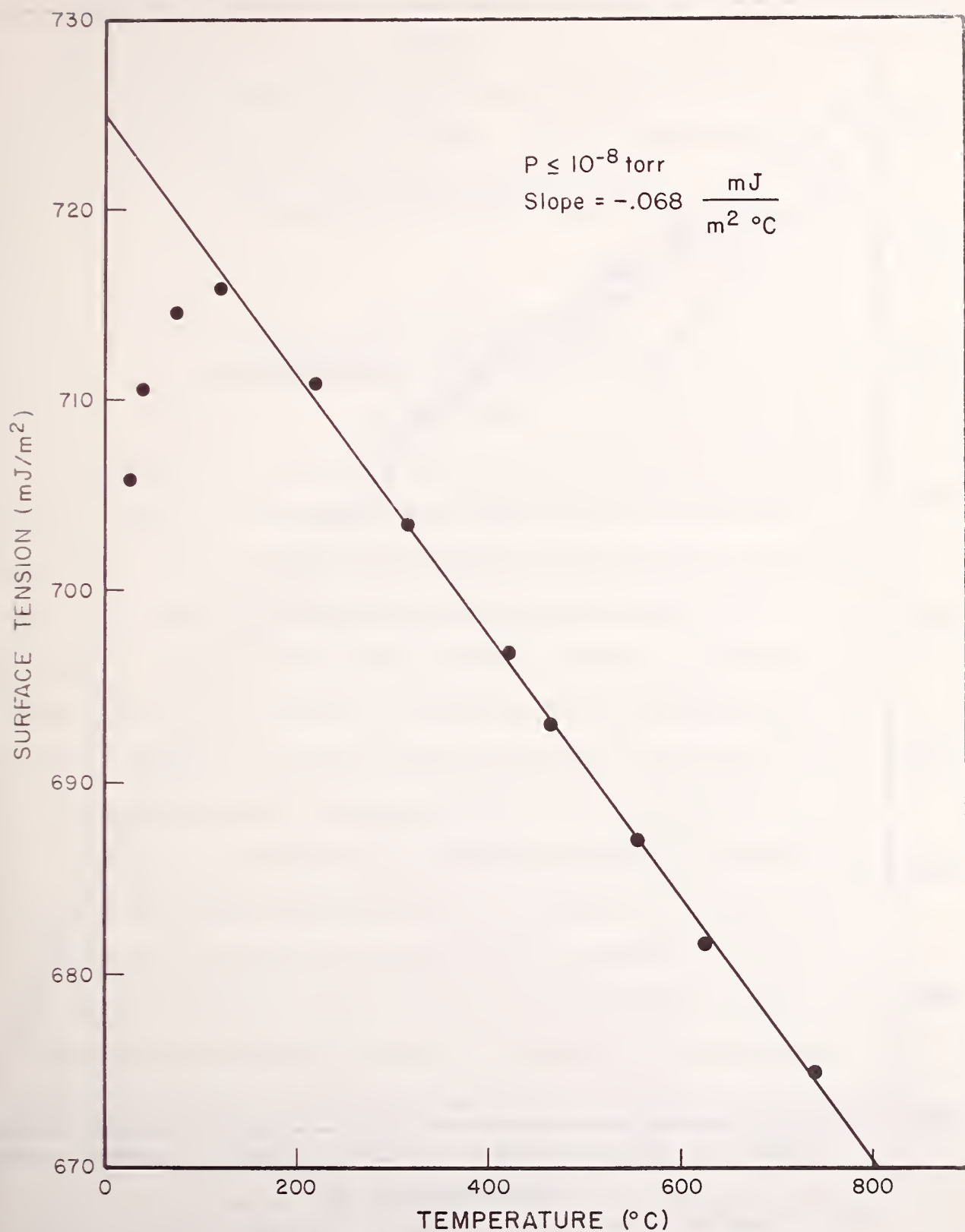


Fig. 5. The surface tension of gallium as a function of temperature (high vacuum level; quartz cup).

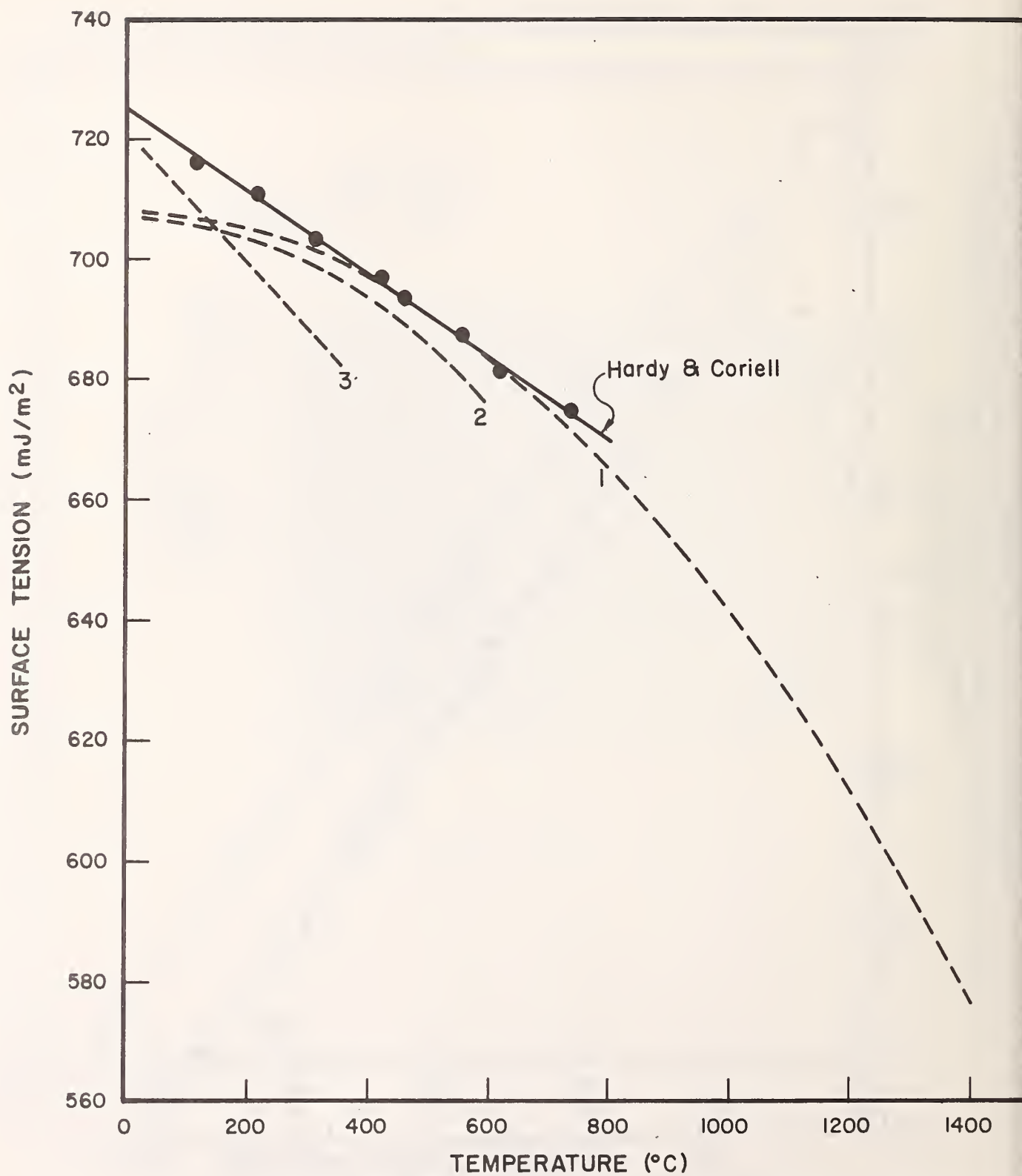


Fig. 6. Comparison of the various measurements of the surface tension of gallium.

Task 2

Solutal Convection during Directional Solidification

W. J. Boettinger, S. R. Coriell, and F. S. Biancaniello

Metal Science and Standards Division
Center for Materials Science

and

M. R. Cordes
Mathematical Analysis Division
Center for Applied Mathematics

Summary

This research is directed towards an understanding of solutal convection caused by the simultaneous concentration and temperature gradients present during the directional solidification of alloys and is a continuation of research previously reported under NASA Government Order H-27954B (NBSIR 78-1483). Included in this study is investigation of the effects of convection on the microstructure and chemical homogeneity of directionally solidified alloys and of the conditions under which undesirable effects can be eliminated.

The onset of convective and interfacial instabilities during the vertical directional solidification of a binary alloy is determined theoretically by means of a linear stability analysis. For values of the physical constants appropriate to the solidification of lead containing tin, the critical bulk solute concentration delineating the demarcation between stability and instability is numerically calculated as a function of growth velocity. For concentrations less than the critical concentration, the system is stable. For velocities in the

range 1-40 $\mu\text{m/s}$, a convective-like long wavelength instability occurs at a critical concentration which increases with velocity. For velocities $> 40 \mu\text{m/s}$, the concentration at which instability occurs decreases as velocity is increased and the values of concentration and wavelength at the onset of instability correspond to the predictions of previous morphological stability theory which neglected density changes and convection. Application of a vertical static magnetic field increases the critical concentration for convective instabilities but a field of a tesla is needed to cause an order of magnitude change. For a given velocity, the increase in critical concentration for the onset of convective instability due to a 10^{-4} reduction in gravitational acceleration is a strong function of velocity, ranging from a factor of 20 to 3000.

The occurrence of solutal convection and its effects on the microstructure and macrosegregation of directionally solidified alloys, particularly off-eutectics, also has been investigated. During plane front solidification the concentration of less dense solute is increased in the liquid near the solid-liquid interface and there is the possibility of solutal convection. In this year's research, the effect of solute gradient induced convection on the macrosegregation of Pb-rich Pb-Sn off-eutectic alloys during vertical solidification is determined experimentally as a function of composition and growth rate. In many cases macrosegregation is sufficiently great to prevent the plane front solidification of the alloy. The transition from

dendritic to composite structure is found to occur when the composition of the solid is close enough to the eutectic composition to satisfy a stability criterion based on G/V (temperature gradient/growth rate).

A. THEORY

Introduction

In recent years there have been extensive research and development efforts on the effect of fluid flow on solidification and on the properties of the resulting solids^[1-2]. In general, one attempts to control fluid flow in such a way as to obtain optimum materials properties. To minimize fluid flow, it is well known that horizontal temperature and concentration gradients must be avoided. If the fluid density gradient is parallel to the gravitational field, a motionless solution of the fluid flow equations is possible; in the remaining discussion we will assume that this is the case, i.e., there are no horizontal density gradients.

In the plane front constant velocity directional solidification of all alloys other than congruent melting compounds and invariant eutectics, there exists in the liquid an exponential concentration gradient which extends ahead of the liquid-solid interface with a decay distance of D/V where D is the liquid interdiffusion coefficient and V is the interface velocity. There also exists a temperature gradient which is essentially linear in the region in which the concentration gradient is exponential. The density, being a function of temperature and concentration, can have various profiles depending on the solidification conditions and the properties of the fluid.

In the theoretical section of this report, the onset of convective and interfacial instabilities during the directional solidification of a binary alloy at constant velocity vertically upwards (positive z -direction) is treated by a linear stability analysis. We assume that the

initial state of the system corresponds to a planar solid-liquid interface of infinite extent in the x and y directions and that there are no horizontal temperature or solute gradients. Further we assume that the liquid density ρ is a linear function of temperature T and solute concentration c. We consider a positive temperature gradient and a liquid which expands on heating, i.e., $(\partial\rho/\partial T)(\partial T/\partial z) < 0$ and the situation where $(\partial\rho/\partial c)(\partial c/\partial z) > 0$. Thus, the temperature gradient alone would cause a negative density gradient and the solute gradient alone would cause a positive density gradient, e.g., this is the case when a solute less dense than the solvent is rejected at the solid-liquid interface. In this model, in the absence of convection, the only fluid flow would be a uniform flow arising from the density difference between solid and liquid. Because the usual solidification boundary conditions are used at the solid-liquid interface, the hydrodynamic and interfacial stability processes are coupled. In the limit that the liquid density does not depend on temperature or solute concentration, and the density change on solidification is negligible, the present treatment reduces to a morphological stability analysis.

In the unperturbed state in a frame moving with the solid-liquid interface, the fluid velocity, temperature and density are functions of z alone; perturbations whose x, y, and time t dependence are of the form $\cos \omega_x x \cos \omega_y y \exp(\sigma t)$ are introduced, where ω_x and ω_y are spatial frequencies and σ determines the growth rate of the perturbation. The onset of convection corresponds to conditions for which the real part of σ vanishes for some value of $\omega(\omega^2 = \omega_x^2 + \omega_y^2)$ and is negative for all other values of ω .

Theoretical Formulation

The basic theory was described in our previous report^[3]. We have now incorporated into the theory the effect of a static magnetic field. For completeness and for the reader's convenience, the basic theory is repeated in this section.

We consider unidirectional vertical solidification of a binary alloy at constant velocity. We choose an (x', y', z') laboratory coordinate system such that the z' axis is perpendicular to the planar solid-liquid interface. The gravitational field is of the form $\bar{g} = (0, 0, -g)$, i.e., positive g implies a field anti-parallel to the z' axis. The following differential equations govern the fluid velocity $\bar{u} = (u_{x'}, u_{y'}, u_{z'})$, temperature T , magnetic field $\bar{H} = (H_{x'}, H_{y'}, H_{z'})^*$ and concentration c [4-6]

$$\nabla' \bar{u} = 0, \quad (1)$$

$$\nabla' \bar{H} = 0, \quad (2)$$

$$(\partial \bar{u} / \partial t') + (\bar{u} \nabla') \bar{u} = -(1/\rho_0) \nabla' (p + \bar{H}^2 / 8\pi) + \nu \nabla'^2 \bar{u} - \bar{g} [\alpha (T - \bar{T}) + \alpha_c (c - \bar{c})] + (\bar{H} \nabla') \bar{H} / 4\pi \rho_0, \quad (3)$$

$$(\partial \bar{H} / \partial t') + (\bar{u} \nabla') \bar{H} - (\bar{H} \nabla') \bar{u} = \eta \nabla'^2 \bar{H}, \quad (4)$$

$$(\partial T / \partial t') + \bar{u} \nabla' T = \kappa \nabla'^2 T, \quad (5)$$

$$(\partial c / \partial t') + \bar{u} \nabla' c = D \nabla'^2 c, \quad (6)$$

where t' is the time, p is a pressure, ν is the kinematic viscosity, κ

* Equations (2) and (4) correspond to four equations for the three components of the magnetic field; however, these four equations are not independent and actually correspond to three independent equations.

is the liquid thermal diffusivity, η is the liquid magnetic diffusivity, and D is the liquid diffusion coefficient. The prime on the operator ∇ indicates that it is with respect to the (x', y', z') coordinate system. We have assumed that the fluid density ρ is given by $\rho = \rho_0 [1 - \alpha(T - \hat{T}) - \alpha_c(c - \hat{c})]$, where ρ_0 is the density at $T = \hat{T}$ and $c = \hat{c}$. The above equations are based on the Oberbeck-Boussinesq approximation [4-5] and the coefficients ν , κ , η , and D are assumed constant.

We transform to a moving coordinate system (x, y, z) attached to the unperturbed planar solid-liquid interface which is moving with constant velocity $\bar{V} = (0, 0, V)$ in the z - direction, i.e., $x = x'$, $y = y'$, $z = z' - Vt$, and $t = t'$.

We obtain

$$\nabla \bar{u} = 0, \quad (7)$$

$$\nabla \bar{H} = 0, \quad (8)$$

$$(\partial \bar{u} / \partial t) - (\bar{V} \nabla) \bar{u} + (\bar{u} \nabla) \bar{u} = -(1/\rho_0) \nabla (p + \bar{H}^2 / 8\pi) + \nu \nabla^2 \bar{u} - \bar{g} [\alpha(T - \hat{T}) + \alpha_c(c - \hat{c})] + (\bar{H} \nabla) \bar{H} / 4\pi \rho_0, \quad (9)$$

$$(\partial \bar{H} / \partial t) - (\bar{V} \nabla) \bar{H} + (\bar{u} \nabla) \bar{H} - (\bar{H} \nabla) \bar{u} = \eta \nabla^2 \bar{H}, \quad (10)$$

$$(\partial T / \partial t) - \bar{V} \nabla T + \bar{u} \nabla T = \kappa \nabla^2 T, \quad (11)$$

$$(\partial c / \partial t) - \bar{V} \nabla c + \bar{u} \nabla c = D \nabla^2 c. \quad (12)$$

Note that \bar{u} is still measured in the laboratory coordinate system (x', y', z') .

The boundary conditions at the solid-liquid interface* are that the tangential components of the fluid velocity vanish (no slip condition) and that the normal component satisfy

$$\bar{\mathbf{v}} \cdot \bar{\mathbf{n}}(\rho_L - \rho_s) = (\bar{\mathbf{u}} \cdot \bar{\mathbf{n}})\rho_L, \quad (13)$$

where $\bar{\mathbf{v}}$ is the solidification velocity, $\bar{\mathbf{n}}$ is the unit normal to the solid-liquid interface, and ρ_L and ρ_s are liquid and solid densities, respectively, at the solid-liquid interface. The temperature and concentration satisfy

$$(\bar{\mathbf{v}} \cdot \bar{\mathbf{n}})L_v = (-k_L \nabla T + k_s \nabla T_s) \cdot \bar{\mathbf{n}}, \quad (14)$$

$$(\bar{\mathbf{v}} \cdot \bar{\mathbf{n}})(c_{sI} - c_I) = (\rho_L / \rho_s) D \nabla c \cdot \bar{\mathbf{n}}, \quad (15)$$

where L_v is the latent heat of fusion per unit volume of solid, k_L and k_s are thermal conductivities of liquid and solid, respectively, c_{sI} and c_I are solid and liquid concentrations at the solid-liquid interface, and all quantities are evaluated at the interface. The temperature T_s in the solid satisfies the differential equation

$$(\partial T_s / \partial t) - (\bar{\mathbf{v}} \cdot \bar{\mathbf{v}})T_s = \kappa_s \nabla^2 T_s, \quad (16)$$

where κ_s is the thermal diffusivity of the solid. Diffusion in the solid has been neglected. In addition, we have

$$T_{sI} = T_I, \quad (17)$$

$$c_{sI} = kc_I, \quad (18)$$

* The authors are indebted to R. F. Sekerka for detailed discussions and derivations of the boundary conditions at the solid-liquid interface.

$$(\bar{v} \cdot \bar{n}) = \mu \{T_e - T_I\}, \quad (19)$$

$$T_e = T_M + mc_I - T_M \Gamma K. \quad (20)$$

Here, we have used a subscript I to denote evaluation of the quantity at the solid-liquid interface; k is the partition coefficient, μ is a linear kinetic coefficient, T_e is the equilibrium temperature of a curved interface in the presence of solute, T_M is the melting point of the pure substance with a planar interface, m is the slope of the liquidus line, Γ is the capillary constant, i.e., the solid-liquid surface tension $\gamma = L_V \Gamma$, and K is the interface curvature. Boundary conditions for the magnetic field will be discussed subsequently.

We now solve the equations for a planar solid-liquid interface located at $z = 0$; all quantities are functions of z alone. We assume that in the moving frame there is no dependence on time. The fluid velocity, magnetic field, temperature, and concentration fields are

$$\bar{u}_0 = (0, 0, -\epsilon V), \quad (21)$$

$$\bar{H}_0 = (H_{0x}, H_{0y}, H_{0z}), \quad (22)$$

$$T_0 = d_1 - (\kappa G_L / V^*) \exp(-V^* z / \kappa), \quad (23)$$

$$T_{s0} = d_2 - (\kappa_s G_s / V \exp(-V z / \kappa_s)), \quad (24)$$

$$c_0 = c_\infty - (c_\infty / k)(k-1) \exp(-V^* z / D), \quad (25)$$

where $\epsilon = (\rho_s / \rho_L) - 1$, H_{0x} , H_{0y} , H_{0z} , d_1 and d_2 are constants, $V^* = V(\rho_s / \rho_L)$, G_L and G_s are temperature gradients in the liquid and solid, respectively, at the solid-liquid interface, c_∞ is the solute concentration far from the interface, and the subscript 0 indicates that the

solutions are for an unperturbed planar interface. From the boundary conditions we also have the relationships

$$VL_v = k_s G_s - k_L G_L, \quad (26)$$

$$V^*(c_\infty/k)(k-1) = DG_c, \quad (27)$$

$$d_1 - (\kappa G_L/V^*) = d_2 - (\kappa_s G_s/V), \quad (28)$$

$$c_{sI} = c_\infty, \quad (29)$$

$$V = \mu \{ T_M + (mc_\infty/k) - d_1 + (\kappa G_L/V^*) \}, \quad (30)$$

where G_c is the concentration gradient in the liquid at the solid-liquid interface. These relationships may be used to find explicit expressions for the constants d_1 and d_2 .

We now consider whether the above solutions, for which there is only a trivial fluid flow corresponding to the density change on solidification, are stable with respect to small fluctuations. We write

$$\bar{u} = \bar{u}_0 + \bar{W}(x, y, z, t), \quad (31)$$

$$\bar{H} = \bar{H}_0 + \bar{H}(x, y, z, t), \quad (32)$$

$$T = T_0 + T(x, y, z, t), \quad (33)$$

$$T_s = T_{s0} + T_s(x, y, z, t), \quad (34)$$

$$c = c_0 + C(x, y, z, t), \quad (35)$$

$$p = p_0 + p_1(x, y, z, t), \quad (36)$$

$$z = z_{sL}(x, y, t), \quad (37)$$

and will retain only linear terms in the perturbation quantities, \bar{W} , \bar{H} , T , T_s , C , p_1 , and z_{SL} . The function $z_{SL}(x, y, t)$ represents the shape of the solid-liquid interface which in general is not planar and the function $p_0(z)$ satisfies the unperturbed equations. We obtain the following differential equations for the fluctuations

$$\nabla \bar{W} = 0, \quad (38)$$

$$\nabla \bar{H} = 0, \quad (39)$$

$$\begin{aligned} (\partial \bar{W} / \partial t) - V^*(\partial \bar{W} / \partial z) = & - (\nabla p_h / \rho_0) + v \nabla^2 \bar{W} - \bar{g}(\alpha T + \alpha_c C) + \\ & (\bar{H}_0 \nabla)(H / 4\pi \rho_0), \end{aligned} \quad (40)$$

$$\partial \bar{H} / \partial t - V^*(\partial \bar{H} / \partial z) - (H_0 \nabla) \bar{W} = \eta \nabla^2 \bar{H}, \quad (41)$$

$$(\partial T / \partial t) - V^*(\partial T / \partial z) + W_z (\partial T_0 / \partial z) = \kappa \nabla^2 T, \quad (42)$$

$$(\partial C / \partial t) - V^*(\partial C / \partial z) + W_z (\partial C_0 / \partial z) = D \nabla^2 C, \quad (43)$$

$$(\partial T_s / \partial t) - V(\partial T / \partial z) = \kappa_s \nabla^2 T_s, \quad (44)$$

where $p_h = p_1 + \bar{H}_0 \cdot H / 4\pi$.

Using the identities for a function ϕ and a vector \bar{a}

$$\text{curl grad } \phi = 0 \quad (45)$$

and

$$\text{curl curl } \bar{a} = \nabla(\nabla \bar{a}) - \nabla^2 \bar{a}. \quad (46)$$

the z -component of equation (40) can be written

$$\begin{aligned} (\partial \nabla_z^2 \bar{W} / \partial t) - V^*(\partial \nabla_z^2 \bar{W} / \partial z) = & v \nabla_z^4 \bar{W} + g(\alpha \nabla_1^2 T + \alpha_c \nabla_1^2 C) + \\ & (H_0 \nabla)(\nabla_z^2 H / 4\pi \rho_0), \end{aligned} \quad (47)$$

where $\nabla_1^2 \equiv (\partial^2/\partial x^2) + (\partial^2/\partial y^2)$.

The boundary conditions on the perturbed quantities at $z = 0$ follow from the general boundary conditions and are

$$W_z = -\epsilon(\partial z_{sL}/\partial t), \quad (48)$$

$$W_x = \epsilon V(\partial z_{sL}/\partial x), \quad (49)$$

$$W_y = \epsilon V(\partial z_{sL}/\partial y), \quad (50)$$

$$(\partial z_{sL}/\partial t)L_v = -k_L[-(V^*/\kappa)G_L z_{sL} + \partial T/\partial z] + k_s[-(V/\kappa_s)G_s z_{sL} + \partial T_s/\partial z], \quad (51)$$

$$(\partial z_{sL}/\partial t)(1-k)(c_\infty/k) = kVG_c z_{sL} - (1-k)VC - (\rho_L/\rho_s)D(\partial C/\partial z), \quad (52)$$

$$G_s z_{sL} + T_s = G_L z_{sL} + T, \quad (53)$$

$$(\partial z_{sL}/\partial t) = \mu\{mG_c z_{sL} + mC + T_M \Gamma \nabla_1^2 z_{sL} - G_L z_{sL} - T\}. \quad (54)$$

From the continuity equation, eqs. (49) and (50) can be combined to give

$$(\partial W_z/\partial z) = -\epsilon V \nabla_1^2 z_{sL} \quad (55)$$

at $z = 0$.

The equations and the boundary conditions are homogeneous and linear. It is convenient to represent the time dependence and the x and y dependence in the form $\exp(\sigma t + i\omega_x x + i\omega_y y)$. The quantities ω_x and ω_y represent spatial frequencies and the general solution of the equations will involve integration over all values of ω_x and ω_y . In general σ is complex, i.e., $\sigma = \sigma_r + i\sigma_i$. If σ_r is positive for any values of (ω_x, ω_y) , then the solutions grow exponentially in time and

are unstable. If σ_r is negative for all values of (ω_x, ω_y) , the system is stable. The criterion for the onset of instability is determined by finding the conditions for which σ_r is not positive for any (ω_x, ω_y) and is equal to zero for some value of (ω_x, ω_y) . We write

$$W_z = \hat{W}_z(z) \exp(\sigma t + i\omega_x x + i\omega_y y), \quad (56)$$

$$H_z = \hat{H}_z(z) \exp(\sigma t + i\omega_x x + i\omega_y y), \quad (57)$$

$$T = \hat{T}(z) \exp(\sigma t + i\omega_x x + i\omega_y y), \quad (58)$$

$$C = \hat{C}(z) \exp(\sigma t + i\omega_x x + i\omega_y y), \quad (59)$$

$$T_s = \hat{T}_s(z) \exp(\sigma t + i\omega_x x + i\omega_y y), \quad (60)$$

$$z_{sL} = \hat{z} \exp(\sigma t + i\omega_x x + i\omega_y y), \quad (61)$$

where \hat{W}_z , \hat{H}_z , \hat{T} , \hat{C} , \hat{T}_s are functions of z alone, and \hat{z} is a constant.

Substituting these expressions in the differential equations yields

$$L\{\nu L + V^*(\partial/\partial z) - \sigma\}\hat{W}_z = g\omega^2(\alpha\hat{T} + \alpha_c\hat{C}) - L\{i(\omega_x H_{0x} + \omega_y H_{0y}) + H_{0z}(\partial/\partial z)\}\{\hat{H}_z/4\pi\rho_0\}, \quad (62)$$

$$\{\eta L + V^*(\partial/\partial z) - \sigma\}\hat{H}_z = - (H_0 \nabla)\hat{W}_z, \quad (63)$$

$$\{\kappa L + V^*(\partial/\partial z) - \sigma\}\hat{T} = \hat{W}_z G_L \exp(-V^*z/\kappa), \quad (64)$$

$$\{DL + V^*(\partial/\partial z) - \sigma\}\hat{C} = \hat{W}_z G_C \exp(-V^*z/D), \quad (65)$$

$$\{\kappa_s L + V(\partial/\partial z) - \sigma\}\hat{T}_s = 0, \quad (66)$$

where $L = [(\partial^2/\partial z^2) - \omega^2]$ and $\omega^2 = \omega_x^2 + \omega_y^2$. Equations (62-65) form a set of coupled ordinary differential equations for the perturbed

functions \hat{W}_z , \hat{H}_z , \hat{T} , and \hat{C} in the liquid.

When $\bar{H}_0 = 0$, the above equations reduce to those given in our previous report^[3]. We are primarily interested in the suppression of the onset of convection by a static magnetic field. It is clear that the horizontal components of H_0 will not suppress the onset of convection since there will always exist perturbations [characterized by values of (ω_x, ω_y)] for which the term $\omega_x H_{0x} + \omega_y H_{0y} = 0$, viz. for fixed H_{0x} , H_{0y} , and ω , choose $\omega_x = -\omega H_{0y} / (H_{0x}^2 + H_{0y}^2)^{1/2}$ and $\omega_y = \omega H_{0x} / (H_{0x}^2 + H_{0y}^2)^{1/2}$. When $\omega_x H_{0x} + \omega_y H_{0y} = 0$, equation (62) for \hat{W}_z is independent of H_{0x} and H_{0y} *. In the remainder of this report we will take $H_{0x} = H_{0y} = 0$ since finite values would not suppress the onset of convection. We will make two further assumptions concerning the magnetic field equation which greatly simplify the calculations. For good conductors $\eta \sim 10^4 \text{ cm}^2/\text{s}$ and it should be an excellent approximation to neglect the $V^*(\partial \hat{H}_z / \partial z)$ term in equation (63). At the onset of convection the real part of σ vanishes; if one further assumes that the imaginary part of σ vanishes, equation (62) can be written as

$$\{L\}\{v[L] + V^*(\partial/\partial z)\}\hat{W}_z = g\omega^2(\alpha\hat{T} + \alpha_c\hat{C}) + (H_{0z}^2/4\pi\rho_0\eta)(\partial^2\hat{W}_z/\partial z^2), \quad (67)$$

which is independent of the perturbed magnetic field. Thus, with these approximations it is not necessary to specify boundary conditions on the perturbed magnetic field or to calculate the perturbed magnetic field^[5-6]. Based on these assumptions, the effect of a magnetic field on the onset of convection will be discussed in the Numerical Results section.

*In general, a constant magnetic field in the x_1 direction does not affect a flow with fluid velocities which are independent of the x_1 coordinate.

Since the equation for \hat{T}_s does not depend on W_z , \hat{T} , or \hat{C} , it can be solved analytically. Using the boundary condition $\hat{T}_s(z \rightarrow -\infty) = 0$, we find

$$\hat{T}_s = d_3 \exp(\lambda z), \quad (68)$$

where d_3 is a constant and

$$\lambda = (-V/2\kappa_s) + \{(V/2\kappa_s)^2 + \omega^2 + (\sigma/\kappa_s)\}^{1/2}. \quad (69)$$

We have three coupled differential equations for the functions \hat{W}_z , \hat{T} , and \hat{C} . The boundary conditions, eqs. (48, 51-55), for \hat{W}_z , \hat{T} , and \hat{C} at $z = 0$ also contain the unknown constant \hat{z} and d_3 . However, we can eliminate these constants, and obtain boundary conditions for \hat{W}_z , \hat{T} , and \hat{C} at $z = 0$, viz,

$$\hat{W}_z + (\sigma/V\omega^2)(\partial\hat{W}_z/\partial z) = 0, \quad (70)$$

$$(\partial\hat{W}_z/\partial z) + (\epsilon V\omega^2 k_L/a_3)(\partial\hat{T}/\partial z) - (\epsilon V\omega^2 k_s \lambda/a_3)\hat{T} = 0, \quad (71)$$

$$(a_3 + a_2 k_s \lambda)\hat{T} - (a_2 k_L)(\partial\hat{T}/\partial z) - a_3 m\hat{C} = 0, \quad (72)$$

$$a_4 k_s \lambda \hat{T} - k_L a_4 (\partial\hat{T}/\partial z) + (1-k)V a_3 \hat{C} + (\rho_L/\rho_s)Da_3(\partial\hat{C}/\partial z) = 0, \quad (73)$$

where

$$a_1 = (k_L G_L V^*/\kappa) - (k_s G_s V/\kappa_s), \quad (74)$$

$$a_2 = (\sigma/\mu) - mG_c + G_L + T_M \Gamma \omega^2, \quad (75)$$

$$a_3 = \sigma L_V - a_1 - k_s \lambda (G_L - G_s), \quad (76)$$

$$a_4 = \sigma(1-k)(c_\infty/k) - kVG_c. \quad (77)$$

Thus we have four linear homogeneous boundary conditions at $z = 0$. We need four additional conditions in the liquid away from the interface since our differential equations are equivalent to a single eighth order equation. We consider a rigid planar isothermal boundary at $z = z_L$ (a constant). The boundary conditions are

$$\hat{W}_z = (\partial \hat{W}_z / \partial z) = \hat{T} = (\partial \hat{C} / \partial z) = 0. \quad (78)$$

However, in order to be able to treat a more general class of problems, we will write the boundary conditions as

$$W_z = 0, \quad (79)$$

$$b_1 \hat{T} + b_2 (\partial \hat{T} / \partial z) = 0, \quad (80)$$

$$b_3 \hat{C} + b_4 (\partial \hat{C} / \partial z) = 0, \quad (81)$$

$$b_5 (\partial \hat{W}_z / \partial z) + b_6 (\partial^2 \hat{W}_z / \partial z^2) = 0, \quad (82)$$

where b_1 , b_2 , b_3 , b_4 , b_5 , and b_6 are constants. Clearly $b_1 = b_4 = b_5 = 1$ and $b_2 = b_3 = b_6 = 0$ corresponds to eq. (78).

The boundary conditions at $z = z_L$ are not rigorous. In many solidification experiments, there is a rigid boundary at $z' = z_L$ (a constant), which implies that in our moving frame the boundary conditions should be applied at $z = z_L - Vt$. In addition, if $\rho_L \neq \rho_S$, the unperturbed flow is not zero at z_L . To take account of these effects would greatly complicate the calculation. We are basically assuming that as long as z_L is sufficiently far from the solid-liquid interface, the results will be relatively independent of the precise boundary conditions. The validity of this assumption has been shown by numerical calculations [3].

Numerical Methods

The linear homogeneous differential equations (62-67) for $\hat{W}_z(z)$, $\hat{T}(z)$, and $\hat{C}(z)$ are equivalent to eight first order equations with linear homogeneous boundary conditions at $z = 0$ [equations (70-73)] and $z = z_L$ [equations (79-82)]. The basic method for solving this eigenvalue problem as an initial value problem was discussed in our previous report^[3]. Here, we will describe three important modifications of the previous numerical algorithm, which permit calculations for a wider range of parameters.

The system of differential equations is solved using the SUPORT computer code developed by Scott and Watts [see references (7-11) for a detailed description of this code]. Basically, linearly independent solutions of the system of differential equations are calculated and then superimposed to satisfy the boundary conditions. The linear independence of the solutions is maintained by orthonormalizing the solutions whenever an impending loss of independence is detected^[7].

For $\sigma_i \neq 0$, the functions $\hat{W}_z(z)$, $\hat{T}(z)$, and $\hat{C}(z)$ are complex, and it is convenient to write them in terms of their real and imaginary parts to obtain sixteen first order real equations with eight boundary conditions at $z = 0$ and eight boundary conditions at $z = z_L$. For specified values of σ_i and c_∞ and fixed values of the remaining parameters in the differential equations and boundary conditions, one calculates eight linearly independent solutions all of which satisfy the boundary conditions at one endpoint. For particular values of σ_i and c_∞ (i.e., eigenvalues) a linear combination of these

eight solutions will satisfy the boundary conditions at the other endpoint. In general this will not be possible for our specified values of σ_1 and c_∞ and it is necessary to iterate to find the eigenvalues. As previously discussed^[3], a linear combination of the eight linearly independent solutions will satisfy the boundary conditions when the determinant of the coefficients vanish. In general this determinant is complex so that we want to find values of c_∞ and σ_1 such that the real and imaginary part of this determinant vanishes, i.e., we need to find the roots of two non-linear equations of two variables.

Keller^[12] has suggested an alternative method for solving eigenvalue problems which does not require the evaluation of a determinant. We have included Keller's suggestion as an option in our numerical code. Specifically, we temporarily replace the homogeneous boundary condition given by eq. (70) with the inhomogeneous boundary condition

$$(\partial^3 W_z / \partial z^3) = 1. \quad (83)$$

The SUPORT code provides a solution to this modified linear problem with inhomogeneous boundary conditions. In general, the homogeneous boundary condition, equation (70) will not be satisfied. We now vary c_∞ and σ_1 until equation (70) is satisfied. Since equation (70) is complex, it corresponds to two real equations and we again need to find the roots of two non-linear equations of two variables. At an eigenvalue clearly the determinant method and Keller's method are equivalent; however, they may have quite different convergence properties. For

the solidification problem treated here with $\sigma_i \neq 0$, Keller's method appears significantly better.

Our previous numerical code used the iteration method developed by Brown^[13] as implemented by Gay^[14]. In our present code, we are using the QN code developed by Shampine and Gordon^[15]. The QN code appears to require fewer function evaluations to find the eigenvalues.

In using the SUPORT code we choose an initial estimate for c_∞ and σ_i and solve the differential equations. The SUPORT code determines the orthogonalization points for this initial estimate for c_∞ and σ_i ; during succeeding iterations the orthogonalization points are not changed. This fixing of the orthogonalization is necessary when the determinant method is used to find the eigenvalues and is also used with Keller's method. The integration of the initial value problem is carried out using the Shampine-Gordon code^[16].

We have also written a code which assumes that $\sigma_i = 0$; in this case $\hat{W}(z)$, $\hat{T}(z)$, and $\hat{C}(z)$ are real and we have only eight first order equations. In addition, only c_∞ is varied to find an eigenvalue. This code requires considerably less computer time.

Numerical Results

A number of calculations have been carried out using parameters appropriate to the solidification of lead containing small quantities of tin. The specific values are given in Table 1. We have neglected the density change on solidification, i.e., $\epsilon = 0$, and kinetic effects, i.e., $\mu \rightarrow \infty$

In order to determine the accuracy of our numerical code, we have previously^[3] described a number of tests. In addition, we have compared magnetic field results with results given in Table XIV of Chandrasekhar^[6] and have compared oscillatory results with the analytic oscillatory convection results for free boundary conditions^[17].

The calculations correspond to unidirectional solidification upwards of a binary alloy which is rejecting ($k < 1$) a solute whose density is less than that of the solvent ($\alpha_c > 0$). We expect that for sufficiently small solute concentration there will be no convection, and the calculation will determine the bulk solute concentration above which convection occurs. This value c_∞^* depends on the spatial frequency ω of the perturbation and convection occurs if the actual concentration c_∞ exceeds c_∞^* for any value of ω , i.e., denoting the minimum value of c_∞^* as a function of ω by c_∞^{**} ; convection occurs if $c_\infty > c_\infty^{**}$. In all the calculations to date, the mode of instability at $c = c_\infty^{**}$ is not oscillatory, i.e., $\sigma_i = 0$. As will be discussed, we have found oscillatory modes but these do not correspond to the minimum value of c_∞^* .

The values of z_L were chosen such that $z_L \gg D/V$ and $\omega z_L \gg 1$. Under these conditions the results for c_∞^* are independent of z_L ; they are also independent of the precise boundary conditions at $z = z_L$ ^[3]. In Table 2 and Figure 1, we show c_∞^{**} as a function of growth velocity. As the growth velocity increases from 0.5 $\mu\text{m/s}$, there is a shallow minimum in c_∞^{**} followed by a rapid rise. At velocities slightly larger than 40 $\mu\text{m/s}$,

the minimum value of c_{∞}^* occurs at small wavelengths $\lambda = 2\pi/\omega$. We will denote this small wavelength instability as a morphological instability since the value of c_{∞}^{**} and ω at c_{∞}^{**} are not influenced by fluid flow, i.e., calculations taking account of fluid flow give the same results as the usual morphological stability theory^[18-19] which neglects fluid flow. The critical concentration and wavelength for morphological instability are denoted by $c_{\infty MS}$ and λ_{MS} , respectively, and are given in Table 2. Neglecting surface tension, the morphological stability criterion for interface stability is approximately $c_{\infty} < 7.7/V$ with V in $\mu\text{m/s}$.

Table 2 and Figure 1 also give the results of calculations for which $g = 10^{-4} g_e = 0.098 \text{ cm/s}^2$. The long wavelength instability at velocities less than $4 \mu\text{m/s}$ is strongly effected by this reduction in gravitational field. We will denote this long wavelength instability as a convective instability. However, it should be recognized that this convective instability gives rise to interfacial instability and that the morphological instability gives rise to fluid flow. The critical concentration for morphological instability is unaffected by the reduction in gravitational field. At velocities slightly larger than $4 \mu\text{m/s}$, the minimum value of c_{∞}^* corresponds to morphological instability. We note that although the critical concentration is substantially increased as the constant vertical gravitational field decreases from g_e to $10^{-4} g_e$, the critical concentration is still rather small for slow growth rates (less than 0.01 w/o at $V = 0.5 \mu\text{m/s}$).

In Table 3, for velocities of 1 and 20 $\mu\text{m/s}$, the effect of the temperature gradient in the liquid on the critical concentration for the onset of convective instability is indicated. For the larger velocity, the critical concentration is relatively insensitive to the magnitude of the temperature gradient. At the smaller velocity a change in temperature gradient from 50 to 1000 K/cm increases the critical concentration by an order of magnitude; the quantity $c_{\infty}^{**}/G_L^{3/4}$ is nearly constant. The frequency ω at the onset of convection is rather insensitive to the value of G_L for a given velocity.

Based on the assumptions previously discussed, the effect of a vertical magnetic field on the onset of convection is shown in Table 4 for velocities of 1, 5, and 20 $\mu\text{m/s}$. Magnetic fields of the order of a tesla are required to give an order of magnitude increase in the critical concentration. For the dimensionless parameter Q fixed at 9.0, the effect of magnetic field on c_{∞}^{**} increases with velocity. The frequency ω at the onset of convection becomes larger as the magnetic field is increased.

At small velocities the convective and morphological instabilities occur at quite different concentrations (see Table 2). In this case the concentration c_{∞}^{*} as a function of ω exhibits a rather simple behavior as illustrated in Figure 2 for $V = 5 \mu\text{m/s}$. Also shown are two higher eigenmodes. The system is unstable to a particular convective mode if the concentration lies above the curve for that mode. The lowest concentration c_{∞}^{**} above which convection occurs is $8.39(10^{-4})$ w/o at $\omega \cong 10$.

When the concentrations corresponding to convection and morphological instabilities are of the same order of magnitude, the concentration c_{∞}^* as a function of ω becomes rather complicated and oscillatory modes ($\sigma_1 \neq 0$) occur. This behavior is shown in Figures 3-6 for velocities of 30, 40, 50, and 80 $\mu\text{m/s}$, respectively. The dashed curves indicate oscillatory instabilities with the value of $\pm \sigma_1$ given in the inset of the graph (note that if σ is an eigenvalue, then the complex conjugate σ^* is also an eigenvalue). The solid curve in the lower right of the figures corresponds to the morphological instability mode; the minimum of this curve occurs at higher values of ω than are shown in the figure. For $V = 30, 40, 50$, and $80 \mu\text{m/s}$ this minimum occurs at $c_{\infty}^* = 0.28, 0.21, 0.18$ and 0.12 and $\omega = 620, 700, 750$, and 900 , respectively. These same values are also obtained if fluid flow is completely neglected. For $V = 30$ and $40 \mu\text{m/s}$, the minimum value of c_{∞}^* occurs at small wavelengths and corresponds to a non-oscillatory ($\sigma_1 = 0$) convective instability. For these velocities, $c_{\infty}^*(\omega)$ consists of two non-oscillatory branches both having a minimum with the absolute minimum corresponding to the convective mode. The two non-oscillatory branches are connected by an oscillatory mode indicated by the dashed line. For $V = 40 \mu\text{m/s}$, there is an additional oscillatory branch at low values of ω . The oscillatory instability occurs at concentrations higher than those required for morphological instability for the four velocities considered. For $V = 50$ and $80 \mu\text{m/s}$, the absolute minimum corresponds to the morphological instability

mode and the convective mode is oscillatory. The values of c_{∞}^* at the relative minimum in these oscillatory modes were indicated in Figure 1 by the dotted curve; the same procedure was also used for the relative minima for the morphological modes at $V = 30$ and $40 \mu\text{m/s}$. The values of σ_i for the oscillatory modes is of the order of 0.1 Hz or a period of the order of 60 s .

For $V = 80 \mu\text{m/s}$, a few calculations were carried out with the sign of α_c changed (i.e., a heavier solute rejected at the solid-liquid interface). The morphological stability mode extended to low frequencies and is a single-valued function of ω (in contrast to $\alpha_c > 0$; see Fig. 6). At low frequencies the values of c_{∞}^* were lower than those obtained by the usual morphological stability theory (which neglects fluid flow) while at large ω all calculations (α_c positive or negative or fluid flow neglected) gave the same results.

For simple boundary conditions, viz., $\hat{W}_z = (\partial^2 \hat{W}_z / \partial z^2) = \hat{T} = \hat{C} = 0$ at both boundaries, an analytic solution^[17] of a double diffusive convection problem is possible. In fact, this solution was used to check our numerical code. The neutral stability curves are of the form

$$R + S = 27\pi^4/4 \quad (84)$$

for $\sigma_i = 0$ and

$\{r^2 S / [(r+s)(1+r)]\} + \{s^2 R / [(r+s)(1+s)]\} = 27\pi^4/4$ for $\sigma_i \neq 0$, where R, S, r, s are the Rayleigh, solute Rayleigh, Prandtl, and Schmidt numbers, respectively. Both of the above expressions are of the form

$$S + a_1 R = a_2, \quad (85)$$

where a_1 and a_2 depend on the properties of fluid, viz., on the Prandtl and Schmidt numbers. For the present solidification problem the relevant length is (D/V) and we define Rayleigh numbers R' and S' based on (D/V) as

$$R' = -g\alpha G_L (D/V)^4 / \nu\kappa, \quad (86)$$

$$S' = -g\alpha_c G_c (D/V)^4 / \nu D = (g\alpha_c / \nu Dk) (1-k) (D/V)^3 c_\infty. \quad (87)$$

We now explore the possibility that the convective instabilities occurring during solidification can be qualitatively understood by an equation of the form

$$S' + a_1 R' = a_2. \quad (88)$$

To make a more direct comparison with the results of our numerical computations we rewrite this equation in dimensional form exhibiting only the V , G_L , c_∞ , and g dependence, i.e.,

$$c_\infty = a_3 V^3 / g + a_4 G_L / V, \quad (89)$$

where a_3 and a_4 depend on all variables other than V , G_L , c_∞ , and g , but perhaps have only a weak dependence on V , G_L , c_∞ , and g . The above equation has two limiting cases. For sufficiently large V , we have $c_\infty = a_3 V^3 / g$ while for sufficiently small V , $c_\infty = a_4 G_L / V$. If we now compare these two limits with our numerical results (see Figure 1 and Tables 2-3), we find qualitative agreement. For $V > 10 \mu\text{m/s}$, c_∞ is approximately proportional to V^3 , is insensitive to changes in G_L , and reduction in g from g_e to $10^{-4} g_e$ eliminates the convective instability, i.e., morphological instability governs the onset of

instability. For small V , c_∞ rises with decreasing V , is sensitive to changes in G_L and reduction in g is not as effective in eliminating the onset of convection. If one is simply interested in fitting the numerical results given in Tables 2-3, one can generalize the above expression in the form

$$S' + a_1 (R')^{a_5} = a_2, \quad (90)$$

or in dimensional form

$$c_\infty = a_3 V^3/g + a_4 (V^3/g) (gG_L/V^4)^{a_5}. \quad (91)$$

This expression can fit the 20 convective instability data points given in Tables 2 and 3 with a maximum error of 18%.

At small velocities, the wavelength at the onset of instability is very large, e.g., 5 cm at $V = 0.5 \mu\text{m/s}$. Clearly, in small tubes such wavelengths are not possible. Our calculation assumes infinite tube diameters, and it is non-trivial to modify the calculation to take account of the effects of the tube walls. To obtain some estimate of these effects one can assume that the tube walls simply prohibit small ω (large wavelength) convective modes. For example, for $V = 0.5 \mu\text{m/s}$, convective instability occurs at $c_\infty^{**} = 3.60 (10^{-4})$ w/o at $\omega = 1.2$; if we allow only perturbations with $\omega \geq 20 \text{ cm}^{-1}$ ($\lambda \leq 0.1\pi$), then instability occurs at a concentration of $1.62 (10^{-3})$ at $\omega = 20$.

At present we have not investigated the effects of fluid properties such as Prandtl and Schmidt numbers on the critical concentration for the onset of convection; such calculations appear worthwhile. For

lead containing tin, the maximum concentrations (regardless of growth velocity) below which there are no convective or morphological instabilities are 0.19 and 1.9 w/o for constant gravitational accelerations of 980 and $980 (10^{-4}) \text{ cm/s}^2$, respectively. For a given velocity, the change in critical concentration for the onset of convective instability due to a 10^{-4} reduction in gravitational acceleration is a strong function of velocity, ranging from a factor of 20 to 3000. Magnetic fields of the order of a tesla increase the critical concentration for convective instabilities by a factor of 10.

For concentrations such that convective instability has occurred, it would be of great interest to determine the effect of this convection on interface shape and the resulting solute distribution in the solidified material. A non-linear analysis is necessary for understanding the effects of fluid flow on solute distribution.

B. EXPERIMENT

Background for Experimental Work

The ability to solidify two-phase aligned structures from a wide range of compositions near a eutectic composition has importance in the full utilization of this class of composite materials. The early work of Mollard & Flemings^[20] claimed that the range of compositions for which plane front composite growth was possible was restricted not only by constitutional supercooling requirements but also by the requirement that convection be avoided. In fact, their experimental work using vertical solidification was limited to the Sn-rich side of the Sn-Pb eutectic wherein the fluid density influenced by temperature and composition always decreases with distance from the interface (height). Subsequently, others^[21-22] argued that as long as a stagnant boundary layer exists whose thickness is large compared to the lamellar spacing, plane front growth should be possible in the presence of convection. This was in fact verified by experiments by Holder & Oliver^[23] and Davis & Fryzuk^[21] who demonstrated the growth of Pb-rich Pb-Sn composites. Verhoeven, Kingery and Hofer^[24] subsequently showed that although composite growth was possible in the case of convection, that significant macrosegregation (10 w/o) down the length of solidified samples occurs in samples only 1 w/o on the Pb-rich side of the Pb-Sn eutectic.

The purpose of this research is to describe the microstructure and macrosegregation produced during the vertical solidification of off-eutectic alloys 3-6 w/o from the eutectic composition when the liquid

density near the interface increases with distance from the interface and to determine if a magnetic field or solidification downward can eliminate convection and hence macrosegregation.

Experimental Procedures

Alloys were prepared from 99.99% pure Sn and Pb in evacuated and sealed borosilicate crucibles. The directional solidification furnace is constructed of non-magnetic materials and has a bifilar wound cylindrical resistance heating element with upper and lower sections and a circulating water cooled chill zone. A silica tube containing the desired alloy is pulled down through the chill sealed by O-rings at constant velocity to accomplish directional solidification. The cooling water comes directly in contact with the silica tube. Using two separate A.C. proportional temperature controllers for the furnace, and water cooled by a heat exchanger, temperatures are constant to 0.1°C over an hour and 1°C in several days. The vertical drive is powered by a synchronous motor with a multi-speed gear box. Speeds from $0.5\text{ }\mu\text{m/s}$ to 0.5 mm/s are possible. The tube is attached to the pull shaft using a device which permits the sample to be suddenly pulled down about 3 cm to quench the liquid-solid interface.

Electrically insulated 0.25 mm diameter sheathed thermocouples were used to measure directly the temperature gradient in the liquid and the solid. The values of the measured liquid temperature gradient for all runs was $360\text{ K/cm} \pm 10\text{ K/cm}$. The furnace is designed so that a permanent magnet with a pole diameter of 8 cm and a pole separation

of 11 cm can be slid around the furnace to apply a 0.1T (1 kilogauss) horizontal magnetic field. Alternately, an 11 cm diameter solenoid can also be placed over the furnace-chill to apply up to 0.1T vertical magnetic field. Additionally the furnace can be inverted for solidification vertically downward. Here a graphite plug is used to maintain a small upward pressure on the inverted melt to prevent separation of the liquid from the freezing solid.

A specific directional solidification experiment is conducted in the following manner. A tube filled with the desired alloy is inserted through the chill, with the alloy completely in the chill section. A vacuum is pulled on the tube and the furnace temperature is equilibrated for several hours. The sample is then driven quickly into the furnace melting about 12 cm of alloy. The tube is backfilled with argon and temperatures are allowed to stabilize for about 1 minute. Excessive holding times at this stage are undesirable because a layer of Pb-rich solid solution will slowly solidify and disrupt the initial liquid composition uniformity. The tube is then pulled at the desired rate until about 6 cm have solidified. The remainder of the sample is then quenched delineating the liquid-solid interface in the microstructure. The silica is removed with HF acid and the specimens are mounted in a cool-setting epoxy for characterization.

Samples are routinely examined in a longitudinal section (parallel to the solidification direction) using standard metallographic techniques. When necessary, transverse sections are also taken. For each

experiment the shape of the liquid-solid interface is examined to be certain that heat flow was unidirectional. In the present experiments, the macroscopic liquid-solid interface of two-phase composite growth, when achieved, was concave outward by only 10-20 μm across a 3 mm diameter sample. Whether the structure is dendritic, lamellar, or whether there are any signs of growth rate fluctuations was also determined.

Measurement of macrosegregation down the length of directionally solidified samples was performed using two methods, x-ray fluorescence and wet chemistry. The former method, which was described previously [3], uses incident monochromatic (22.2 keV) x-rays collimated to 1/2 mm x 1/2 mm. The use of x-rays permits deeper penetration into and hence better averaging over the two-phase structure present in the samples than does the use of electron probe methods. This data was used to non-destructively evaluate the extent of macrosegregation and to indicate those samples for which wet chemistry would be used. Wet chemistry using a titration method^[25] was performed on approximately 2 mm discs cut transverse to the growth direction. Accuracy of the wet chemistry is approximately ± 0.25 w/o Pb.

Experimental Results

In all experiments conducted on the Pb-rich side of the eutectic, solidification begins with the dendritic growth of the Pb-rich phase despite the fact the G_L/V (temperature gradient in the liquid at the interface/growth velocity) substantially exceeds the requirement of

constitutional supercooling for the bulk composition of the alloy. The volume fraction of dendrites decreases slowly as a function of distance as shown in Figure 7, until the structure is two-phase composite. The region of dendritic growth in most instances is very long compared to D/V (where D is the liquid interdiffusion coefficient) and does not correspond to an initial transient of the type described by Flemings^[20]. Table 5 is a summary of experiments showing the bulk composition (C_o), growth rate (V), G_L/V , D/V , the initial length of the liquid alloy (L), the length of the dendritic zone (Z^D), and other parameters to be discussed later.

Figure 8 shows the composition as a function of fraction solidified (f_s) for two 43.7 w/o Pb alloys solidified at 0.5 $\mu\text{m/s}$ with total initial melt lengths of 5.2 cm and 11.8 cm respectively. [The eutectic composition is 38.1 w/o Pb.] The initial solid composition is very high in Pb content (the boundary of the two phase field occurs at 81 w/o Pb), and falls to the vicinity of the eutectic composition as solidification proceeds. The position in the samples where the dendritic structure ends is at a f_s of 0.12 and 0.11 respectively, where f_s is fraction solidified. Because of the excellent agreement of the macrosegregation of these two samples as well as the dendrite disappearance position, it is apparent that fraction solidified is the proper variable to describe changes in composition. This fact suggests strongly that the dendritic zone is not caused by an initial transient but by macrosegregation. Henceforth in this paper we will use fraction solidified as the length parameter to describe macrosegregation.

Figure 9 shows the composition as a function of fraction solidified for a 43.7 w/o Pb alloy solidified at 2.6 $\mu\text{m/s}$. With the increased velocity, the degree of macrosegregation is less and the transition to lamellar composite structure occurs at a larger fraction solid (0.23) than for the sample run at 0.5 $\mu\text{m/s}$.

Figures 10 and 11 shows data for 40.7 w/o Pb alloys solidified at 5.1 $\mu\text{m/s}$ and 1.3 $\mu\text{m/s}$ along with the position of dendrite disappearance. Table 5 includes the solid composition at the position of dendrite disappearance (C_s^D) and the solid composition at $f_s = 0$ obtained by extrapolating the macrosegregation curves.

Conclusions and Discussion

The extensive macrosegregation shown in Figures 8 through 11 occurs only for alloys on the Pb-rich side of the eutectic when freezing vertically upward. Experiments performed by the present authors on the Sn-rich side of the eutectic under identical conditions as the Pb-rich experiments exhibit only a relatively small amount of macrosegregation produced by thermal diffusion. The measured macrosegregation on the Sn-rich side agrees with previous work of Verhoeven, Warner & Gibson^[26] using their equation (17) with a thermal diffusion coefficient of $2.1 \times 10^{-8} \text{ cm}^2/\text{s-K}$ ($D = 0.6 \times 10^{-5} \text{ cm}^2/\text{s}$) and no mixing near the liquid solid interface (δ large). This absence of significant macrosegregation on the Sn-rich side in experiments conducted under identical conditions with those on the Pb-rich side is strong evidence that solutal convection and not ordinary thermal convection is the cause of the extensive macrosegregation on the Pb-rich side of the eutectic.

A qualitative model for the macrosegregation and resultant changes in microstructure is apparent. Solutal convection is sufficiently vigorous to disrupt the normal diffusion controlled (Sn-rich) solute field near the liquid solid interface regardless of whether it is planar or dendritic. This solute is transported by the convection to the bulk liquid far from the interface which is almost always well mixed* by the radial temperature gradients which exist there^[26]. Hence the bulk liquid, which initially was of composition C_0 on the Pb-rich side of the eutectic, gradually becomes more Sn-rich. This causes a slow change in the solid to compositions which are also more Sn-rich as solidification proceeds. Qualitatively the situation is identical to the case of normal solidification for single phase materials^[27] or Verhoeven et al.^[26] for plane front two-phase solidification. The transition from dendritic to composite structure occurs when the solid composition is close enough to the eutectic composition that plane front composite growth is stable. When the bulk liquid composition approaches the eutectic composition, solutal convection ceases. Macrosegregation after this point is caused only by thermal diffusion.

A quantitative description of the location of dendrite disappearance is possible. Figure 12 is a plot of G_L/V vs. the composition of the solid at the position where the structure changed from dendritic to composite.

* In the present experiments the composition of the liquid determined after quenching was constant to within ± 0.25 w/o Pb. The solute boundary layer was too thin to be detected.

It resembles the expected form of the relation between G_L/V vs. composition for the stability of plane front solidification, i.e., it falls slightly below the requirement of the simple constitutional supercooling criterion

$$G_L/V = - m/D (C_E - C_S) \quad (92)$$

where m is the liquidus slope of the Pb-rich phase. It also agrees with the limited data of Davis & Fryzuk^[21] on zone melted off-eutectics where macrosegregation is avoided by the fact that solid of constant composition is fed into the melted zone. Hence, it is a conclusion of this paper that the transition from dendritic to composite structure occurs when the composition of the solid satisfied a stability criterion for plane front growth of a composite.

Quantitative description of the observed macrosegregation is more difficult. Verhoeven et al.^[24,26] using a thermotransport-corrected Burton-Prim-Slichter^[27] type analysis of plane front composite growth has formulated an expression to predict macrosegregation. The 40.7 w/o Pb sample run at 5.1 $\mu\text{m/s}$ is dendritic for an extremely short distance (long compared to D/V) and hence this analysis is applicable. Using a value of the thermotransport coefficient D' mentioned previously, a value of 90 μm for δ , the thickness of the unmixed zone near the interface, gave the best fit to the measured data in close agreement with Verhoeven. This calculated curve of the macrosegregation is shown superimposed on the data of Figure 10. In this experiment, it was determined experimentally that the liquid composition remained on

the Pb-rich side of the experiment up to the quench point and solutal convection probably existed throughout this experiment. The calculated value of the bulk liquid composition using this value for δ also agreed to within 0.25 w/o of the measured composition of the quenched liquid.

Samples with large regions of dendritic growth cannot be fit with this equation. Clearly the existence of the dendritic interface influences both the driving force for solutal convection and the geometry for the flow. In the data shown in Figure 9 a substantial number of data points exist in the dendritic zone of the sample and a marked change in slope occurs as the volume fraction of dendrites decreases. Quantitative description of these curves is a topic for future research.

It is significant to note two aspects of solutal convection observed in this research. There is no evidence to suggest that as the concentration of the bulk liquid approaches the eutectic composition during solidification (and hence the concentration gradient goes to zero) that the convection becomes less vigorous. For example, in Figure 10, there is no systematic deviation of the data from the calculated curve which might suggest that δ , the width of the unmixed zone, increased as the liquid composition reached the eutectic composition. Additional evidence on this point is seen in Figure 8, where the sharp break in the data at a f_s of about 0.25 marks the transition from macrosegregation caused by solutal convection to macrosegregation caused by thermal diffusion. This sharp transition from regimes of convection to no convection may be reflected in the extremely low concentrations (i.e., deviation from eutectic composition)

required for the onset of convection described in Section A of this report. Additionally, the fact that containers as small as 3 mm used for this work do not apparently suppress convection may be reflected in the rather small change of critical composition for the onset of convection as a function of w discussed in Section A.

The presence of growth rate fluctuations have been observed in some cases in the present study. However, as can be seen for example in Figure 7, many samples have been obtained which contain no fluctuations. Hence, it is the belief of these authors that these fluctuations are caused by artifacts, such as for example, by nonsteady thermal contractions^[28]. Solutal convection seems to be sufficiently steady as to not cause growth rate fluctuations.

Future work on this contract will involve experiments under magnetic field and solidification downward to determine if solutal convection can be suppressed. Also attempts will be made to predict quantitatively the extent of macrosegregation during the dendritic growth of these off-eutectic alloys.

Acknowledgements

We acknowledge the substantial contributions of Professor Robert F. Sekerka of Carnegie-Mellon University and Consultant to the National Bureau of Standards to the theoretical part of this research. We would also like to thank Barry I. Diamondstone for the wet chemical analysis and J. R. Carruthers, M. Kuriyama, and R. G. Rehm for helpful discussions.

References

- [1] J. R. Carruthers, Preparation and Properties of Solid State Materials, Vol. 3, Eds. W. R. Wilcox and R. A. Lefever (Marcel Dekker, Inc., New York, 1977) p. 1.
- [2] D. T. J. Hurle, Current Topics in Materials Science, Vol. 2, Eds. E. Kaldis and H. J. Scheel (North-Holland, Amsterdam, 1977) p. 549.
- [3] W. J. Boettinger, S. R. Coriell, F. S. Biancaniello, and M. R. Cordes, NBS: Properties of Electronic Materials, Eds. J. R. Manning and R. L. Parker (NBSIR 78-1483, National Bureau of Standards, Washington, D. C.) p. 15.
- [4] D. D. Joseph, Stability of Fluid Motions I and II (Springer-Verlag, Berlin, 1976).
- [5] G. Z. Gershuni and E. M. Zhukhovitskii, Convective Stability of Incompressible Fluids (Keter, Jerusalem, 1976).
- [6] S. Chandrasekhar, Hydrodynamic and Hydromagnetic Stability (Oxford, London, 1961).
- [7] M. R. Scott and H. A. Watts, SIAM J. Numer. Anal. 14, 40 (1977).
- [8] M. R. Scott and H. A. Watts, SAND 75-0198, Sandia Laboratories, Albuquerque, New Mexico, 1975.
- [9] B. L. Darlow, M. R. Scott, and H. A. Watts, SAND 77-1328, Sandia Laboratories, Albuquerque, New Mexico, 1977.
- [10] B. L. Darlow, M. R. Scott, and H. A. Watts, SAND 77-1690, Sandia Laboratories, Albuquerque, New Mexico 1977.

- [11] M. E. Lord and H. A. Watts, SAND 78-0522, Sandia Laboratories, Albuquerque, New Mexico 1978.
- [12] H. B. Keller, Numerical Solution of Two Point Boundary Value Problems (Society for Industrial and Applied Mathematics, Philadelphia 1976).
- [13] K. M. Brown, SIAM J. Numer. Anal. 6, 560 (1969).
- [14] D. M. Gay, CNA-109 (Center for Numerical Analysis, The University of Texas at Austin) Dec. 1975.
- [15] L. F. Shampine and M. K. Gordon, SAND 75-0450, Sandia Laboratories, Albuquerque, New Mexico 1975.
- [16] L. F. Shampine and M. K. Gordon, Computer Solution of Ordinary Differential Equations - The Initial Value Problem (W. H. Freeman, San Francisco, 1975).
- [17] J. S. Turner, Buoyancy Effects in Fluids (Cambridge, London, 1973), Chapter 8.
- [18] R. F. Sekerka, Crystal Growth: An Introduction, Ed. P. Hartman, (North-Holland, Amsterdam, 1973) p. 403.
- [19] R. T. Delves, Crystal Growth, Vol. 1, Ed. B. R. Pamplin (Pergamon, Oxford, 1974) p. 40.
- [20] F. R. Mollard and M. C. Flemings, Trans. AIME 239, 1534 (1967).
- [21] K. G. Davis and P. Fryzuk, Can. Met. Quart. 10, 273 (1971).
- [22] J. D. Verhoeven and R. H. Homer, Met. Trans. 1, 3437 (1970).
- [23] J. D. Holder and B. F. Oliver, Met. Trans. 5, 2423 (1974).

- [24] J. D. Verhoeven, K. Kingery and R. Hofer, Met. Trans. 6B, 647 (1975).
- [25] M. J. Tschetter and R. Z. Bachman, Talanta 21, 106 (1974).
- [26] J. D. Verhoeven, J. C. Warner, E. D. Gibson, Met. Trans. 3, 1437 (1972).
- [27] J. A. Burton, R. C. Prim, and W. P. Slichter, J. Chem. Phys. 21, 1987 (1953).
- [28] J. D. Verhoeven and E. D. Gibson, J. Cryst. Growth 10, 235 (1971).

Table 1. Values Used in Numerical Calculations
(unless otherwise stated)

ν (kinematic viscosity)	$2.43(10^{-3})$	cm^2/s
κ (thermal diffusivity)	.108	cm^2/s
η (magnetic diffusivity)	$7.6(10^3)$	cm^2/s
D (diffusion coefficient)	$3.0(10^{-5})$	cm^2/s
g (acceleration of gravity)	980.0	cm/s^2
α (thermal coefficient of expansion)	$1.15(10^{-4})$	K^{-1}
α_c (solutal coefficient of expansion)	$5.2(10^{-3})$	$(\text{w/o})^{-1}$
ρ_0 (density of Pb at melting point)	10.66	gm/cm^3
k_L (thermal conductivity)	.159	J/cmKs
κ_s (thermal diffusivity of solid)	.202	cm^2/s
k_s (thermal conductivity of solid)	.297	J/cmKs
L_v (latent heat per unit volume)	256.0	J/cm^3
m (liquidus slope)	-2.33	$\text{K}/(\text{w/o})$
T_M^Γ (capillary parameter)	$1.0(10^{-5})$	cmK
μ (kinetic coefficient)	∞	cm/sK
k (distribution coefficient)	0.3	
ϵ (fractional density change)	0	
r (Prandtl number ν/κ)	$2.25(10^{-2})$	
s (Schmidt number ν/D)	81.0	
κ_s/κ	1.87	
k_s/k_L	1.87	
G_L	200.0	K/cm

Table 2. Bulk concentrations, c_{∞}^{**} , at which instability first occurs as a function of velocity V ($G_L=200$ K/cm)

$$g = g_e = 980 \text{ cm/s}^2$$

$V (\mu\text{m/s})$	$c_{\infty}^{**} (\text{w/o})$	$\lambda (\text{cm})$	$D\omega/V$	$c_{\infty}^{\prime\prime} (\text{w/o})$	$c_{\infty\text{MS}} (\text{w/o})$	$\lambda_{\text{MS}} (\text{cm})$
0.5	$3.60(10^{-4})$	5	0.7	1.14	15.5	0.039
1.0	$3.16(10^{-4})$	2.4	0.8	0.57	7.76	0.031
2.5	$4.10(10^{-4})$	1.0	0.7	0.23	3.13	0.024
5.0	$8.39(10^{-4})$	0.6	0.6	0.11	1.58	0.019
10.0	$3.10(10^{-3})$	0.4	0.4	0.057	0.804	0.015
20.0	$1.89(10^{-2})$	0.26	0.36	0.028	0.412	0.012
30.0	$6.40(10^{-2})$	0.18	0.35	0.019	0.281	0.010
40.0	$1.86(10^{-1})$	0.14	0.34	0.014	0.215	0.009
50.0	$1.75(10^{-1})$	0.008	4.5	0.011	0.175	0.008
80.0	$1.16(10^{-1})$	0.007	3.4	0.0071	0.116	0.007

$$g = 10^{-4} g_e$$

0.5	$8.4(10^{-3})$	6	0.6	1.14	15.5	0.039
1.0	$3.09(10^{-2})$	4	0.5	0.57	7.76	0.031
2.5	$3.63(10^{-1})$	2.2	0.34	0.23	3.13	0.024
4.0	1.87	1.4	0.34	0.14	1.97	0.021

See Table 1 for values of physical quantities used in the calculations. For $c_{\infty} < c_{\infty}^{\prime\prime}$, the unperturbed density is a monotonically decreasing function of height.

Table 3. Bulk concentrations, c_{∞}^{**} , at which instability first occurs as a function of temperature gradient G_L

<u>V($\mu\text{m/s}$)</u>	<u>G_L (K/cm)</u>	<u>$c_{\infty}^{**}(\text{w/o})$</u>
1.0	50.0	$1.15(10^{-4})$
1.0	100.0	$1.89(10^{-4})$
1.0	200.0	$3.16(10^{-4})$
1.0	400.0	$5.37(10^{-4})$
1.0	1000.0	$1.11(10^{-3})$
20.0	50.0	$1.88(10^{-2})$
20.0	100.0	$1.86(10^{-2})$
20.0	200.0	$1.89(10^{-2})$
20.0	400.0	$1.95(10^{-2})$
20.0	1000.0	$2.10(10^{-2})$

Table 4. Bulk concentrations, c_{∞}^{**} , at which instability first occurs as a function of magnetic field H_{0z} ($\sigma_i=0$ assumed)

$V(\mu\text{m/s})$	$c_{\infty}^{**}(\text{w/o})$	$D\omega/V$	$H_{0z}(\text{T})$	Q
1.0	$3.16(10^{-4})$	0.8	0.0	0.0
1.0	$3.55(10^{-4})$	0.9	0.050	9.0
1.0	$3.09(10^{-3})$	2.7	1.00	$3.6(10^3)$
5.0	$8.39(10^{-4})$	0.6	0.0	0.0
5.0	$1.90(10^{-3})$	0.8	0.25	9.0
5.0	$4.16(10^{-3})$	1.0	0.50	$3.6(10^1)$
5.0	$1.16(10^{-2})$	1.1	1.00	$1.4(10^2)$
5.0	$5.70(10^{-2})$	1.5	2.50	$9.0(10^2)$
20.0	$1.89(10^{-2})$	0.36	0.0	0.0
20.0	$2.63(10^{-2})$	0.42	0.25	0.56
20.0	$4.19(10^{-2})$	0.53	0.50	2.25
20.0	$8.84(10^{-2})$	0.68	1.00	9.0

The dimensionless number^[6] $Q = (H_{0z} D/V)^2 / (4\pi\eta\nu)$ based on D/V as the relevant length; for the values used in these calculations $Q = 3.6(10^3) (H_{0z}/V)^2$ where H_{0z} is in T and V is in $\mu\text{m/s}$.

Table 5 - Summary of Experiments

C_o (w/o Pb)	V ($\mu\text{m/s}$)	$G_L/V \times 10^{-6}$ ($\text{K} \cdot \text{s}/\text{cm}^2$)	D/V (cm)	L (cm)	C_s (o) (w/o Pb)	C_s^D (w/o Pb)	Z^D (cm)	f_s^D
40.7	5.1	0.7	0.01	8.6	43.5	43.4	0.08	0.01
40.7	1.3	2.8	0.05	12.3	53	49.1	0.8	0.06
43.7	2.6	1.4	0.02	14.7	53	47.0	3.4	0.23
43.7	0.5	7.2	0.12	5.2	72	58.8	0.62	0.12
43.7	0.5	7.2	0.12	11.8	72	60.5	1.3	0.11

$$G = 360 \text{ K/cm}$$

$$D = 0.6 \times 10^{-5} \text{ cm}^2/\text{s}$$

$$C_E = 38.1 \text{ w/o Pb}$$

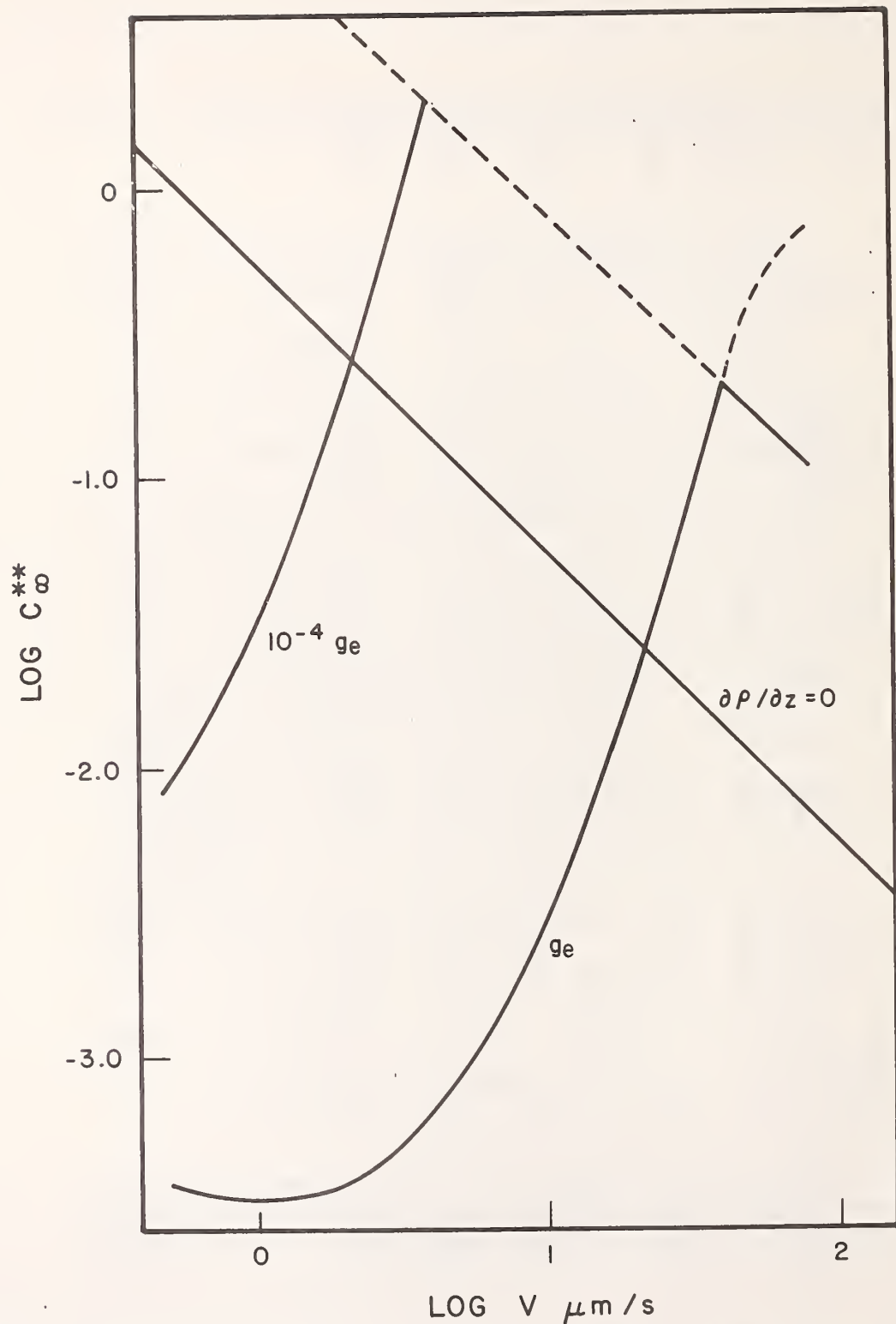


Fig. 1. The critical concentration c_{∞}^{**} above which instability occurs as a function of the velocity V of directional solidification of lead containing tin. The solid curves with positive slope represent the onset of convective instabilities for constant gravitational accelerations of $g_e = 980 \text{ cm/s}^2$ and $10^{-4} g_e$. The solid curve with negative slope represents the onset of morphological instability; the nearly parallel solid line labeled $(\partial \rho / \partial z) = 0$ represents the neutral density criterion.

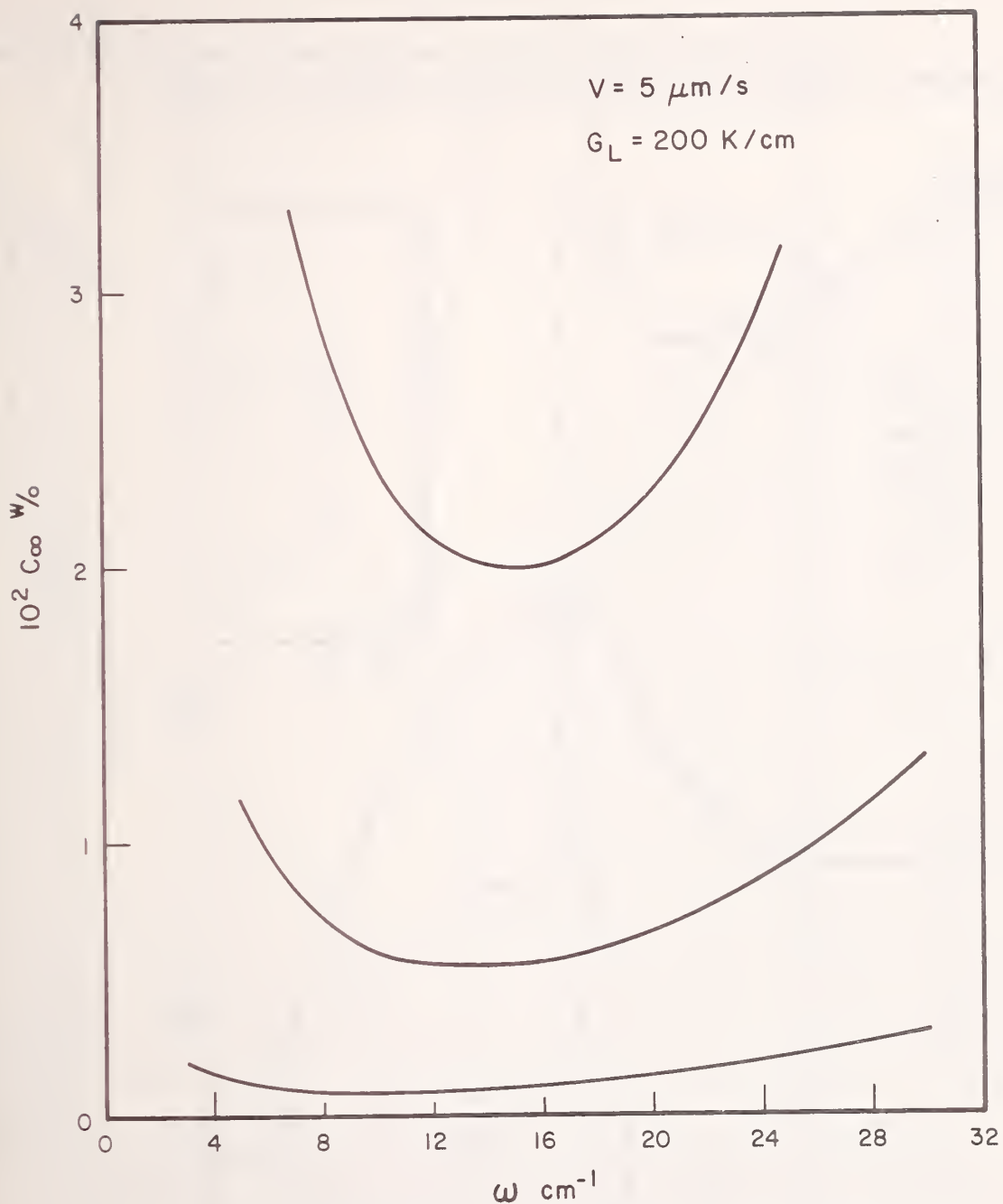


Fig. 2. The concentration at the onset of instability during directional solidification at $V = 5 \mu\text{m/s}$ for a dilute alloy of tin in lead as a function of the spatial frequency ω of a sinusoidal perturbation. Three eigenmodes are shown; the system is unstable with respect to a particular convective mode if the bulk concentration c_∞ lies above the curve for that mode. For $c_\infty < 8.4 \cdot 10^{-4}$ w/o, the system is stable with respect to all small perturbations.

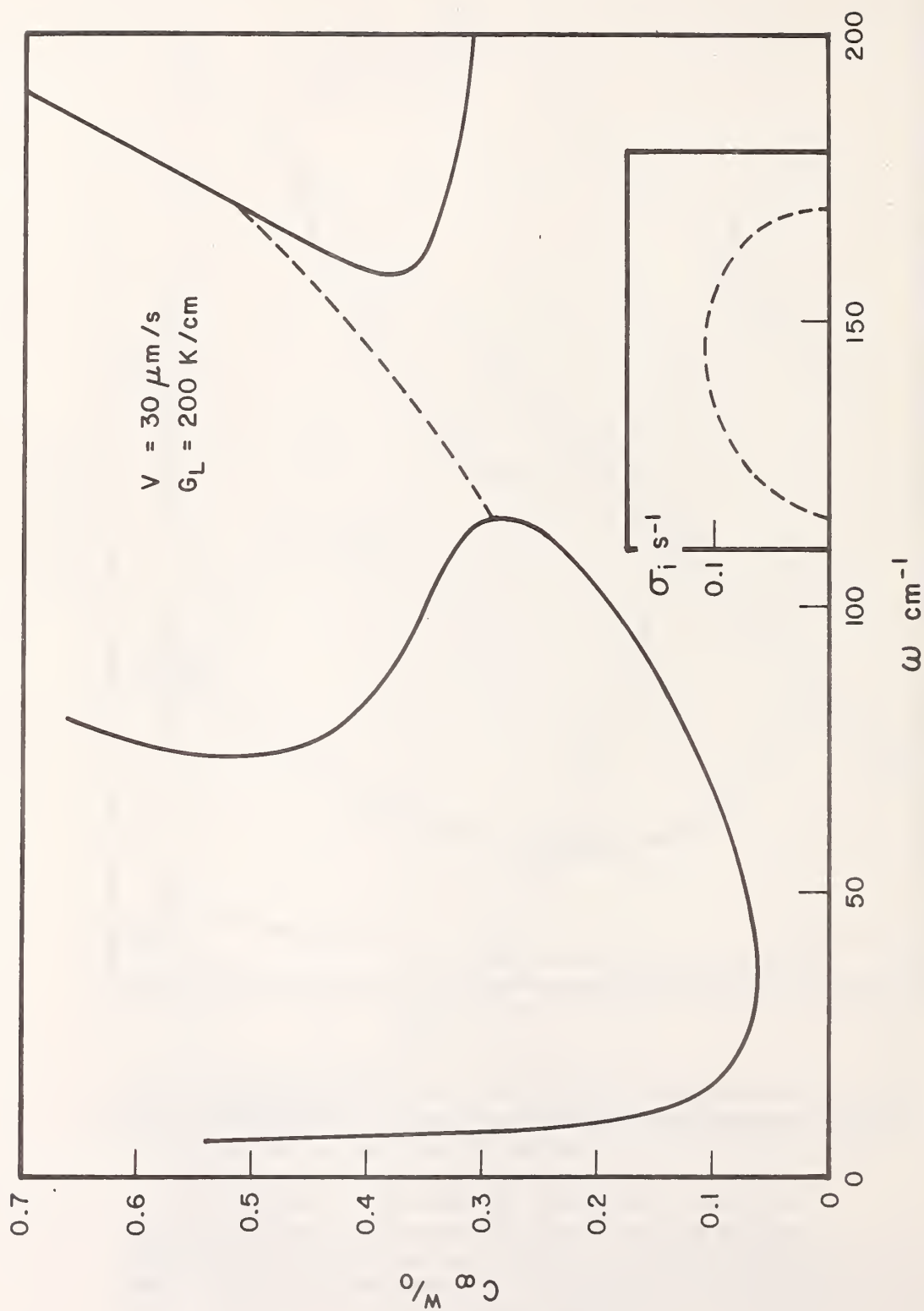


Fig. 3. The concentration at the onset of instability during directional solidification at $V = 30 \mu\text{m/s}$ of a dilute alloy of tin in lead as a function of the spatial frequency ω of a sinusoidal perturbation. The solid curves mark the onset of non-oscillatory instabilities ($\sigma_i = 0$); whereas the dashed curves mark the onset of oscillatory instabilities (the value of σ_i is given in the inset).

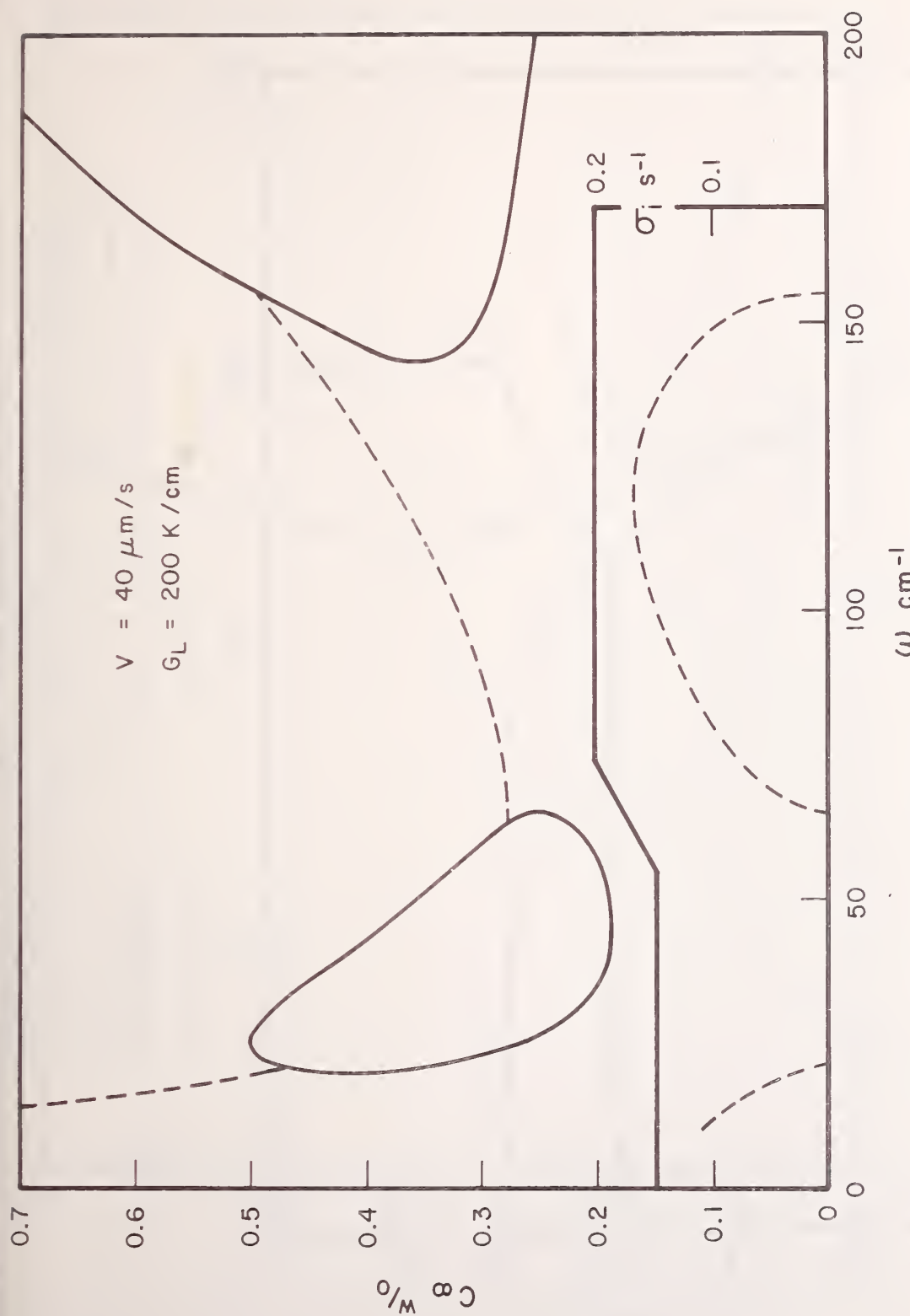


Fig. 4. The concentration at the onset of instability during directional solidification at $V = 40 \mu\text{m/s}$ of a dilute alloy of tin in lead as a function of the spatial frequency ω of a sinusoidal perturbation. The solid curves mark the onset of non-oscillatory instabilities ($\sigma_i = 0$); whereas the dashed curves mark the onset of oscillatory instabilities (the value of σ_i is given in the inset).

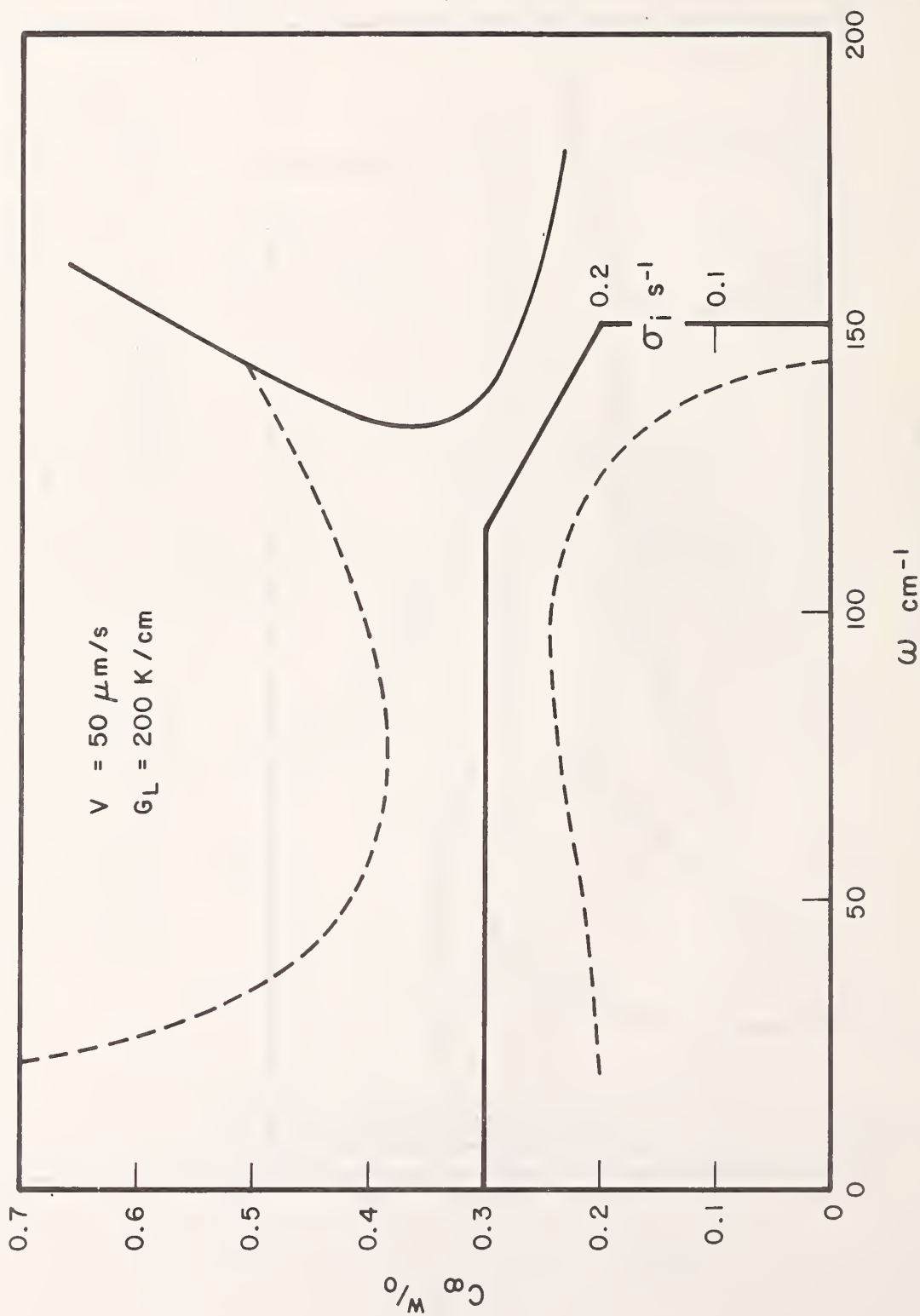


Fig. 5. The concentration at the onset of instability during directional solidification at $V = 50 \text{ } \mu\text{m/s}$ of a dilute alloy of tin in lead as a function of the spatial frequency ω of a sinusoidal perturbation. The solid curves mark the onset of non-oscillatory instabilities ($\sigma_i = 0$); whereas the dashed curves mark the onset of oscillatory instabilities (the value of σ_i is given in the inset).

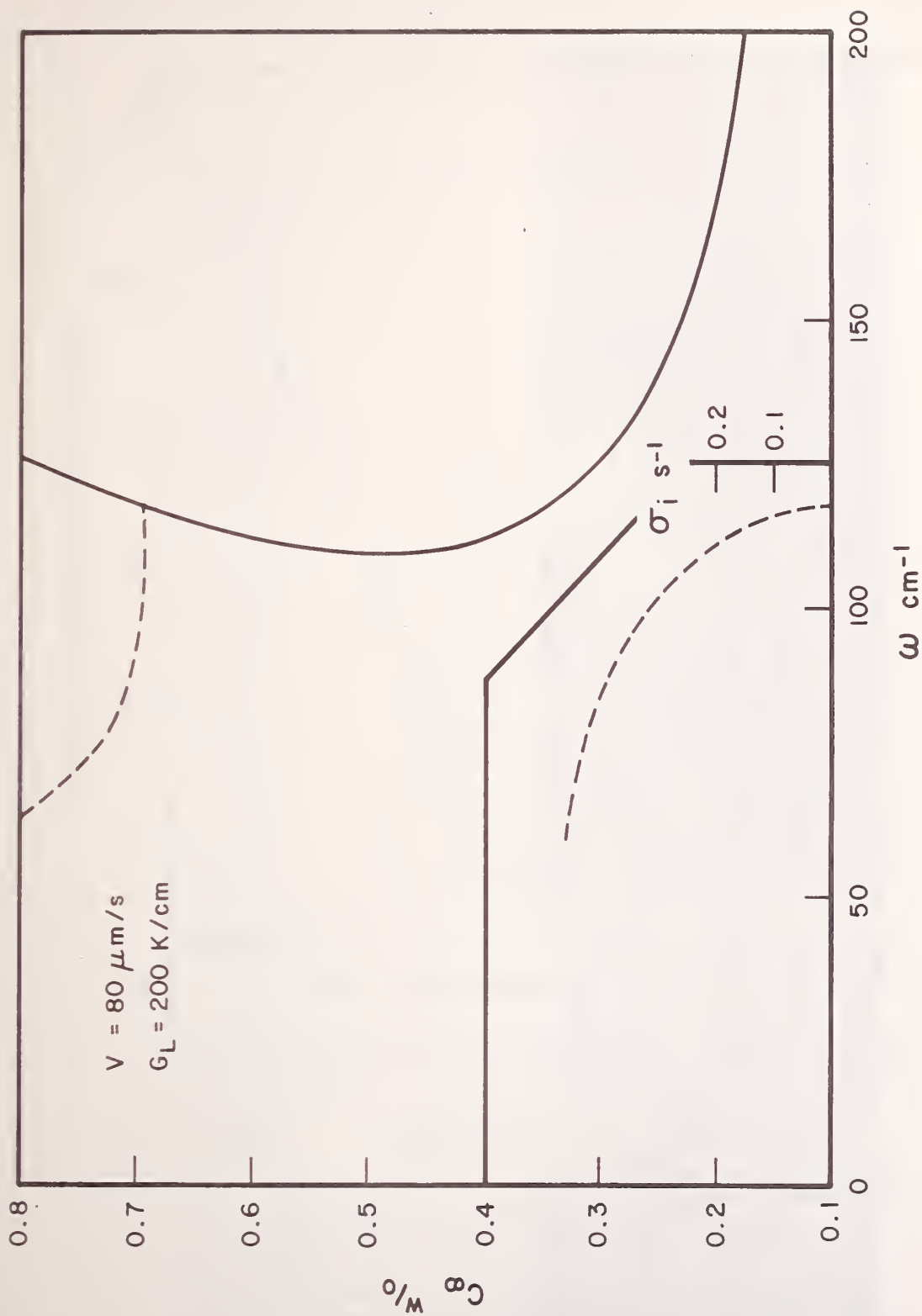


Fig 6. The concentration at the onset of instability during directional solidification at $V = 80 \mu\text{m/s}$ of a dilute alloy of tin in lead as a function of the spatial frequency ω of a sinusoidal perturbation. The solid curves mark the onset of non-oscillatory instabilities ($\sigma_i = 0$); whereas the dashed curves mark the onset of oscillatory instabilities (the values of σ_i is given in the inset).



Fig. 7. Longitudinal section of directionally solidified sample showing the change in volume fraction of Pb dendrites as a function of distance (fraction solidified). Solidification proceeded from left to right. At the extreme right there are no dendrites. Solidification velocity is $1.3 \mu\text{m/s}$ - original composition is 40.7 w/o Pb.

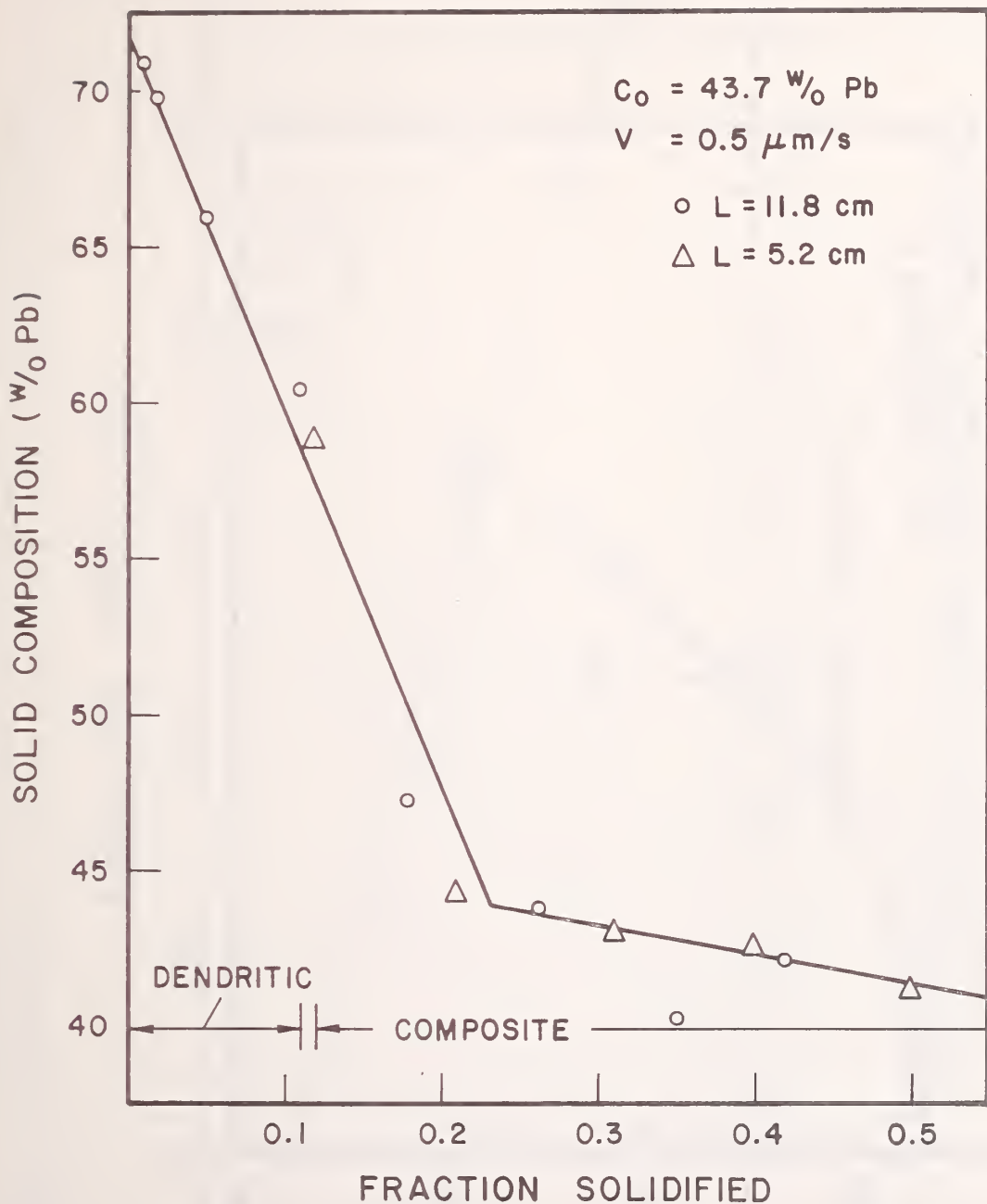


Fig. 8. Solid composition as a function of fraction solidified for two 43.7 w/o Pb samples of different length L , solidified at $0.5 \mu\text{m/s}$. Agreement shows fraction solidified to be an accurate parameter to describe these experiments. The regions of dendritic and composite growth are indicated. The sharp break in the curve is the demarcation between regions of macrosegregation induced by solutal convection and thermal diffusion.

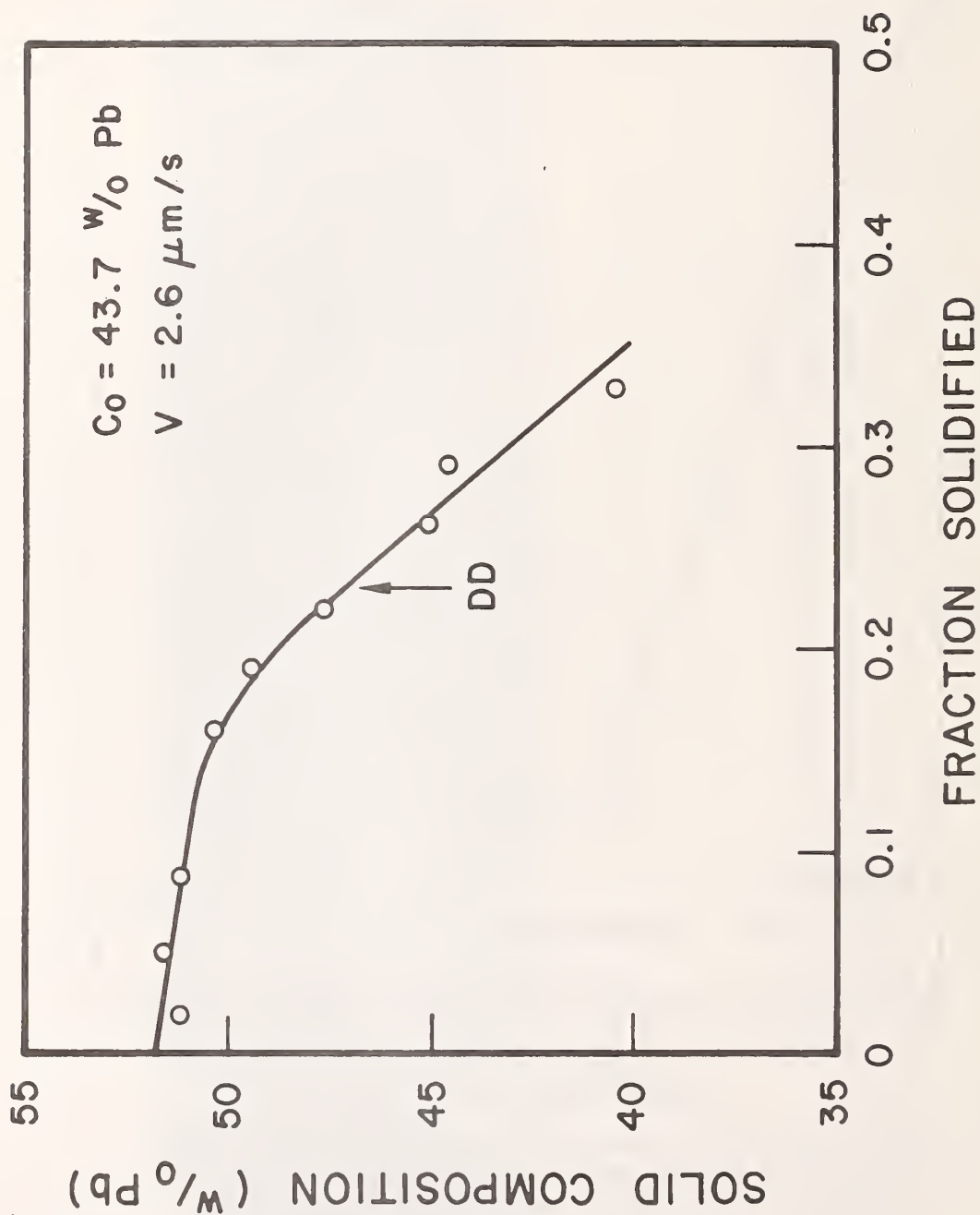


Fig. 9. Macrosegregation data for a 43.7 w/o Pb alloy solidified at $2.6 \mu\text{m/s}$. "DD" denotes the position where the volume fraction of Pb dendrites reached zero. The sample was quenched before the transition to thermal diffusion controlled macrosegregation.

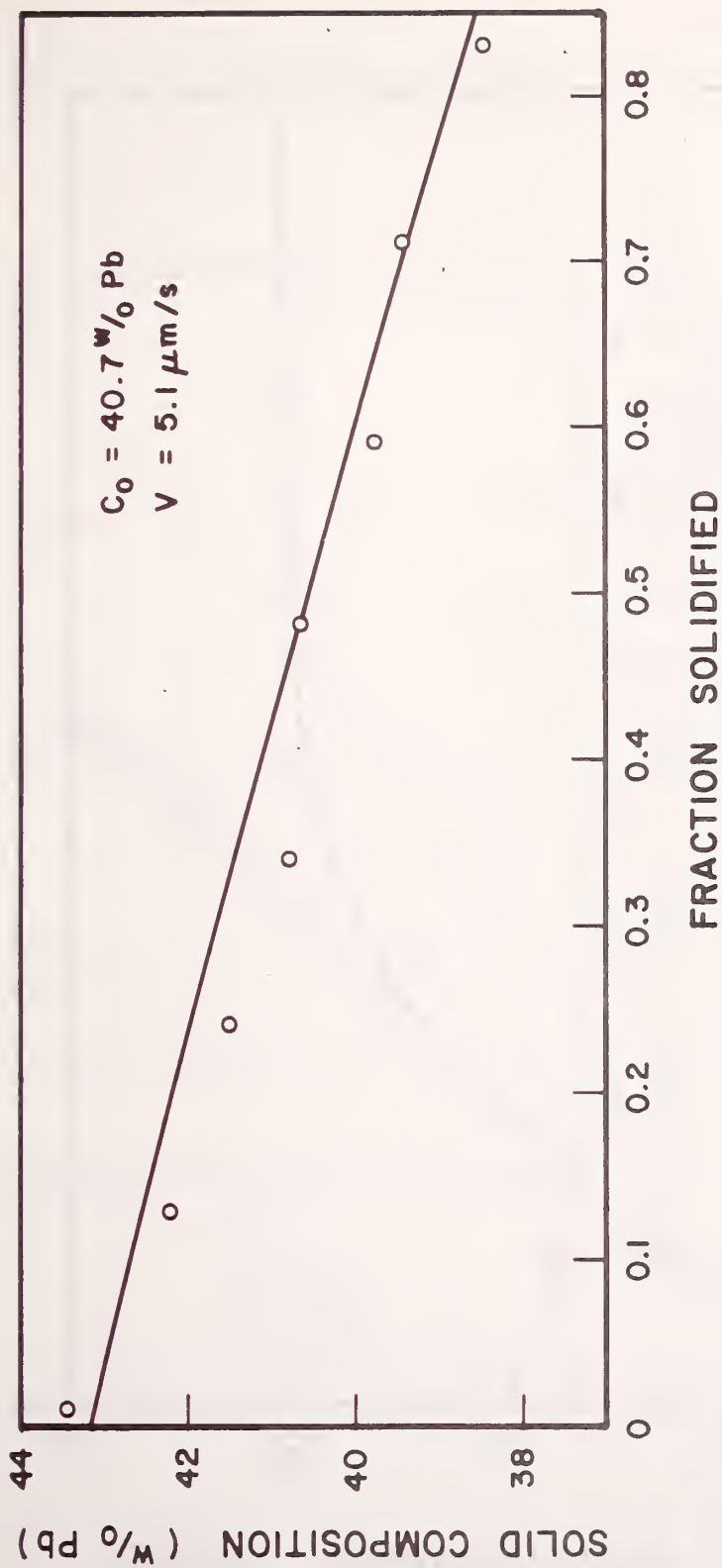


Fig. 10. Macrosegregation data for a 40.7 w/o Pb alloy solidified at 5.1 $\mu\text{m/s}$.
 The curve is the best fit of the data using only δ as a parameter
 using Verhoeven's equation (17) [26].

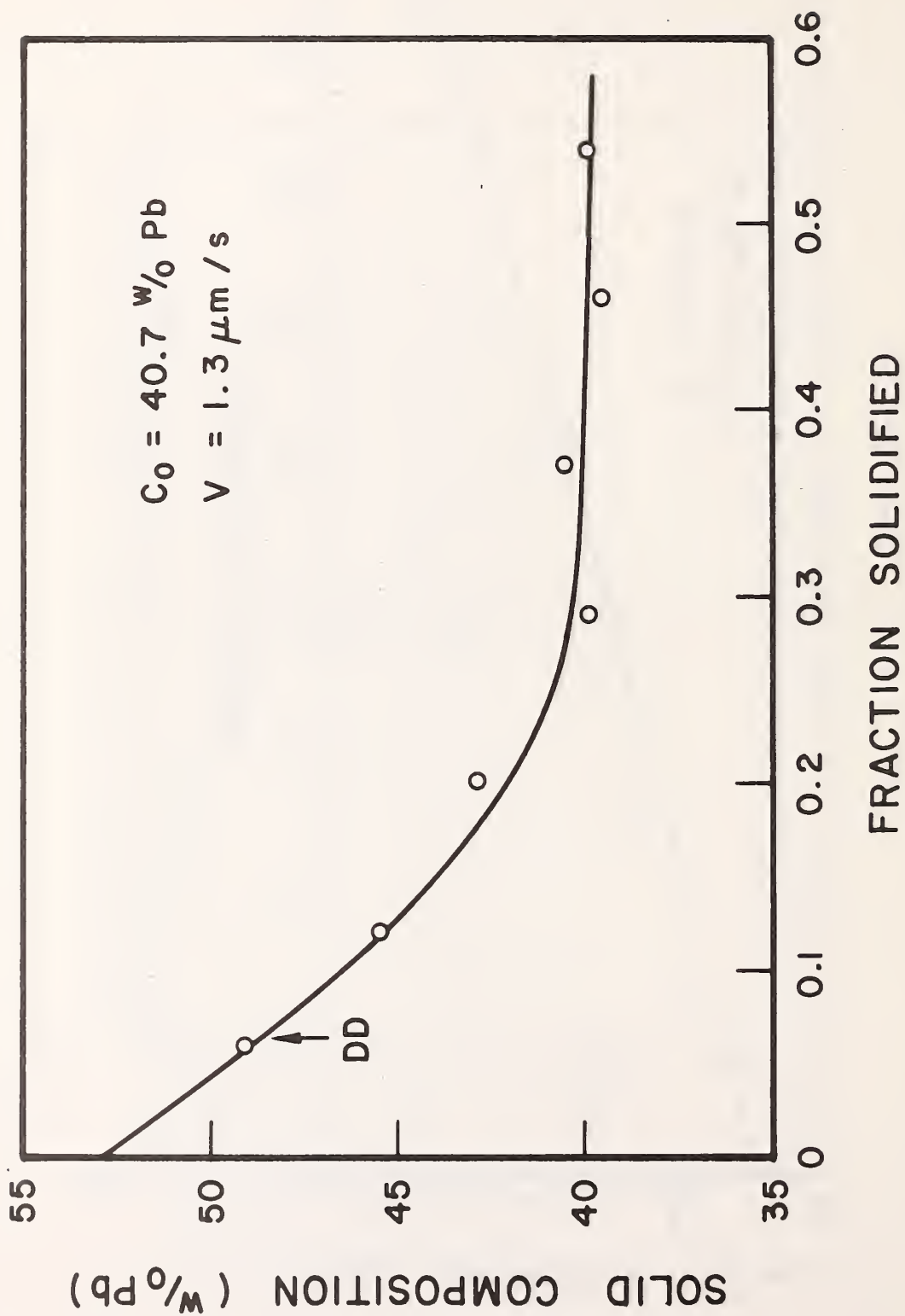


Fig. 11. Macrosegregation data for a 40.7 w/o Pb alloy solidified at $1.3 \mu\text{m/s}$.

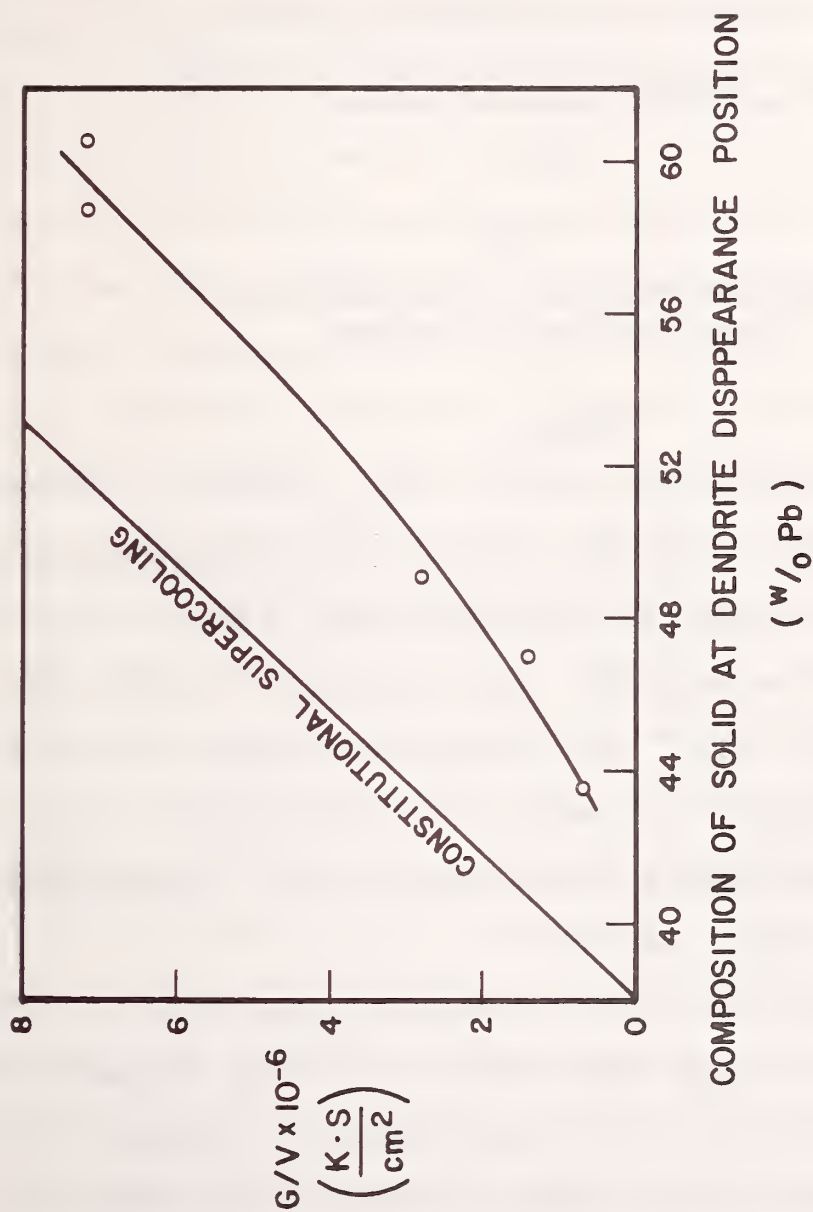


Fig. 12. A plot of G_L/V versus solid composition at the position of dendrite disappearance for all of the samples. The data follows the general trend of plane front interface stability for off-eutectic alloys.

Task 3

A Thermochemical Study of Corrosive Reactions in Oxide Materials

H. S. Parker, R. S. Roth and C. D. Olson

Ceramics, Glass and Solid State Science Division
Center for Materials Science

and

E. R. Plante

Chemical Stability and Corrosion Division
Center for Materials Science

Summary

Phase relationships in the K_2O - Fe_2O_3 system are described for the 80-100 mole percent Fe_2O_3 portion. Two structures analogous to the Na-Beta alumina structures were found, a β -type at about 85.2 mole percent Fe_2O_3 and a high temperature β''' -type at about 91 mole percent Fe_2O_3 . Vapor pressure measurements of the β -type indicate pressures of the order of 10^{-4} atm at $1300^\circ C$. Vacuum melting and low oxygen pressure heatings in open containers result in excessive sample volatility.

The chemical corrosion of platinum by compositions in the 80-100 mole percent Fe_2O_3 range appears to be minimal at temperatures up to $1600^\circ C$ although there is some evidence of diffusion of the volatile species into the platinum container. The absence of container attack may be attributed to the low amount of Fe^{+2} in the specimens at the pressures and compositions used in these experiments.

Introduction

The objectives of this task are to investigate the nature, extent and limitations on experimental studies imposed by sample-container reaction at high temperature and to evaluate containerless techniques for melt and solid state investigations. Alkali and transition elements are among the most reactive and are of great technological importance because of their application in the fields of MHD, fuel cells, catalysts and solid state electronic and ionic conductors. Reaction with the container can severely compromise the bulk composition of the sample and adversely affect the electrical and chemical properties. This, together with the inability in general to electromagnetically levitate ceramic materials, makes low gravity experiments attractive for containerless study of such materials.

The systems chosen as the initial experimental materials include the $\text{KFeO}_2\text{-FeO}_x$ system and the $\text{CaO-Y}_2\text{O}_3\text{-FeO}_x$ system. These systems are of interest not only because of the reactivity with container materials (particularly Fe^{+2}) and other ceramics but also because of their interesting electronic and ionic conductivity. Because of the high temperatures involved, the container choice is limited to the noble metals and their alloys for oxidizing atmospheres and to molybdenum, tantalum and tungsten for inert or reducing atmospheres.

The general approach is to: a) determine the maximum temperature limits for the container material and characterize the reaction products, b) determine the equilibrium phase assemblages and vapor pressures in selected portions of the systems within the limitations

imposed by a), and, c) in collaboration with MSFC provide specimens for acoustic levitation experiments at MSFC and characterize and correlate results of levitation experiments with container experiments to evaluate problems associated with low gravity experiments.

The work described in this report on the $\text{KFeO}_2\text{-FeO}_x$ system is a continuation of that undertaken during the previous contract year [1].

Experimental Procedures

A detailed description of the preparation of the compositions used for the quenching experiments described herein is given in the previous report [1], together with the characterization methods following heat treatment of each specimen.

The quench furnaces used were of a standard design, wound with Pt-Rh alloy wire and utilizing the furnace winding as one arm of an a.c. bridge for temperature control. For temperatures up to 1500°C , Pt-90Pt10Rh thermocouples were used for measurement. Above 1500°C , a disappearing filament optical pyrometer was utilized. The thermocouples and pyrometer were calibrated in situ against known melting points and suitable corrections applied.

Equilibrium at a given temperature was considered to have been reached when continued heating produced no further changes in the x-ray powder diffraction pattern of the specimen.

Experimental Results

A. Phase Equilibria and Specimen-Container Reaction (H. S. Parker, R. S. Roth and C. D. Olson)

The compositions and temperatures investigated are shown in Table 1 and Figure 1. Included in Figure 1 are some data from the previous report [1]. The β''' -alumina structure occurring in this system at compositions in the 90-92 mole percent " Fe_2O_3 " range has not been recognized previously, although the β -structure has been reported [2].

Attempts were made to heat specimens of the β''' composition in open platinum containers at 1200°C and partial pressures of oxygen in the 10^{-3} atm range, with the hope of increasing the $\text{Fe}^{+2}/\text{Fe}^{+3}$ ratio and thereby lower the observed minimum temperature of stability. These attempts were unsuccessful, in every case the only phase present after heat treatment was Fe_3O_4 . This suggests that the potassium volatility under these conditions is too great to allow the attainment of equilibrium in open containers. This is in contrast to similar specimens (90.9 mole percent " Fe_2O_3 ", Table 1) which ruptured the container during heating in air at 1450°C for 24 hours yet still contained only β''' .

As discussed in the previous report [1], little interdiffusion and minimal reaction was observed between the platinum container and a specimen of $\text{K}_2\text{O}:5.75\text{Fe}_2\text{O}_3$ (85.2 mole percent Fe_2O_3) after heating at 1475°C for 19 hours. Specimens of $\text{K}_2\text{O}:4\text{Fe}_2\text{O}_3$, $\text{K}_2\text{O}:11\text{Fe}_2\text{O}_3$, $\text{K}_2\text{O}:12\text{Fe}_2\text{O}_3$ and $\text{K}_2\text{O}:16\text{Fe}_2\text{O}_3$ (80, 91.7, 92.3 and 94.1 mole percent Fe_2O_3 , respectively) were heated at 1450°C for 20 hours in sealed

Table 1. The System KFeO_2 - Fe_2O_3 .

<u>Composition</u> mole percent		<u>Temp.</u> ^{a/} °C	<u>Time</u> hrs	<u>Results</u> ^{b/}
K_2O	Fe_2O_3			
20	80	1200	19	$\beta + \text{KFeO}_2$
		1450	20	partial melting. β
16.67	83.33	1200	19	$\beta + \text{tr } \beta''$
		1446	19	partial melting. β
15.4	84.6	1200	19	β
		1200	23	β
		1399	22	β
		1520	20	leaked. $\beta''' + \text{Fe}_3\text{O}_4$
14.3	85.7	1200	19	β
		1200	24	β
		1450	16	partial melting. β
12.5	87.5	1400	20	small leak. $\beta + \beta'''$
		1520	22	leaked. $\beta''' + \text{Fe}_3\text{O}_4$
11.1	88.9	1200	19	$\beta + \text{Fe}_2\text{O}_3$
		1325	16	$\beta + \text{Fe}_2\text{O}_3$
		1400	20	small leak. $\beta''' + \beta + \text{tr. Fe}_3\text{O}_4$
		1446	18	partial melting. $\beta + \beta'''$
10.0	90.0	1200	19	$\beta + \text{Fe}_2\text{O}_3$
		1396	20	$\beta + \text{Fe}_2\text{O}_3$
		1450	16	$\beta + \beta'''$
9.1	90.9	1200	19	$\beta + \text{Fe}_2\text{O}_3$
		1398	20	β'''
		1450	24	leaked. β'''
		1450	16	leaked. β'''
		1520	20	partial melting. $\text{Fe}_3\text{O}_4 + \beta + \beta'''$
8.3	91.7	1200	19	$\beta + \text{Fe}_2\text{O}_3$
		1200	24	$\beta + \text{Fe}_2\text{O}_3$
		1450	16	β'''
		1475	19	$\text{Fe}_3\text{O}_4 + \beta'''$
		1600	19	melted. $\beta''' + \text{Fe}_3\text{O}_4$

7.7	92.3	1400	20	$\text{Fe}_2\text{O}_3 + \beta$
		1450	20	$\beta'' + \text{Fe}_3\text{O}_4$
		1450	24	$\beta''' + \text{Fe}_3\text{O}_4$
5.9	94.1	1200	24	$\beta + \text{Fe}_2\text{O}_3$
		1400	20	$\beta + \text{Fe}_2\text{O}_3$
		1450	20	leaked. $\text{Fe}_3\text{O}_4 + \beta'''$
		1520	20	$\beta''' + \text{Fe}_3\text{O}_4$ <u>c/</u> (partial melting)
		1608	19	Fe_3O_4 <u>c/</u> (partial melting)
4.2	95.8	1200	24	$\text{Fe}_2\text{O}_3 + \beta$
		1396	20	$\text{Fe}_2\text{O}_3 + \beta$
		1520	20	$\text{Fe}_3\text{O}_4 + \text{tr } \beta$ <u>c/</u> (partial melting)

a/ All compositions calcined at 625°C for 18 hours, 800°C for 90 hours and 1000°C for 72 hours with periodic grinding prior to use in quenching experiments. All quenching experiments done in sealed platinum capsules.

b/ Based on visual observation for detection of melting and x-ray diffraction powder technique for phase identification.

c/ If partial melting occurred, presence of liquid phase could not be detected visually.

heavy wall (1.5 mm) platinum tubes and sectioned for SEM examination.

An empty heavy wall tube was given the same heat treatment for comparison.

In the $\text{K}_2\text{O}:4\text{Fe}_2\text{O}_3$ specimen, little sample-container reaction or interdiffusion was evident, as shown in Figure 2. The three pores which intersect the platinum surface, however, are rich in potassium and iron as shown by the maps in Figure 2c and 2d. Examination of all specimens at higher magnifications revealed a number of small pores, in a band, remote from the inner surface of the platinum tubes (see Figure 3, 4 and 5). No such porosity could be found in the empty

platinum tube given the same heat treatment. Figure 6 shows the platinum container wall used for heating a specimen of $K_2O:11Fe_2O_3$ and left exposed to laboratory air after SEM examination. These dendrites are rich in potassium and appear to be associated with pores and fissures in the platinum, suggesting potassium accumulation in these areas.

It is possible that these pores are the result of diffusion of the volatile species from the specimen along grain boundaries with subsequent agglomeration and pore development.

Specimens of $K_2O:7Fe_2O_3$ (87.5 mole percent " Fe_2O_3 ") were prepared from hot-pressed material in the form of discs, 1 cm diameter and 0.1 to 0.2 cm thick, spheres 0.2 to 0.6 cm in diameter, and small bars about 0.2 x 0.1 x 1 cm and supplied to MSFC for use in their acoustic levitation and drop tube melting experiments. The sample was melted in the drop tube apparatus, but melting was accompanied by extreme outgassing of the sample and electrical discharges in the apparatus, terminating the experiment. As discussed elsewhere in this section, the potassium and oxygen pressures in these samples are apparently too high for heating at high temperatures in vacuum or reduced oxygen pressures in open containers without seriously compromising the bulk composition and introducing difficult problems in design of experiments.

B. Vapor Pressure Studies (E. R. Plante)

Vapor pressure measurements yield useful data for projected containerless operations under zero gravity by helping to define conditions which minimize loss of volatile constituents. During

the current project year, vapor pressure measurements on the composition approximated by " $\text{K}_2\text{O}\cdot 6\text{Fe}_2\text{O}_3$ " were carried out and will be summarized in this section of the report. These measurements complement the vaporization studies on KFeO_2 -" $\text{K}_2\text{O}\cdot 7\text{Fe}_2\text{O}_3$ " which were summarized in the previous report [1]. The previous vaporization measurements were interpreted in terms of the reaction

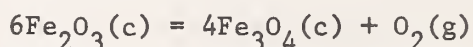
$$7/6 (\text{K}_2\text{O}\cdot \text{Fe}_2\text{O}_3) = 2\text{K}(\text{g}) + 1/2 \text{O}_2(\text{g}) + 1/6 (\text{K}_2\text{O}\cdot 7\text{Fe}_2\text{O}_3).$$

The composition of the β phase, " $\text{K}_2\text{O}\cdot 7\text{Fe}_2\text{O}_3$ ", is not known precisely. This phase may contain as little as 5.75 moles of Fe_2O_3 and has a small solid solution range in which additional Fe_2O_3 may be dissolved. Under the conditions of the vaporization experiments the oxygen pressure is self generated and the K_2O - Fe_2O_3 phase may become oxygen deficient. In fact, the vapor pressure measurements do indicate slight changes in the composition of the evaporating phase. However, in the interpretation of the vaporization data, the composition of the residue phase in the previous experiments, and the evaporating phase in the current experiments will be assumed to be $\text{K}_2\text{O}\cdot 6\text{Fe}_2\text{O}_3$.

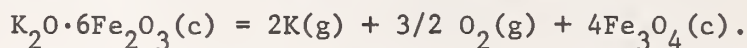
Vapor pressure measurements were made using a modulated beam quadrupole mass spectrometer. A molecular beam issuing from a Pt Knudsen cell was ionized by 30 V electrons and the major ions, K^+ and O_2^+ were alternately monitored. The mass spectrometer was calibrated using observed weight losses and integrated ion currents ($I_{32}^+ \Delta t \sqrt{T}$ and $I_{39}^+ \Delta t \sqrt{T}$). Because of the complicated vaporization process a nominal 0.34 mm diameter effusion hole was employed in the

effusion cell to aid in obtaining equilibrium pressures. Temperatures were measured by thermocouple at the base of the effusion cell and confirmed by optical pyrometer sighting into the effusion cavity.

The sample used in the current measurements was prepared by a commercial supplier and had a molar ratio of K_2O/Fe_2O_3 of 1/7. This composition corresponds to a two phase region in the phase diagram at elevated O_2 pressure (see Figure 1) which is not stable under the conditions of the vacuum vaporization experiments. Thus, in the early stages of the measurements, oxygen pressures were high because of the reaction



which competed with the reaction,



Three sets of experiments were carried out using two samples of molar ratio K_2O/Fe_2O_3 of 1/7. In the first two experiments, the initial starting composition were taken as 1/7 and the final composition was taken as 1/6. In the third experiment the initial and final composition were both assumed to be 1/6. The three independent sets of calibration constants determined for O_2 and K were consistent using these assumptions.

In previous measurements on $KFeO_2$ [1], we noted that certain non-equilibrium effects were observed. Measurements of ion currents were made at constant temperature but the ratio of I_{32}^+/I_{39}^+ varied with time depending on whether the temperature was increased or decreased

in going from one constant temperature to another. When the temperature was increased, the K^+ intensity increased with time while the O_2^+ intensity decreased with time. If the temperature were decreased, then the K^+ intensity decreased with time and the O_2^+ intensity increased with time. Although it was possible to obtain and reproduce a steady state in which the K^+ and O_2^+ intensities did not depend on time, it was expedient to obtain data by varying the temperature in one direction only and accepting the K^+ and O_2^+ ion currents at the mean time interval of each temperature because this data is also required to calculate the mass spectrometer sensitivity constant. The gradual variation in K^+ and O_2^+ intensities with time at constant temperature is believed to result from a slight variation in composition of one or both of the phase boundaries.

In the measurements on $K_2O \cdot 6Fe_2O_3 - Fe_3O_4$ the same non-equilibrium effects as mentioned above were observed; however, the approach to steady state conditions was much slower than in the $KFeO_2 - K_2O \cdot 6Fe_2O_3$ measurements and it was not possible to demonstrate that equilibrium conditions could actually be achieved. The observation that the increase in the K^+ and the decrease in the O_2^+ signals with time can be reversed by decreasing the temperature so that the K^+ signal decreases and the O_2^+ signal increases is evidence that the composition of the evaporating phase has crossed the equilibrium phase boundary and is tending toward equilibrium.

As in the previous measurements, K^+ and O_2^+ signals were taken at the mean of the time interval of each constant temperature point. Since none of the data is obtained at equilibrium but the system is trending toward equilibrium it follows that the K pressures are too low and the oxygen pressures too high for data obtained when the temperature is increased while the K pressures are too high and the oxygen pressures too low for data obtained with decreasing temperature.

Some typical data for K and O_2 pressures are shown in Figure 7. The upper curve labeled A and the lower curve labeled A show the respective K and O_2 pressures when the temperature is varied from lower temperature to higher temperature while the curves labeled B show the K and O_2 pressures when the direction of temperature change is reversed. In spite of the non-reproducibility of the data, it is possible to show that the variation in the $K_2O.6Fe_2O_3$ composition is not very great. If the vaporization reaction is written to produce one mole of vapor and the $K_2O.6Fe_2O_3$ composition is essentially constant then the product $P_K^{0.57} \cdot P_{O_2}^{0.43}$ should vary linearly with $1/T$. Figure 8 shows the same data as shown in Figure 7 plotted in this way and it is clear that a linear plot is obtained. In fact, all of the data obtained in the measurements closely follow this curve.

As noted previously, the variation in the K^+ and O_2^+ intensities with time at constant temperature show that the composition of $K_2O.6Fe_2O_3$ varies somewhat with temperature. Although we assumed

that the average composition is $K_2O.6Fe_2O_3$, it is possible to calculate shifts in the O_2 content from the assumed average composition using the observed ion intensities. At a temperature of $1300^\circ C$ the composition of " $K_2O.6Fe_2O_3$ " turns out to be $K_2O.6Fe_2O_{2.97}$. Thus, the deviation in O_2 content from the assumed average composition is not large.

Finally, a comparison of K pressures over $KFeO_2$ - $K_2O.6Fe_2O_3$ and $K_2O.6Fe_2O_3$ - Fe_3O_4 is of interest. Although equilibrium pressures were not obtained a comparison of K pressures for phases of fixed composition may be made using the data obtained from $P_K^{.8} \cdot P_{O_2}^{.2}$ for the former and $P_K^{.57} \cdot P_{O_2}^{.43}$ for the latter. These comparisons assume that $P_{O_2} = 1/4 P_K$ for the $KFeO_2$ vaporization and $P_K = 1.33 P_{O_2}$ for $K_2O.6Fe_2O_3$. Average potassium pressures for the respective phases plotted as a function of temperature are shown in Figure 9. Pressures of K over $K_2O.6Fe_2O_3$ are approximately $1/2$ those over $KFeO_2$. The pressures at $1300^\circ C$ in the 10^{-4} atm range predict that loss of K would be experienced unless a high ambient pressure of O_2 was maintained or experiments were of short duration. This is entirely consistent with the findings in other parts of the study.

Conclusion and Discussion

Phase assemblages in the system $KFeO_2$ -" Fe_2O_3 " have been determined by the quenching technique in the 1200° - $1600^\circ C$ temperature range for compositions between 80 and 100 mole percent Fe_2O_3 . The existence of a β''' -alumina structure type between 1400° and $1520^\circ C$ at about a $K_2O:11Fe_2O_3$ composition is reported.

The corrosive attack of platinum by specimens in the 80-100 mole percent Fe_2O_3 range appears minimal at temperatures in the 1450°-1600°C range. However, the development of arrays of small pores in the platinum suggests diffusion of volatile species from the specimen into the tube and agglomeration into pores. The absence of container attack is attributed to the fact that the amount of Fe^{+2} in the specimens in a closed environment is too small to cause a serious reaction problem with platinum. It is known that, in silicate systems, the presence of Fe^{+2} does lead to container problems and bulk composition shifts (see e.g. Min. Mag. (12) 41, 555-6 (1977)). For this reason, it is planned to investigate the effect of SiO_2 additions to selected compositions in the $\text{KFeO}_2\text{-FeO}_x$ system and determine the extent of container reaction at low oxygen pressures.

Vapor pressure measurements on $\text{K}_2\text{O:6Fe}_2\text{O}_3$ (85.7 mole percent Fe_2O_3) show the potassium pressures to be about one-half those over KFeO_2 . However, pressures in the 10^{-4} atm range at 1300°C predict that loss of K would be expected unless a high ambient oxygen pressure was maintained to suppress volatility or experiments were of short duration. This is confirmed by the excessive outgassing of a specimen containing 87.5 mole percent Fe_2O_3 during a drop tube melting experiment performed by MSFC for NBS.

References

1. J. R. Manning and R. L. Parker, NBS: Properties of Electronic Materials, NBSIR 78-1483, pp. 84-100, June 1978.
2. T. Takahashi, K. Kuwabara and Y. Kase, "Formation of $K-\beta\text{Fe}_2\text{O}_3$ and Phase Diagram of the System $\text{KFeO}_2\text{-Fe}_2\text{O}_3$ ", Denki Kagaku 43 [5] 273-7 (1975). In Japanese.

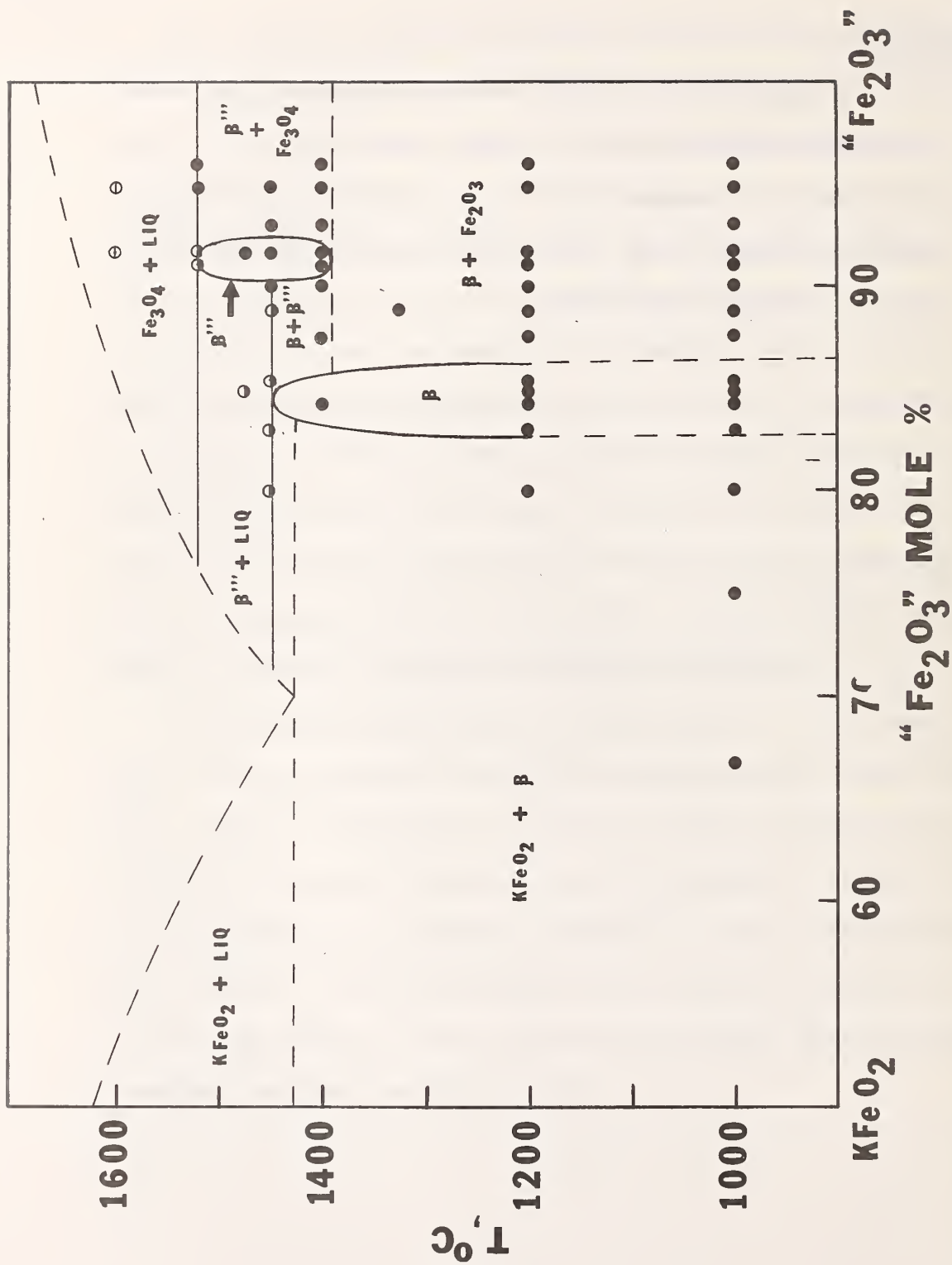
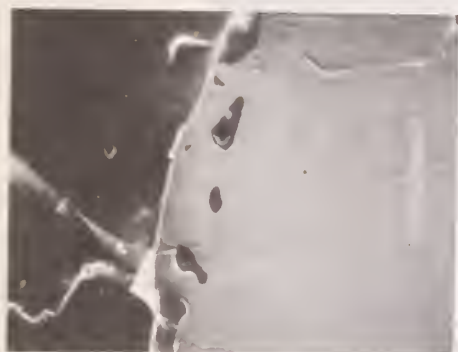
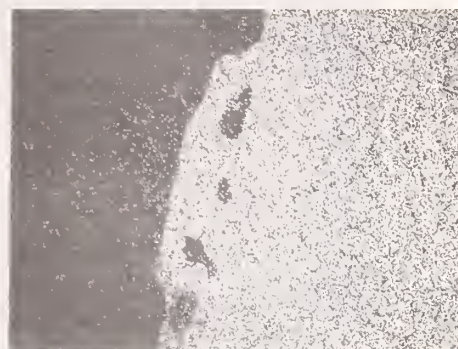


Figure 1. The system $\text{KFeO}_2 - \text{Fe}_2\text{O}_3$.



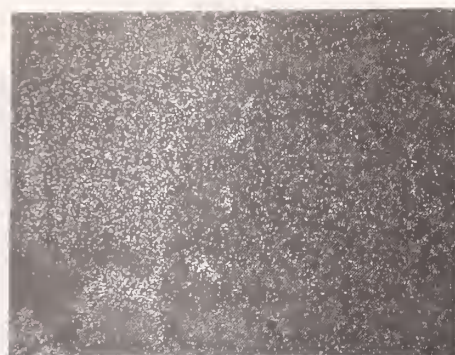
(a)



(b)



(c)



(d)

—|—|—|
0.05 mm

Figure 2. (a) Specimen and platinum container of $\text{K}_2\text{O}:4\text{Fe}_2\text{O}_3$ (80 mole percent Fe_2O_3) after heating at 1450°C for 20 hours.

(b) Platinum map of 2(a).

(c) Iron map of 2(a).

(d) Potassium map of 2(a).



3 μm

Figure 3. Platinum container used for heating specimen of $K_2O:4Fe_2O_3$ (80 mole percent Fe_2O_3) at $1450^\circ C$ for 20 hours.



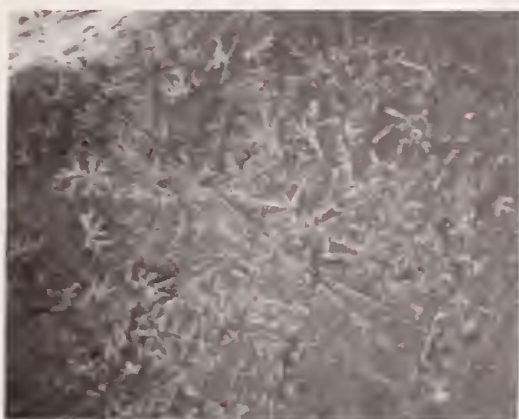
6 μm

Figure 4. Platinum container used for heating specimen of $K_2O:12Fe_2O_3$ (92.3 mole percent Fe_2O_3) at $1450^\circ C$ for 20 hours (dark area specimen, light area platinum).



6 μm

Figure 5. Platinum container wall used for heating specimen of $\text{K}_2\text{O}:16\text{Fe}_2\text{O}_3$ (94.1 mole percent Fe_2O_3) at 1450°C for 20 hours.



(a)

50 μm



(b)

10 μm

Figure 6. Platinum container used for heating specimen of $\text{K}_2\text{O}:11\text{Fe}_2\text{O}_3$ (83.3 mole percent Fe_2O_3) at 1475°C for 19 hours, left exposed to air after SEM examination.

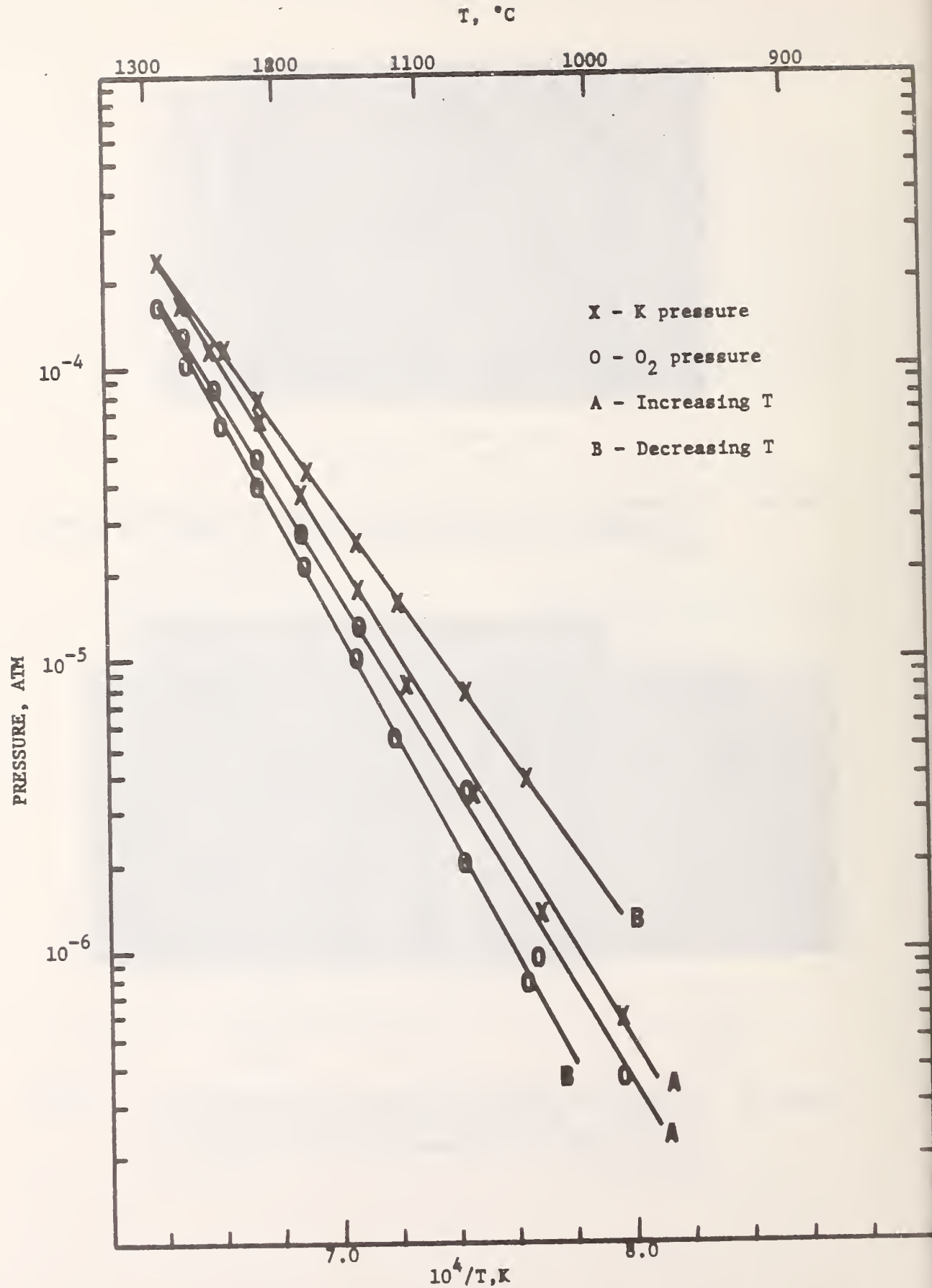


Figure 7. Plot of P_K and P_{O_2} over $K_2O \cdot 6Fe_2O_3 - Fe_3O_4$ showing dependence of pressure on direction of temperature change.

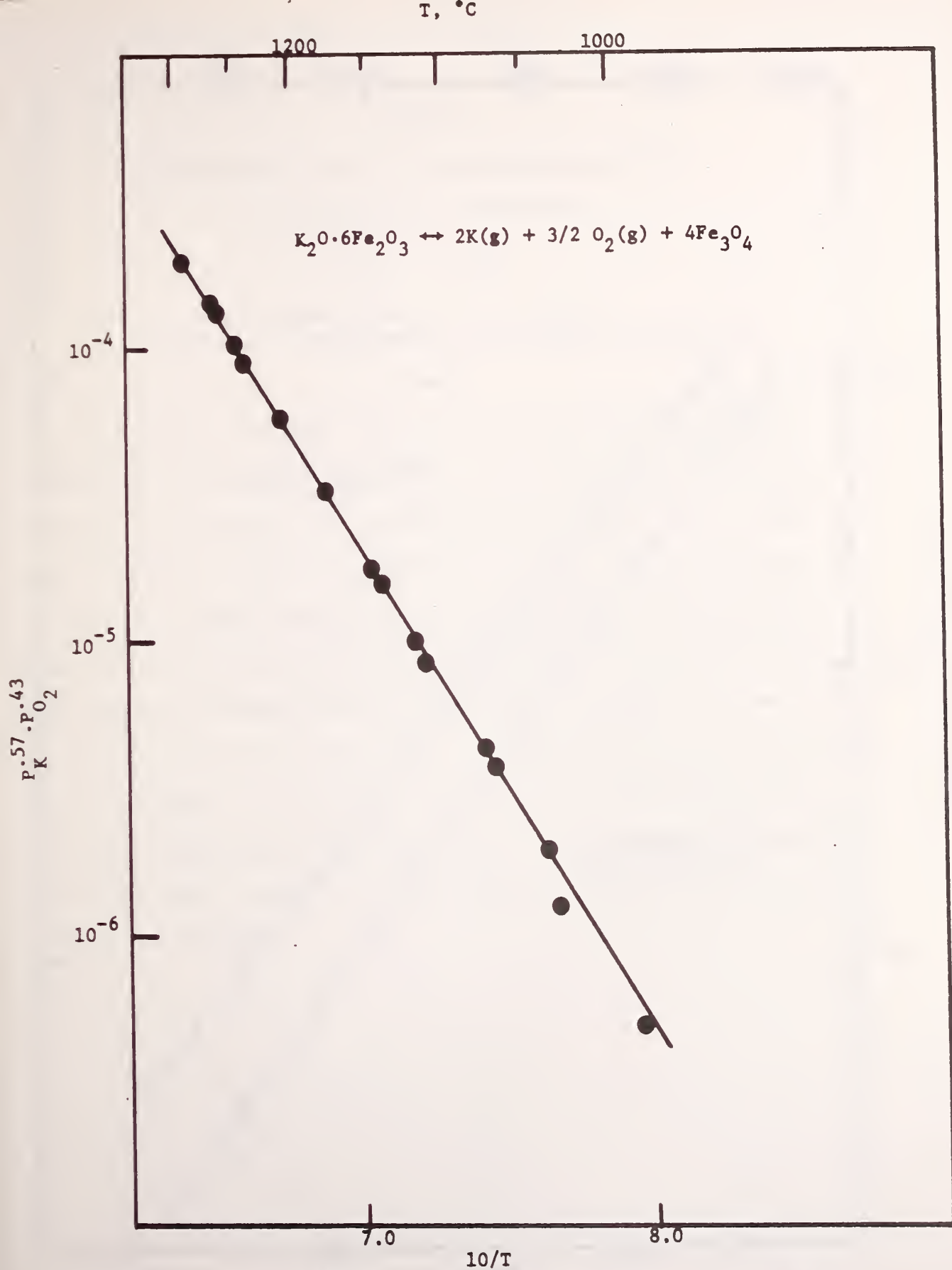


Figure 8. Plot of $P_K^{0.57} \cdot P_{O_2}^{0.43}$ of same data shown in Figure 7, demonstrating that composition range of $\text{K}_2\text{O} \cdot 6\text{Fe}_2\text{O}_3$ is small.

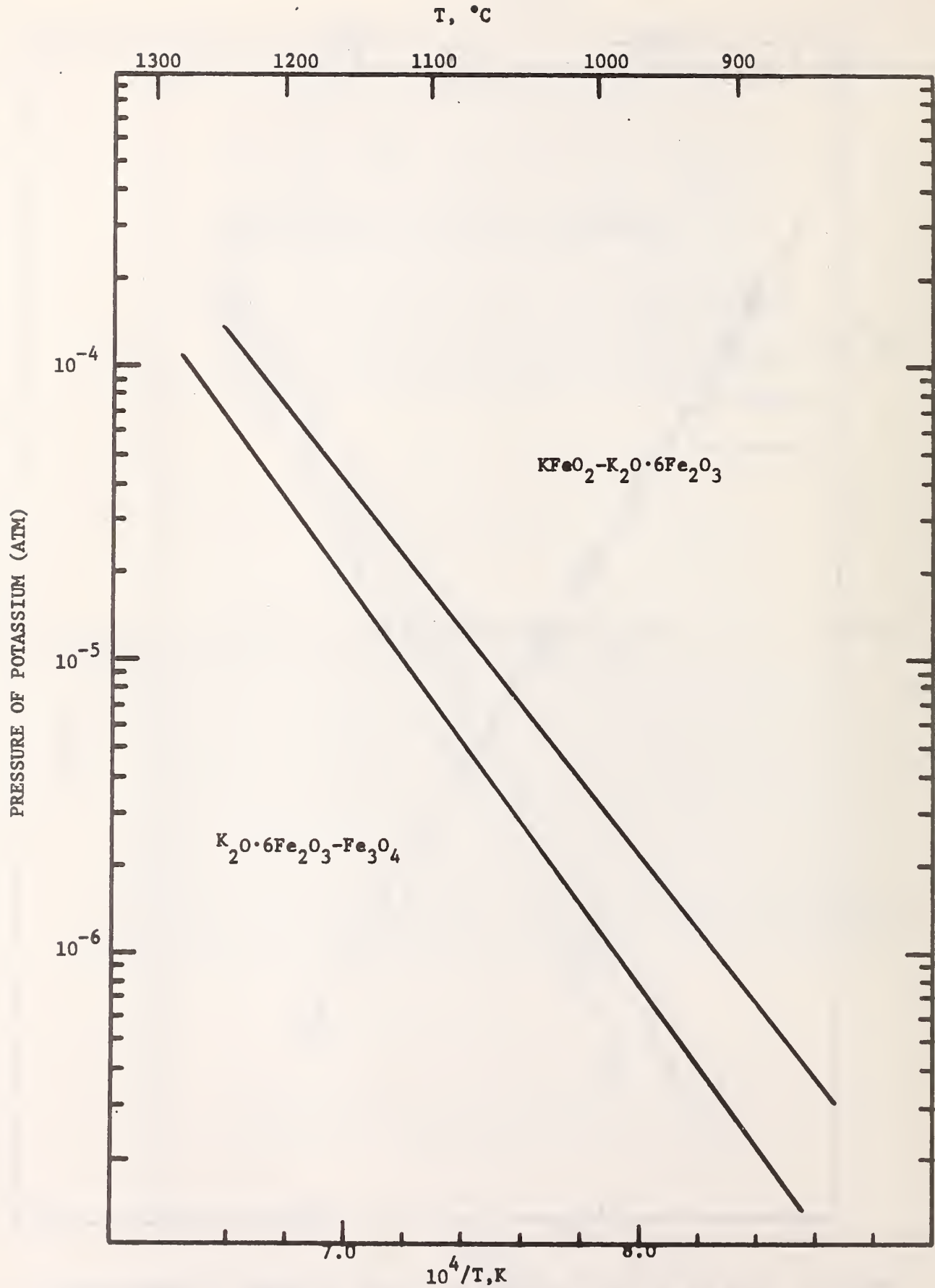


Figure 9. Comparison of K pressures over $KFeO_2-K_2O \cdot 6Fe_2O_3$ and $K_2O \cdot 6Fe_2O_3-Fe_3O_4$ for assumed constant compositions.

Task 4

Thermodynamic Properties of Refractory Inorganic Materials at High Temperatures

Jack H. Colwell

Chemical Thermodynamics Division
Center for Thermodynamics and Molecular Science

Summary

The various techniques that have been used for high-temperature thermodynamic measurements are reviewed, detailing the major problems involved. The potential for obtaining thermodynamic data from freely-cooling spherical samples is presented. The use of optical pyrometry and arrays of photodiode detectors for the measurement of surface radiance temperatures are contrasted and the requirements for converting these measurements to thermodynamic temperatures are discussed. The use of pyroelectric detectors is proposed for the determination of the total heat loss from samples. The measurement difficulties presented by several particular aspects of the experiments, such as the radiance of transparent materials, sample vaporization, and temperature gradients within spherical samples, are discussed.

Introduction

High temperature thermodynamic data has been largely derived from drop calorimetry measurements^[1]. In these measurements samples are heated to some fixed (known) temperature in a furnace and then "dropped" into a calorimeter. The heat released in the calorimeter is a measure of the enthalpy change of the sample between the temperatures of the furnace and the calorimeter. From a series of such determinations at different furnace temperatures, the heat capacity and other thermodynamic variables for the sample material can be derived. At moderate temperatures the sample temperature within the furnace is usually determined by measuring the furnace temperature with a resistance thermometer or thermocouple. At sufficiently high temperatures, optical pyrometers are used to measure the temperature of the sample within the furnace; this arrangement usually gives a reasonable approximation to a black-body radiation source. Many types of calorimeters have been used varying from the "block" type, where a temperature rise of the calorimeter is determined, to calorimeters where a phase change in a calorimetric material, such as the melting of ice in the Bunsen ice calorimeter, is determined.

In striving to carry this type of measurement to higher temperatures (>2000 K), material problems became a limitation. Furnace design becomes difficult but this can be circumvented by direct heating of samples by induction heating or radiation sources. Sample containment, however, remains as a stumbling block. As temperatures are increased, all materials become increasingly reactive so that the samples must be kept from any contact with foreign materials in order to prevent their reaction or

contamination. Several ways have been found around this problem. Samples have been suspended within the induction coils by fine wires of the same material as the sample, an approach which works up to the melting point^[2]. In these experiments a deep hole bored in the side of the sample served as a black-body cavity for temperature measurements.

The latest step in this line of development is the use of electromagnetic levitation to suspend the sample while it is heated^[3]. By properly shaping induction coils and applying sufficient power, an electromagnetic lift can be imparted to a sample so that it is levitated in the gravitational field. After the temperature of the sample reaches a steady state, the radiance temperature of the sample is determined and the levitating field is shut off, dropping the sample into a calorimeter. These experiments are difficult and tedious because the power required to levitate a sample frequently precluded effective temperature control of the sample. Coils have to be developed for individual cases dependent on the density and electrical resistance of the sample and the range of temperatures to be covered. These experiments, on the other hand, are not limited by the melting of the samples and measurements have been made well into the liquid range of several metals. It is necessary, however, to line the calorimeter with a sheath of the sample material to prevent reactions at that stage of the experiment.

A parallel development in the measurement of high-temperature heat capacities has been the use of high-speed resistive heating of metal samples, the entire experiment taking less than one second^[4]. The heat capacity is derived from the simultaneous measurement at millisecond intervals of the power being dissipated in the sample and its rate of

temperature rise. Temperatures are determined with a high-speed pyrometer by observing the black-body radiation within the tubular sample through a small hole in the wall of the tube. The experiments are nearly "containerless" even through the current and potential leads make contact with the sample. The current leads are remote from the measurement area and are cooled so there is little likelihood of impurity diffusion to the measurement area in the short duration of the experiments. The knife edges used for potential contacts are made from the same material as the sample so that no contamination can occur. Experiments can be carried to the point where the sample is partially molten, but the collapse of the sample prevents any extension of the measurement further into the liquid range^[5]. This technique, as with the use of electromagnetic levitation, has been limited to metals. Although "non-conductors" are usually sufficiently conductive at high temperatures to permit electrical heating, such experiments will be very difficult^[6]. The high speed experiments require that the sample be heated uniformly. This is assured in the case of metals where their electrical resistance has a positive temperature coefficient, as a result the coolest point in the cross section of the sample gets the most current and therefore, the most heating. The reverse is true of nominal insulators, the conductivity is semiconducting in nature so that the most heating will take place at any hot spot which accidentally occurs.

With the advent of the Space Shuttle Program the possibility was presented of conducting containerless, high temperature thermodynamic measurements on materials that are not good metallic conductors. An

obvious approach would be an experiment similar to the electromagnetic levitation experiment except that the low-gravity environment of space would be used to "suspend" the sample as it is heated and its temperature determined. Since the sample cannot be dropped, it would be necessary to inject it into the calorimeter in some way or for the calorimeter to engulf the sample. The latter prospect led John Margrave to dub such a device the "gulp calorimeter"^[7,8]. Although this approach to the problem is straightforward and involves no new principles, it would be cumbersome in practice. Each datum of the enthalpy determinations would probably require a separate sample and a new calorimeter liner or possibly even a different calorimeter. Even if the device could be automated the experiments would still be very time consuming and most likely still require considerable operator participation. An alternative method which we have been studying is to simply heat a sample to a high temperature and then allow it to freely cool within an evacuated cold-walled chamber. If the rate of energy loss and the temperature of the sample can be determined as a function of time one has a direct measure of the heat capacity as simply the rate of energy loss divided by the rate of temperature change. It is the problems likely to be encountered in making these two measurements on which we have concentrated our attention. There are other aspects of such an experiment for which we have postponed consideration or which are being pursued by other workers. Positioning of the sample within the apparatus and making it hold that position is one such case. In the space environment an apparatus will be subjected to accelerations which a freely

floating sample within the apparatus would not experience. To keep the sample in a fixed position within the apparatus the same accelerations must be imparted to the sample. Electromagnetic positioning is anticipated for this purpose (see below). Sets of coils, similar to those used for the ground-based levitation of metals, can be used, but operating at very low power so that little energy is dissipated to the sample. Thomas Frost has been studying the application of this technique to the space environment^[7]. An alternative is to use acoustic positioning^[9], but as this technique requires a gas atmosphere, we are not giving it much consideration at this time.

Heating of the sample to a high temperature after it is positioned in the apparatus can be carried out in a variety of ways and should not present a major difficulty. If electromagnetic positioning is utilized, the same coils could be used for inductively heating the sample. It is likely, however, that the positioning coil would not be strongly coupled with the sample so that the inductive heating would have to be supplemented with some form of radiative heating to achieve the highest temperatures. Nonmetallic samples will have to be heated radiatively to some high temperature (~ 2000 K) before they will be sufficiently conductive even to be positioned electromagnetically, so it is unlikely that inductive heating can be utilized in this case.

Temperature Measurement

No matter what type of experiment we are going to perform to determine the thermodynamic properties of a sample, we must determine the temperature of the sample. For the temperatures we are considering

—greater than 2000 K, in a vacuum environment, —radiation thermometry is the only means available. The radiance of a black body is given by Planck's distribution law

$$J_b(\lambda, T) = C_1 \lambda^{-5} \pi^{-1} [\exp(C_2 / \lambda T) - 1]^{-1} \quad (1)$$

where C_1 and C_2 are the radiation constants and λ is the wavelength of the radiation^[10]. Temperatures are not determined by measuring J_b in an absolute sense but by measuring J_b relative to that of another source. The International Practical Temperature Scale is derived by assigning a numerical value to the temperature of a black body at the melting point of gold. In designing high temperature experiments one usually tries to achieve a black body source in some way —a cavity in the specimen can give a good approximation. In experiments where the sample is unconfined, this is not easily accomplished and is not possible for molten samples. One must then resort to measuring the surface radiance which is given by

$$J(\lambda, T, \theta) = \epsilon(\lambda, T, \theta) J_b(\lambda, T) \quad (2)$$

where $\epsilon(\lambda, T, \theta)$ is the spectral emittance of the sample surface. The emittance is a function of the condition of the surface, the angle of the emission, θ , relative to the normal to the surface, and has a temperature and wavelength dependence which is characteristic of the material. By integrating over all angles one obtains the hemispherical spectral radiance

$$W(\lambda, T) = \epsilon(\lambda, T) W_b(\lambda, T) = \epsilon(\lambda, T) \pi J_b(\lambda, T) \quad (3)$$

where $\epsilon(\lambda, T)$ is the hemispherical spectral emittance. Further, integrating over all wavelengths gives one the total hemispherical radiance

$$W(T) = \epsilon(T) W_b(T) = \epsilon(T) \sigma T^4 \quad (4)$$

where $\epsilon(T)$ is the total hemispherical emittance and σ is the Stefan-Boltzmann constant. The latter equation defines the total radiative heat loss per unit surface area as a function of temperature.

There is an extremely large literature on the radiative properties of materials but the subject is not well understood. Emittance measurements are not easy to make, particular for wide ranges of angle, temperature, and wavelength. The sensitivity to surface condition makes the use of literature values questionable (emissivity is the emittance of an optically flat surface which should also be clean and free of damage), and, in any case, at high temperatures few values exist. It appears, however, that whatever technique is used to determine temperature, it will be based on some assumption about the emittance of the sample so one must be cognizant of the literature on the subject. In the electromagnetic levitation experiments of Margrave and coworkers^[11] the emittance of the molten sample was determined at the melting point, a temperature that was known, and it was assumed that it did not change with increasing temperature. The assumption, in this case, although an expedient, is based on the knowledge that for metals, the emittance is not a strong function of temperature or wavelength.

The assumption of the emittance being a weak function of temperature and wavelength is also the basis of the only practical method available for skirting the problem of an unknown emittance. The typical optical pyrometer is monochromatic, using filters to define a narrow band of wavelengths usually centered at 0.653 μm . The temperature is then defined by (using Wien's Law as an approximation for Planck's Law)

$$J(\lambda, T) = \epsilon(\lambda, T) C_1 \lambda^{-5} \pi^{-1} \exp(-C_2/\lambda T). \quad (5)$$

By using a two color pyrometer where the radiance is determined simultaneously at two different frequencies, one obtains

$$\frac{J_1}{J_2} = \frac{\epsilon_1}{\epsilon_2} \frac{\lambda_2^5}{\lambda_1^5} \exp(C_2/T) [(1/\lambda_2) - (1/\lambda_1)] \quad (6)$$

If one assumes the emittances are equal then the ratio of the radiances gives the temperature; or better, if the radiances can be determined at a known temperature, such as a melting point, then one need only assume that the ratio of the emittances is a constant to obtain any other temperature. An idea of the validity of these assumptions can be obtained from Fig. 1 which shows the extensive emissivity data for tungsten obtained by de Vos^[12]. The assumptions that the emittances are either independent of temperature or equal at two different wavelengths can be seen to fail badly. The assumption that the ratio of emittances is independent of temperature is rather good at short wavelengths but begins to break down above 1 μm . If one goes to a three color pyrometer one can assume that the slope of the ϵ versus λ curve is constant or, with a point of calibration, that the curvature is constant. The three-color device is probably more useful being used as two separate two-color devices where the redundancy is likely to show up systematic errors, from the failure of the basic assumptions or from instrumentation faults.

The instrumentation of optical pyrometry has undergone some recent development^[6,13] and, in general, these devices far exceed our demands.

Automatic pyrometers have been constructed which can record data at microsecond intervals. The highly stable silicon photodiodes are replacing photomultipliers as detectors so that continuous chopping for intercomparison with a reference standard is no longer necessary and a continuous output can be used. Fiber optics can be used to carry light to a remote detector system if required^[6].

The use of pyrometers in our experiment could cause some difficulties because we would be viewing a sphere, possibly of small size, that is not rigidly positioned and will be moving about to some degree. An optical pyrometer is usually used to view the normal spectral radiance from a surface, but in viewing a sphere this would only be achieved at the midpoint of the spherical image. If the sphere behaved as a gray body, i.e. had a constant emittance, independent of angle as well as wavelength and temperature, it would not matter what part of the sample surface was viewed for the sphere would appear as a flat disc of uniform radiance. A real sphere, however, will not be gray and the emittance will have a pronounced angular dependence. The general behavior found for this dependence is shown in Fig. 2 where the emissivity relative to the normal emissivity is plotted as a function of angle. This angular dependence is in addition to the Lambert cosine law correction for projected area. The important point is that all opaque materials do appear to have an extended region going out to between 30 and 45° from the normal to the surface where the emittance is constant. Thus, in observing a sphere with a fixed pyrometer, the sphere could undergo lateral displacements of approximately half the radius of the sphere

without affecting the observation as long as the field of view is small compared with the radius of the sphere. Similar displacements parallel to the viewing direction, causing the sample surface to be out of focus, can probably also be tolerated.

The possibility of having to cope with relatively large sample displacements led us to consider using an array of radiation detectors in place of an optical pyrometer. The individual detectors could be of the silicon diode type with lenses or apertures to define a field of view much larger than the sample at the position of the sample. The signal of the detector will depend, in addition to the radiance of the sample, on the size of the sample and its distance from the detector. To establish the position of the sample at a given instant an array of detectors would be used. With an appropriate geometric array the magnitude of the instantaneous signals at the detectors would vary as the inverse square of the distance of the sample from each detector. This information can be used to establish the position of the sample and then the signal at any one detector can then be related to the sample radiance. The arrangement which appears best for this purpose is to have four detectors at the apices of a regular tetrahedron. This arrangement allows for two sets of detectors to be symmetrically placed about a sample by having them occupy alternate corners of a cube as diagrammed in Fig. 3. This arrangement also allows for three sets of mutually perpendicular positioning coils to occupy the faces of the cube. The size of the sample would have to be determined, probably by photographic techniques. The bandwidth at the individual detectors would be determined by the characteristics of the detectors and any filters that may be used, just as with a pyrometric system.

The detector array could be adapted to two-color determinations. The best arrangement for this would probably be to use two separate detector systems but it could be done by switching filters on a single array.

In order to get the most accuracy in the temperature measurements it will probably be necessary to obtain information on the emittances of the various materials being studied by conducting separate laboratory experiments. For materials in the solid state, one could construct samples with cavities to get a black-body temperature while simultaneously measuring the surface emittance. For liquid state measurements, skull melting^[14] could be used to achieve uncontaminated samples. Although the temperature of the melt could not be obtained with any accuracy, the radiance as a function of wavelength at various arbitrary temperatures would be useful in identifying unexpected large fluctuations in emittances.

In resorting to separate emittance measurements, use of optical pyrometric measurements will be much simpler than using the silicon detector system both from an instrumental standpoint and because of the quantity that must be measured. The optical pyrometer as used measures the normal spectral radiance as given by Eq. 2 ($\theta = 0^\circ$). The detector system, however, in looking at a sphere will be observing a radiance which is equivalent to the hemispherical spectral radiance given by Eq. 3. This can be seen in Fig. 4 where the top portion is a pictorial description of the hemispherical radiance, i.e. all the radiation leaving the elemental flat surface at all angles falls on a hemispherical detector. The bottom portion of Fig. 4 shows the radiation from a sphere falling on an elemental detector surface at a distance. It can be shown

analytically that the radiance as a function of emission angle reaching the detector is the same in each case, but a symmetry argument will suffice. If the elemental detector in the bottom picture is considered as a portion of a larger sphere symmetrically enclosing the radiating sphere, then all the radiation leaving the inner sphere must fall uniformly on the outer sphere. Since each elemental surface area of the inner sphere is radiating as the elemental area in the top picture the elemental detector in the lower picture must be receiving the hemispherical radiance. As a result, if we were to try to determine the required emittances in separate experiments, the detector system would require that we observe a sphere with one of the detectors in the same fashion as it is to be used in the actual experiment, or measure a flat radiating surface at all angles to the normal and integrating over a hemisphere. In either case the task would be difficult compared to a simple measurement of the normal radiance.

Most of the above discussion concerning emittances is based on the premise that the radiating samples are opaque. Since our primary interest is in dielectric materials we will surely be encountering materials that are transparent in at least some wavelength regions. There is very little information available on the thermal radiation from bulk samples of transparent materials. The most useful discussion we have found is by Gardon^[15] who analyzed the radiation from ordinary glass. The principle point is that the emission of radiation is no longer a surface phenomenon but a bulk phenomenon. As a result, the thickness of the sample and absorption coefficient of the material become determining parameters.

Figure 5 summarizes some of the results of Gardon. It is the product of the absorption coefficient, γ , and the sample thickness, X , which determine the effective thickness of a sample, for if the absorption coefficient is large the material will appear opaque and all the radiation will be from the surface layer. This thickness dependence is going to have a pronounced effect on what one observes with spherical samples; the size of the observation area of constant emittance will now be much smaller than was determined above for opaque materials.

Free-Cooling Experiment

To gather thermodynamic information from a free-cooling experiment one must be able to measure, in addition to temperature, the total heat loss from the sample. In our case, we are considering a spherical sample at temperatures in the range 2000 to 4000 K. At these temperatures the principal mode of heat loss will be by radiation. Heat loss through evaporation will be a consideration, but if it becomes large it will probably defeat the experiment for other reasons. For the range of temperatures considered, more than 99% of the thermal radiation will be in the band of wavelengths from 0.4 μm to 12 μm , i.e. from the far blue region of the visible through most of the near infrared.

In recent years there has been considerable research and commercial development in pyroelectric detectors. A pyroelectric is a poled ferroelectric material which, when heated, changes its spontaneous polarization and with suitably applied electrodes can be used to generate a current in an external circuit. The current is proportional to the rate

of change of temperature, so, to observe a continuous source, the radiation must be chopped in some way. Pyroelectric materials range from the plastic film of polyvinyl fluoride, to the organic crystals of triglycine sulfate, to the inorganic crystals of LiTaO_3 . LiTaO_3 with its high Curie temperature of 883 K is best suited for a high temperature apparatus and is used in many commercial devices. Since the pyroelectrics are thermal sensing devices, their response to different wavelengths is not a function of the pyroelectric material but of the surface coatings or the device configuration. Devices using gold-black coatings are effectively black over the spectral range of interest^[16] and the devices can be made less dependent on the quality of the coating by incorporating the pyroelectrics into wedge shaped light traps^[17]. The sensitivity of commercial detectors appear to exceed our demands but the linearity is questionable.

Pyroelectric detectors could be used in a manner similar to that proposed above for the use of silicon diode detectors in temperature measurements, except that radiation choppers would have to be installed in front of the detectors. In using these detectors the sample size and the distance from the sample to the detector would have to be determined. A detailed knowledge of the effective area of the detector would be needed to derive the total hemispherical radiance at the sample surface, but this would come out of the calibration procedures.

It is contemplated that the detectors would be exposed directly to the radiation from the sample with only apertures to cut down reflected radiation. If any evaporation is occurring, the detectors would also be exposed to the evaporated atoms which would most likely condense out. Assuming the vacuum is good enough for most of the evaporated atoms to travel directly to the surface of the detector and that their sticking coefficient is high, one could get a reasonable measure of the heat loss from evaporation. There is obviously much room for error on this point, for instance, the vapor could react with the detector coating. The coating itself, because of its highly porous nature, would probably have to adsorb a considerable amount of the evaporated species before its radiation absorption characteristics would be appreciably affected^[18]; also a light trapping device could help in this regard. One could use windows such as KRS-5 (thallous halides) or Irtran-2 (ZnS) which are transparent over the wavelengths concerned to discriminate against evaporated atoms but the reflection characteristics of these polished surfaces would be quickly affected by the condensation of the evaporated atoms. The various possibilities in this regard would have to be studied in separate laboratory experiments for each substance studied.

Margrave and Weingarten^[8] proposed, in the study of metals, that the induction coils be used to heat the sample to a steady state temperature. At that point the power loss from the sample by all mechanisms would be equal to power dissipated by the inductive heating. The latter can be calculated if the metal's resistance is known, but whether it could be calculated for a semiconducting material where the heating would not be uniform is uncertain.

In conducting a free-cooling experiment one would want to remove the heat source quickly so that initial perturbations can die away and the measurements begun before the sample has cooled appreciably from its highest temperature. This is done simply when radiant heating is being used by shutting off the source. If the sample is being heated inductively by the electromagnetic positioning coils, care must be exercised in reducing the field so that the sample does not go into wide oscillation about its equilibrium position. In rocket experiments where metallic samples were heated and positioned in this way it was found that the field could usually be reduced to a low level in a few couple seconds^[19].

A potentially major problem in the free cooling experiments is the temperature gradients that may exist in the sample. Since all the heat must leave from the surface of the sample, heat in the interior of the sample must be conducted to the surface and if the thermal conductivity of the material is small or the heat capacity or sample size is large, large temperature gradients will develop. For most metals the gradients would be small and not greatly affect a heat capacity determination, but for non-metals the problem could become severe and the solution intractable.

The rate of cooling of a sphere by radiation when no gradient exists is obtained by equating the rate of heat loss

$$dH = -4\pi R^2 \epsilon \sigma T^4 dt \quad (7)$$

with the thermal capacity

$$dH = (4/3)\pi R^3 c_p dT \quad (8)$$

which yields

$$dT/dt = -3 \epsilon \sigma T^4 / (c \rho R), \quad (9)$$

c is the specific heat and ρ is the density of the material, ϵ is the total hemispherical emittance and R the radius of the sphere. When the thermal conductivity, k , is finite the temperature distribution within an opaque sphere must satisfy the equation

$$\frac{\partial^2 T}{\partial r^2} + \frac{2}{r} \frac{\partial T}{\partial r} = \frac{\rho c}{k} \frac{\partial T}{\partial t} \quad (10)$$

where r is the radius vector. The solution must also satisfy the boundary condition at the surface

$$k \frac{\partial T}{\partial r} = \epsilon \sigma T^4 \quad \text{at } r = R \quad (11)$$

i.e. the energy leaving the surface must equal the energy conducted to the surface from the interior of the sphere. The T^4 term on the right hand side of Eq. (11) makes the problem nonlinear and it cannot be solved analytically. If the boundary condition is made linear in temperature

$$k \frac{\partial T}{\partial r} = hT \quad (12)$$

the problem can be solved (though not simply)^[20]. Approximate solutions can be generated by an iterative procedure of substituting

$$h = \epsilon \sigma T_0^3 \quad (13)$$

in Eq. 12, with T_0 as the starting surface temperature. After generating a solution for a small temperature change from an initial T_0 , a second determination is made starting from the previous final temperature. Each time, however, new roots to a transcendental equation must be found and the starting conditions generated by a Fourier's series involving those roots fit to the preceeding solution; a most laborious procedure. This problem was worked out several years ago by D. L. Ayers

using a finite-difference computing technique and a brief summary of the results was published^[21]. The generalized solutions are in terms of two dimensionless quantities

$$N_{Fo} = kt/(c\rho R^2) \quad (14)$$

and

$$N_{rc} = k/(\epsilon\sigma T_0^3 R) \quad (15)$$

When N_{Fo} exceeds 10 or N_{rc} exceeds 30 the cooling proceeds in a isothermal manner, that is, as given by Eq. 9. If one could obtain sufficiently accurate data there would be the possibility, for a region where the thermal gradients were moderately large, of deriving a value for the thermal conductivity as well as the heat capacity. This could be accomplished by varying the size of the sample for this has a marked effect on the cooling pattern; doubling the size of the sample would have the same effect as simultaneously doubling the heat capacity and halving the thermal conductivity. By measuring small samples the gradients would be small and the heat capacity could be found. That value could then be used in measurements on a large sample with its large gradients to get a value of the thermal conductivity.

The nature of the temperature gradient within a spherical sample using the boundary condition of Eq. 12 is shown in Fig. 6, where the temperature T as a function of the radial vector r is plotted relative to the temperature at the center, $r = 0$. The surface temperature will be at some point $R = \omega r$ where ω is a scaling factor which depends on the parameters affecting the temperature gradient. For example, if k is

large, ωr would approach zero and the gradient would be small; if k approached zero, ωr would approach π and the surface temperature would approach zero (we assumed the radiating sphere sees surroundings at 0 K). The dashed curve is an estimate of the behavior that would be obtained using the true radiation boundary condition of Eq. 11.

The behavior of transparent materials in free cooling experiments will probably be radically different from that described for opaque materials. The radiation from a transparent material does not originate at the surface but from within, so the description for thermal gradients given above cannot hold. When the path length for radiation within a material is very long it probably has the effect of making the effective thermal conductivity large.

Conclusions and Discussion

At this time the potential of free-cooling experiments for obtaining high-temperature thermodynamic data looks promising, but there are many aspects of such experiments that will require considerably more study as well as extensive laboratory investigation. The success of the free-cooling approach, as presently conceived, hinges on the ability to measure the total energy loss from the samples. We propose using pyroelectric detectors to measure the radiant energy loss, but their suitability for this purpose has yet to be established in laboratory tests.

It is intended that measurements will extend to temperatures where samples will be evaporating at a considerable rate. The heat loss from

evaporation can probably be established, but the sample vaporization will complicate the radiation determination. Tests should be made on rapidly evaporating samples to determine the effects on both radiation loss and temperature measurements, but a suitable experimental arrangement has not yet been devised.

For temperature determinations it will be highly desirable if an optical pyrometer type device can be used for radiance measurements. The methods for this type of measurement using multi-color rapid-response instruments are reasonably well established and the emittance parameters for the different materials would be much easier to assess than would be the case with the use of a detector array. At this time we do not see how a pyrometer can be kept focused on a sample if the sample is moving about to any extent. Electromagnetic positioning does not appear to be a problem for metals but may be for poor conductors. Before any development can begin, therefore, we must ascertain that samples of the materials of interest can be positioned within required limits. Other NASA contractors could be of assistance to us in this regard.

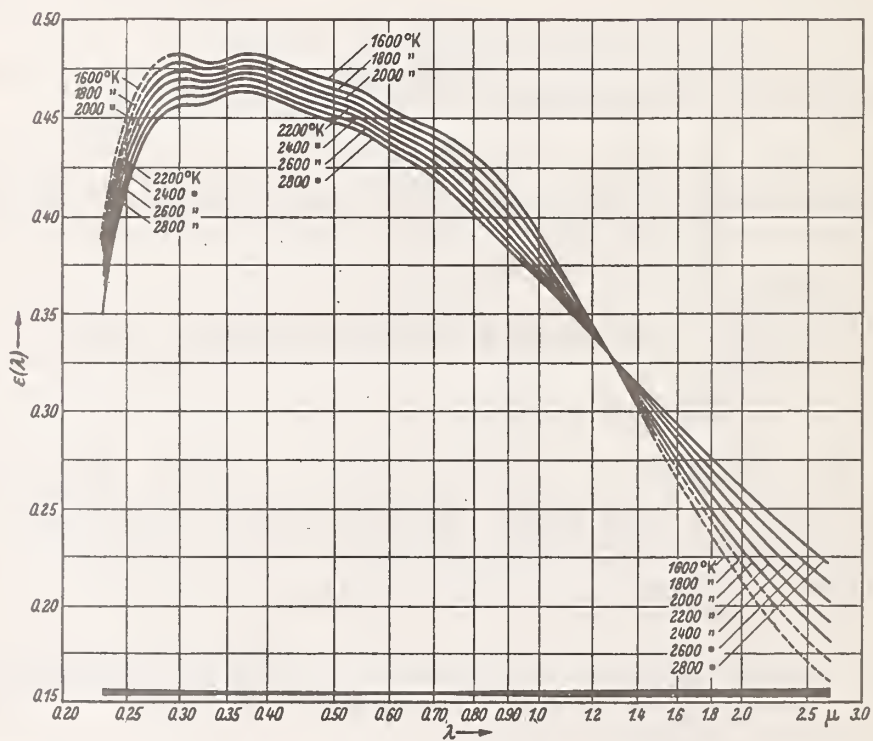
In the event that the free-cooling experiments are not feasible, we are continuing to give consideration to the various ways that receiver (drop) type calorimeter experiments can be conducted.

References

- [1] T. B. Douglas and E. G. King, Experimental Thermodynamics Vol. 1, J. P. McCollough and D. W. Scott, Eds. (Butterworth, London, 1968) p. 293.
- [2] L. Leibowitz, M. G. Chasanov, and L. W. Mishler, Trans. Metall. Soc. AIME 245, 981 (1969).
- [3] A. K. Chandhuri, D. W. Bonnell, A. L. Ford, and J. L. Margrave, High Temp. Sci. 2, 203 (1970).
- [4] A. Cezairliyan, J. Res. Nat. Bur. Stand. (U.S.) 75C (Eng. and Instr.), 7 (1971).
- [5] An evolution of this high speed technique which is under development is to carry out the measurements at much higher speed (microsecond intervals between readings) so that the integrity of the sample is maintained upon melting. See G. R. Gathers, J. W. Shaner and R. L. Brier, Rev. Sci. Instrum. 47, 471 (1976) or A. Cezairliyan and C. W. Beckett, Microsecond-Resolution Pulse Calorimetry for Semiconducting Materials at High Temperatures (A Feasibility Study), NBS Publication NBSIR 75-793, October 1975.
- [6] A. Cezairliyan, Thermophysics Division, NBS, Washington, DC, private communication.
- [7] Workshop on an Electromagnetic Positioning System in Space, May 1-2, 1978, Washington, D.C.
- [8] J. L. Margrave and J. S. Weingarten, Thermodynamics Property Determination in Low Gravity, Rice University, Contract NAS8-32030, Final Report, January 31, 1977.
- [9] W. A. Oran, D. A. Reiss, L. H. Berge, and H. W. Parker, Preliminary Characterization of a One-Axis Acoustic System, NASA TM-78213.

- [10] See for example D. L. McElroy and W. Fulkerson, Techniques of Materials Preparation and Handling, Vol. 1, pt. 1, Chap. II, R. F. Bunshah, Ed., Wiley and Sons, New York, 1968.
- [11] D. W. Bonnell, J. A. Treverton, A. J. Valerga, and J. L. Margrave, Temperature, Its Measurement and Control in Science and Industry, Vol. 4, pt. 1, p. 483, H. H. Plumb, Ed., Instr. Soc. of America, 1972.
- [12] J. C. de Vos, Thesis, Amsterdam, 1953.
- [13] See also the references in footnote [5].
- [14] In skull melting a block of material is heated locally to melting in such a way that the unmelted portion forms a crucible for the molten portions.
- [15] R. Gardon, J. Am. Ceram. Soc. 39, 278 (1956); 44, 305 (1961).
- [16] W. R. Blevin and J. Geist, Appl. Optics 13, 1171, 2212 (1974).
- [17] W. M. Doyle, B. C. McIntosh and R. L. Maxwell, Detectors for Wavelength Independent Radiometry, Electro-Optics/Laser meeting, Paper IX-2, New York, N.Y. (1976).
- [18] J. Geist, Radiometric Physics Division, NBS, Washington, D.C., private communication.
- [19] R. T. Frost, Space Science Center, General Electric Corporation, King of Prussia, Pa., private communication.
- [20] L. R. Ingersoll, O. J. Zobel, and A. C. Ingersoll, Heat Conduction, Univ. of Wisconsin Press, 1954.
- [21] D. L. Ayers, J. Heat. Trans., Trans ASME 92, 180 (1970). Unfortunately, these solutions may now be lost. We have made considerable effort to locate the author of this paper or someone familiar with the work, but we have not been successful.

Fig. 1. Emissivity of tungsten as a function of temperature and wavelength after de Vos [12].



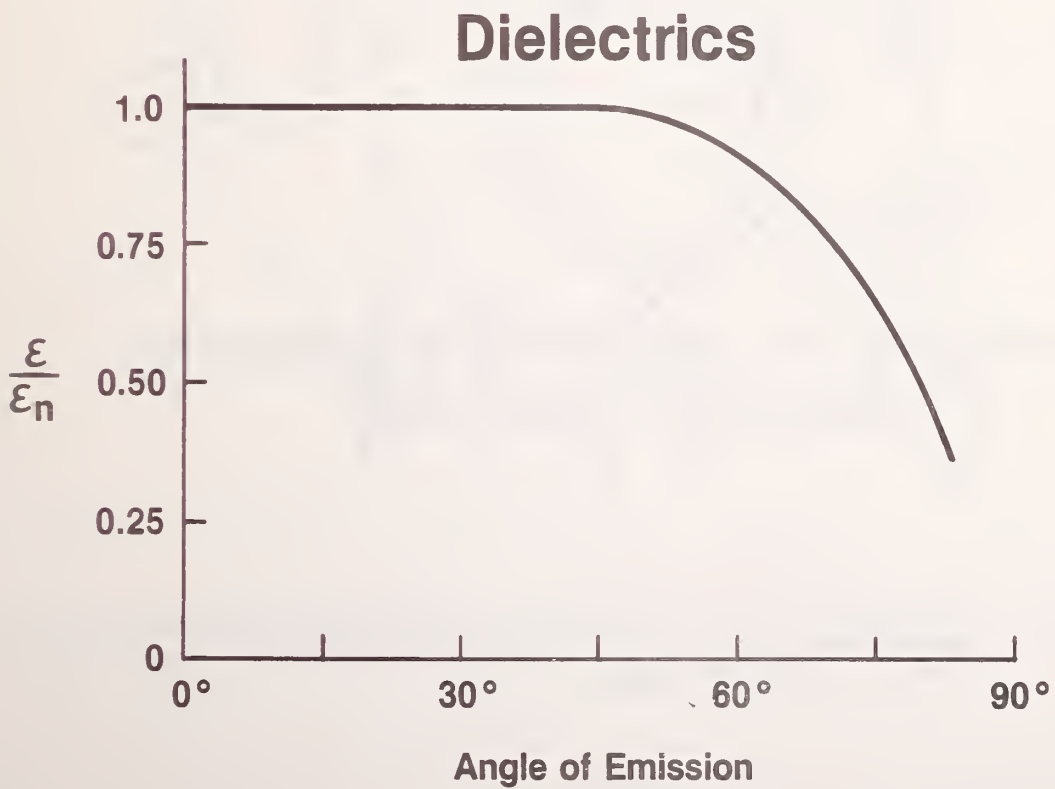
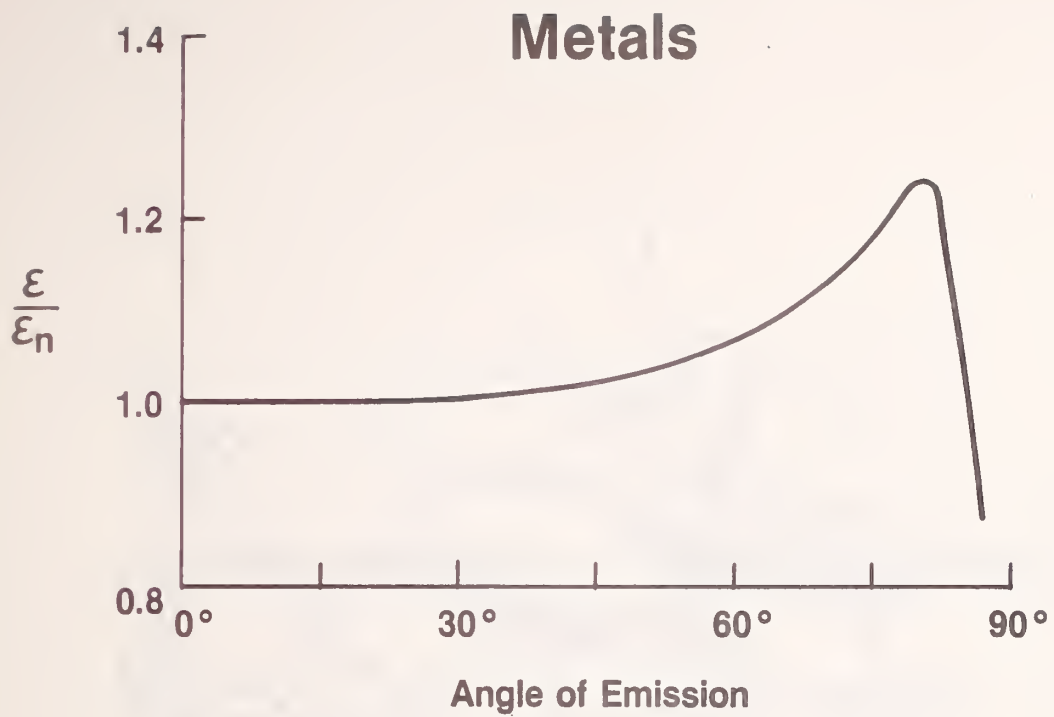


Fig. 2. Directional spectral emittance relative to normal emittance typical of metals and dielectric materials.

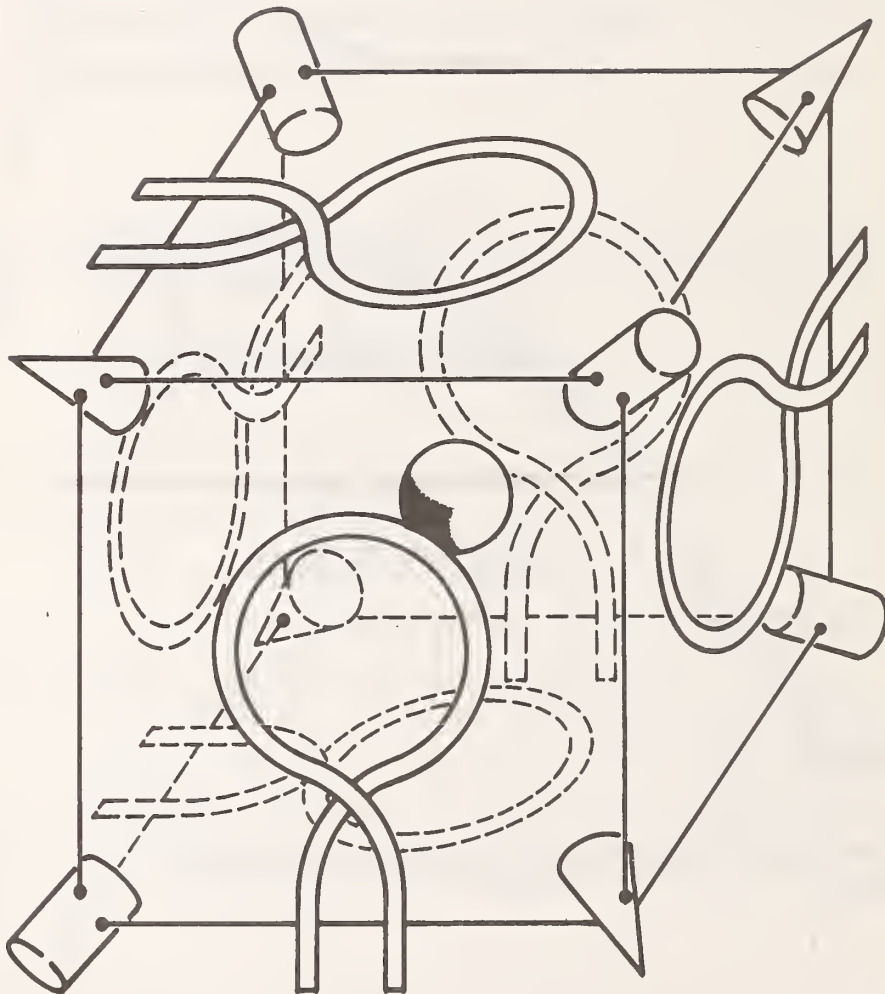
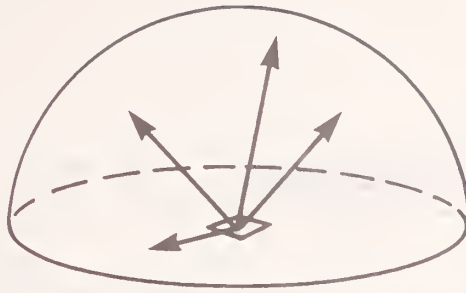
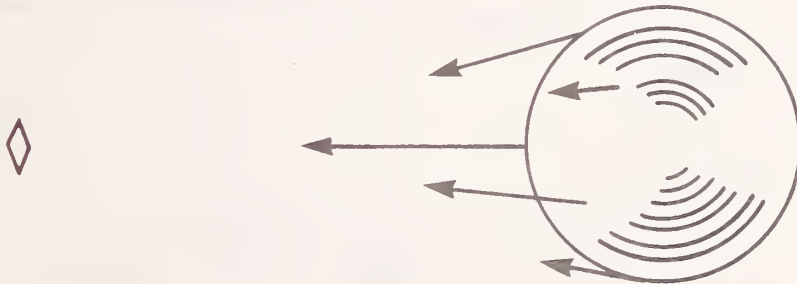


Fig. 3. Arrangement (not to scale) for positioning photodiode detectors pyroelectric detectors, and electromagnetic positioning coils about a spherical sample.



Measurement of Hemispherical Emittance



Measuring Emittance of a Sphere at a Point Detector

Fig. 4. Equivalence of detected hemispherical radiation.

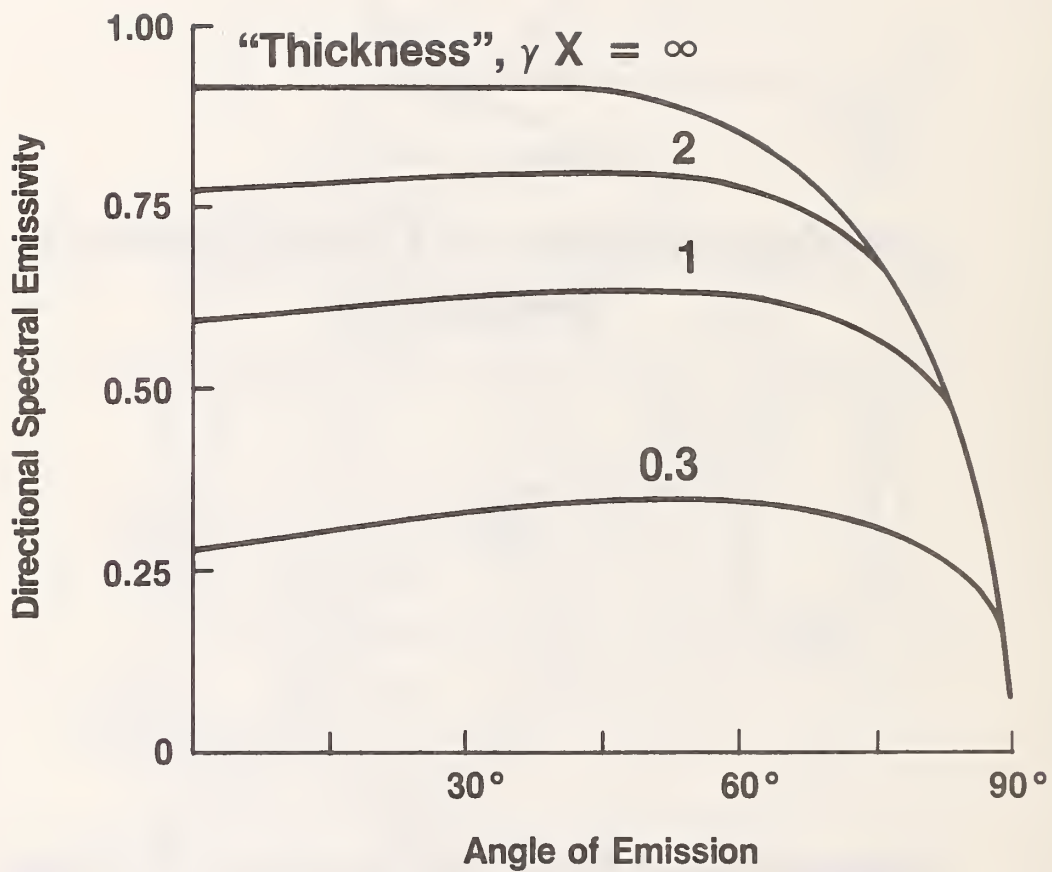


Fig. 5. Directional spectral emissivity of glass determined by the product of the absorption coefficient, γ , and the sample thickness, X .

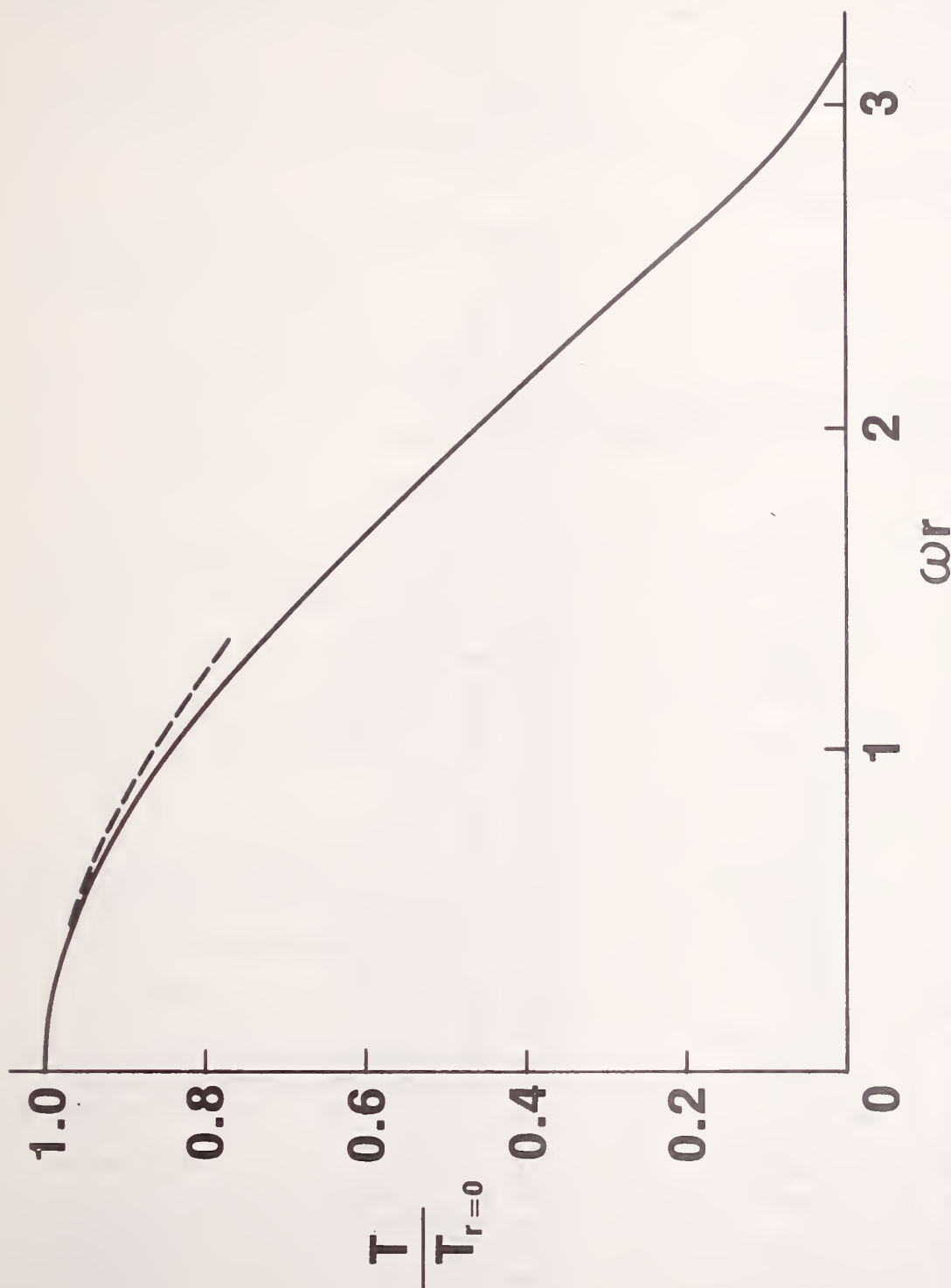


Fig. 6. Radial temperature distribution of a radiating opaque sphere. Surface temperature of sphere will be at some point $R = \omega r$ where ω depends on the heat capacity, thermal conductivity and emittance of sample.

Distribution

National Aeronautics and Space Administration
Washington, D. C. 20546

Mr. F. L. Williams	Code ES	1 copy
Dr. J. R. Carruthers	Code ES	4 copies

National Aeronautics and Space Administration
Johnson Space Center
Houston, Texas 77058

Mr. W. E. Rice	Code EA	2 copies
Mr. J. P. Loftus	Code AT	1 copy
Mr. J. A. Mason	Code DA	1 copy
Mr. E. J. Svreek	Code FM5	1 copy

National Aeronautics and Space Administration
George C. Marshall Space Flight Center
Marshall Space Flight Center, Alabama 35812

Mr. H. P. Gierow	Code PD-MP-DIR	1 copy
Mr. K. R. Taylor	Code PD-MP-T	2 copies
Mr. B. O. Montgomery	Code S&E-DIR	1 copy
Dr. W. G. Johnson	Code S&E-R-DIR	1 copy
Mr. R. E. Lake	Code S&E-R	1 copy
Mr. R. Schwinghamer	Code S&E-ASTN-M	1 copy
Dr. R. S. Snyder	Code S&E-ASTN-MTE	1 copy
Mr. E. C. McKannan	Code S&E-ASTN-MM	1 copy
Mr. R. C. Ruff	Code S&E-ASTN-MEV	1 copy
Miss M. H. Johnston	Code S&E-ASTN-MEV	1 copy
Mr. H. Wuenscher	Code S&E-PE-DIR	1 copy
Mr. I. C. Yates, Jr.	Code S&EPE-A	1 copy
Mr. L. H. Berge	Code S&E-PE-A	1 copy
Mr. G. M. Arnett	Code S&E-SSL-TR	1 copy
Mr. T. C. Bannister	Code S&E-SSL-T	1 copy
Mr. M. C. Davidson	Code S&E-SSL-TR	1 copy
Mr. A. C. Krupnick	Code S&E-ASTN-MT	1 copy
Mr. W. B. McPherson	Code S&E-ASTN-MMM	1 copy
Mr. J. H. Hess	Code S&E-ASTN-MM	1 copy
Mr. L. L. Lacy	Code S&E-SSL-NP	1 copy
Mr. M. F. Nowakowski	Code S&E-QUAL-QT	1 copy
Dr. R. E. Allen	Code S&E-ASTN-MTM	1 copy
Mr. P. H. Rhodes	Code S&E-ASTN-MTE	1 copy
Mr. J. Bond	Code S&E-ASTN-MTE	1 copy
Mrs. B. R. Facemire	Code S&E-SSL-TR	1 copy
Mr. C. F. Schafer	Code S&E-SSL-TR	1 copy
Mr. B. R. Aldrich	Code S&E-PE-MXX	1 copy
Mr. A. Boese	Code S&E-PE-A	1 copy
Mr. R. A. Taylor	Code S&E-PE-MEI	1 copy
Mr. J. R. Williams	Code S&E-PE-M	1 copy
Mr. V. H. Yost	Code S&E-PE-MW	1 copy
Dr. M. P. L. Siebel	Code S&E-PE-DIR	1 copy

Jet Propulsion Laboratory
California Institute of Technology
4800 Oak Grove Drive
Pasadena, California 91103

Dr. C. H. Savage	Code 158-235	1 copy
Dr. M. M. Saffren	Code 183-301	1 copy
Dr. T. G. Wang	Code 183-401	1 copy
Dr. D. D. Elleman	Code 183-401	1 copy
Dr. J. W. Lucas	Code 180-700	1 copy

National Aeronautics and Space Administration
Langley Research Center
Hampton, Virginia 23665

Dr. L. T. Melfi, Jr.	Code 401A	1 copy
Mr. B. W. Cocke, Jr.	Code 401A	1 copy
Dr. R. A. Outlaw	Code 234	1 copy
Dr. J. P. Mugler	Code 215B	1 copy
Mr. J. D. DiBattista	Code 215B	1 copy
Mr. W. C. Ayers	Code 418	1 copy

National Aeronautics and Space Administration
Ames Research Center
Moffett Field, California 91103

Dr. J. A. Parker	Code SC	1 copy
------------------	---------	--------

Grumman Aerospace Corporation
Bethpage, New York 11714

Dr. C. H. Li		1 copy
--------------	--	--------

General Electric Company
Space Sciences Laboratory
P.O. Box 8555
Philadelphia, Pennsylvania 19101

Dr. R. T. Frost		1 copy
-----------------	--	--------

European Space Research Organization
114 Avenue Charles de Gaulle
92 Neuilly, France

Dr. G. Seibert		1 copy
----------------	--	--------

Gesellschaft für Weltraumforschung mbH
505 Porz-Wahn
Linder Höhe
German Federal Republic

Dr. A. Bewersdorff		1 copy
--------------------	--	--------

U.S. DEPT. OF COMM. BIBLIOGRAPHIC DATA SHEET	1. PUBLICATION OR REPORT NO. NBSIR 79-1767	2. Gov't. Accession No.	3. Recipient's Accession No.
4. TITLE AND SUBTITLE NBS: Properties of Electronic Materials		5. Publication Date JUNE 1979	6. Performing Organization Code
7. AUTHOR(S) J. R. Manning		8. Performing Organ. Report No.	
9. PERFORMING ORGANIZATION NAME AND ADDRESS NATIONAL BUREAU OF STANDARDS DEPARTMENT OF COMMERCE WASHINGTON, DC 20234		10. Project/Task/Work Unit No.	11. Contract/Grant No. Government Order H-27954B
12. SPONSORING ORGANIZATION NAME AND COMPLETE ADDRESS (Street, City, State, ZIP) George C. Marshall Space Flight Center National Aeronautics and Space Administration Marshall Space Flight Center, AL 35812		13. Type of Report & Period Covered Annual, Apr. 1978 - Mar. 1979	14. Sponsoring Agency Code
15. SUPPLEMENTARY NOTES <input type="checkbox"/> Document describes a computer program; SF-185, FIPS Software Summary, is attached.			
16. ABSTRACT (A 200-word or less factual summary of most significant information. If document includes a significant bibliography or literature survey, mention it here.) The report describes NBS work for NASA in support of NASA's Materials Processing in Space Program covering the period April 2, 1978 to April 1, 1979. The results obtained are given in detailed summaries in the body of the report. Briefly, in Task I - Surface Tensions and their Variations with Temperature and Impurities - measurements of the surface tension γ of liquid gallium were made in vacuum by the sessile drop technique as a function of temperature T and, in the range 100 °C to 750 °C, it was found that $dy/dT = -0.068 \text{ mJ/m}^2 \text{ } ^\circ\text{C}$. In Task 2 - Solutal Convection and Liquid Diffusion Coefficients - samples of off-eutectic Pb-rich Pb-Sn were directionally solidified, and the macrosegregation and changes in microstructure along the length of the sample, attributed to solutal convection, were measured. In Task 3 - A Thermochemical Study of Corrosion Reactions in Oxide Materials - phase relationships in the $\text{K}_2\text{O-Fe}_2\text{O}_3$ system were investigated up to 1600 °C with major corrosion of the platinum containers being avoided, perhaps because of the small amount of Fe^{+2} in the specimens. In Task 4 - <u>Thermodynamic Properties of Refractory Inorganic Materials as Functions of Temperature</u> - methods of determining heat capacities in reactive liquid samples levitated at high temperatures, especially by use of freely-cooling spherical samples, were analyzed.			
17. KEY WORDS (six to twelve entries; alphabetical order; capitalize only the first letter of the first key word unless a proper name; separated by semicolons) Convection; Heat capacity measurement; Pb-Sn off-eutectic alloys; phase diagram of $\text{K}_2\text{O-Fe}_2\text{O}_3$ system; Solidification; Surface tension of liquid gallium; Thermodynamic properties			
18. AVAILABILITY <input checked="" type="checkbox"/> Unlimited <input type="checkbox"/> For Official Distribution. Do Not Release to NTIS <input type="checkbox"/> Order From Sup. of Doc., U.S. Government Printing Office, Washington, DC 20402, SD Stock No. SN003-003- <input checked="" type="checkbox"/> Order From National Technical Information Service (NTIS), Springfield, VA, 22161		19. SECURITY CLASS (THIS REPORT) UNCLASSIFIED 20. SECURITY CLASS (THIS PAGE) UNCLASSIFIED	21. NO. OF PRINTED PAGES 136 22. Price \$7.25

